ER-13065-571
UR-1104

Total Hadronic Cross Section in Electron-Positron Annihilation at Center-of-Mass Energies from 50 to 57 GeV

by
Toshinori Mori

THE UNIVERSITY OF ROCHESTER

DEPARTMENT OF PHYSICS AND ASTRONOMY

ROCHESTER , NEW YORK

Total Hadronic Cross Section in Electron-Positron Annihilation at Center-of-Mass Energies from 50 to 57 GeV

by
Toshinori Mori

Submitted in Partial Fulfillment
of the
Requirements for the Degree

DOCTOR OF PHILOSOPHY

Supervised by Professor S.L.Olsen

Department of Physics and Astronomy
University of Rochester
Rochester, New York

1988

Research supported in part by U.S. Dept. of Energy
contract DE-AC02-76ER13065.

Abstract

An analysis of electron-positron annihilation into hadronic final states at center-of-mass energies ranging from 50 to 57 GeV, measured by the AMY detector at the TRISTAN e^+e^- collider, is presented. With a data sample corresponding to an integrated luminosity of 19.3 pb^{-1}, a total of 2280 hadronic events were selected. The total cross sections (or the ratios R) were then determined with an overall normalization error of 4.1% and point-to-point systematic errors ranging from 1.1% to 2.8%.

We observed an evident rise in R that is due to the Z^0 intermediate state. Although the measured total cross sections at the higher energies tend to be consistently larger than the prediction of the standard model using the nominal values for M_{Z^0}, $\sin^2\theta_W$, and $\Lambda_{\overline{MS}}$, they are still consistent.

Event shape variables were calculated to further test for the possibility of new heavy quark production. They are all consistent with expectations based on five quark flavors. Assuming a threshold dependence as given by the quark-parton model, 95% confidence level lower mass limits of $m_t > 27.6$ GeV/c^2 for the top quark and $m_{\nu'} > 25.5$ GeV/c^2 for the fourth generation down quark were obtained.

Our R values together with lower energy results were compared to the standard model prediction to obtain best fit values for the standard model parameters M_{Z^0}, the Z^0 boson mass, and $\Lambda_{\overline{MS}}$, the QCD scale parameter. The fits yielded $M_{Z^0} = 88.8 \pm 2.0$ GeV/c^2 and $\Lambda_{\overline{MS}} = 0.17^{+0.15}_{-0.11}$ GeV with the third-order QCD corrections. The value of M_{Z^0}, although somewhat smaller, is still marginally consistent with the direct measurement of M_{Z^0}. In the determination of $\Lambda_{\overline{MS}}$, the effects of the third-order QCD corrections are found to be significant.

VITA

The author was born in Nagoya, Japan in 1960. He studied physics at Tokyo Institute of Technology, and received a B.S. in March, 1982. His B.S. thesis was based on the experimental studies on isospin triplet states of ^{26}Al nucleus that were carried out at the Van de Graaff accelerator of the Institute under the guidance and support of Dr. H. Yokota and Dr. R. Chiba. He was admitted to the graduate school of the same university in 1982. During the first two years of his graduate studies, he was engaged in two nuclear physics experiments, in collaboration with physicists from the University of Tokyo, at the proton synchrotron accelerator at the Japanese National Laboratory for High Energy Physics (KEK). One experiment, lead by Dr. K. Nakai, used a few GeV hadrons (protons or pions) incident on various nuclear targets to study the stopping power of the nuclei. The other one, carried out under Dr. H. Yokota's guidance, used 65 to 160 MeV/c pions incident on ^{6,7}Li targets for studying pion absorption reactions; this became the basis of the author's master thesis. He received an M.S. in March, 1984. His thesis adviser was Dr. R. Chiba. He was awarded a Keidanren scholarship (Ishizaka Foundation) for studying abroad and transfered to the graduate school of University of Rochester in July, 1984. He has been a research assistant at Rochester since then. He received an M.A. from Rochester in May, 1985. He has been engaged in the AMY experiment at the TRISTAN accelerator at KEK from its R&D and construction stages. His thesis adviser has been Dr. S.L. Olsen.

Acknowledgements

I would like to thank S.L. Olsen for continuously encouraging and advising me during my graduate study at University of Rochester. He provided me many precious occasions where I could train myself to be a competent physicist. I am especially indebted to T. Nozaki; the analysis presented in this thesis had been carried out under his guidance. H. Sagawa also made special contribution in offline analysis concerning hadronic events. Many thanks should go to R. Chiba, H. Yokota, and K. Nakai for introducing me to the world of nuclear physics and to high energy physics; I really learned many things (not only physics) when I was working with them. I am quite thankful to K. Ueno, H.W. Zheng, M. Ho, and Y.K. Kim, for making lots of hard work with the CDC more enjoyable and easier. I can never forget the invaluable job that the KEK machine-shop staff and the REPIC ladies had made: all the excellent performance of the CDC belongs to them. It is my pleasure to acknowledge all the collaborators in the AMY experiment; they have been always helpful and I really enjoyed working with those people. I benefited from the interaction with the fellow students and the staff members in Rochester and from the kind treatment by the TRISTAN and KEK staff in Japan. Finally, I am extremely grateful to my parents, who never objected to what I chose to do, and also my special thanks and love are for Yumiko Aoba; without her encouraging words, I would not have had the strength to finish this dissertation.

Contents

Chapter 1

Introduction

TRISTAN [1], the electron-positron collider at the National Laboratory for High Energy Physics (KEK), Japan, became operational in 1987 and opened up a new high-energy frontier for e^+e^- physics, replacing PETRA [2], the storage ring at the DESY laboratory in Hamburg, West Germany, which terminated operations in 1986. The AMY detector [3], situated at one of the four interaction points of the TRISTAN e^+e^- collider, has been in operation since the start of TRISTAN, taking data at the highest e^+e^- center-of-mass energies achieved to date, with the possibility that a new horizon may appear for particle physics.

The primary motivation for the TRISTAN collider and the AMY experiment is to challenge the so-called standard model of elementary particle physics, i.e. the standard (Glashow-Salam-Weinberg) electroweak model (GSW) [4] and quantum chromodynamics (QCD) [5]. To date, the successes of the standard model have been impressive; a wide variety of electromagnetic, weak, and strong interaction processes have been studied with results that have been always in support of the predictions of the model.

In the standard model, all phenomena other than the effects of gravity are described by a set of elementary particles and three kinds of interactions (electromagnetic, weak, and strong interactions) among them. In this model, matter is made up of spin 1/2 particles called quarks and leptons. Quarks differ from leptons in that they carry color charges, which couple them to the strong interaction just as electric charge couples charged particles to electromagnetic forces. Quarks and leptons fit into similar patterns as far as the electroweak interactions are concerned: the quarks come in pairs

$$\binom{u}{d}, \binom{c}{s}, \binom{t}{b}, \ldots \tag{1.1}$$

where the upper quarks have electric charge 2/3, and the lower ones -1/3, while for the leptons we have

$$\binom{\nu_e}{e^-}, \binom{\nu_\mu}{\mu^-}, \binom{\nu_\tau}{\tau^-}, \ldots \tag{1.2}$$

where the upper leptons, called neutrinos, are electrically neutral, and the lower ones have charge -1. Each pair of quarks is associated with a corresponding pair

of leptons, and each set of quark and lepton pairs is called a generation. So far, three generations are necessary to explain the spectrum of observed particles; however, there is no theoretical reason to limit the number of generations to three. In addition to quarks and leptons, there is a set of spin 1 particles that mediate interactions, the so-called gauge particles. The best known example is the photon, γ, which mediates the electromagnetic interaction between charged particles. The recently discovered $W^{\pm}$ and Z^0 bosons mediate weak interaction among quarks and leptons. Similarly, the strong interaction is mediated by massless, neutral particles called gluons. The model requires yet another particle, called the Higgs boson (spin zero), which is instrumental in spontaneously breaking the underlying symmetry of the model and giving masses to the particles. The existence of all of these particles, with the exception of the top quark (t) and Higgs boson (H^0), has been established. At present, there is no evidence for a fourth generation.

In spite of the many successes of the Standard Model, it still has a few missing ingredients. In addition to the still unobserved top quark and Higgs particle, the model has several parameters that are not yet precisely known. Moreover, gravity still cannot be incorporated in the model in a satisfying way and the model cannot answer many fundamental questions like the mysterious equality of the proton charge with the positron charge, etc.

Among the many experiments testing the validity of the Standard Model, those using e^+e^- colliding beams have been particularly useful [2]. This is because e^+e^- reactions are relatively simple to interpret, and the theoretical predictions for these reactions are rather unambiguous. The AMY experiment, which by July, 1988, had logged a sample of data corresponding to a total integrated luminosity of 19.3 pb^{-1} at center-of-mass energies ranging from 50 to 57 GeV, is designed to extend the testing of the standard model into the new high energy region made available by the TRISTAN e^+e^- collider.

This thesis reports on an analysis of e^+e^- annihilation into multi-hadronic final states using all the data accumulated by the AMY detector as of July, 1988. It is organized as follows: i) the first chapter (the current one) is an introduction where physics involving hadronic events is reviewed and the motivation for the analysis methods that we adopted are explained; ii) chapter two contains descriptions of the experimental apparatus and the data sample that was used in the analysis; iii) chapters three, four, and five present the procedures that were used for selecting and analyzing events; and iv) chapter six contains a summary and some conclusions. The author's main responsibility in the implementation of the experiment was the construction of the charged particle detection system and the development of the track reconstruction program. Detailed descriptions of these items are provided in Appendices.

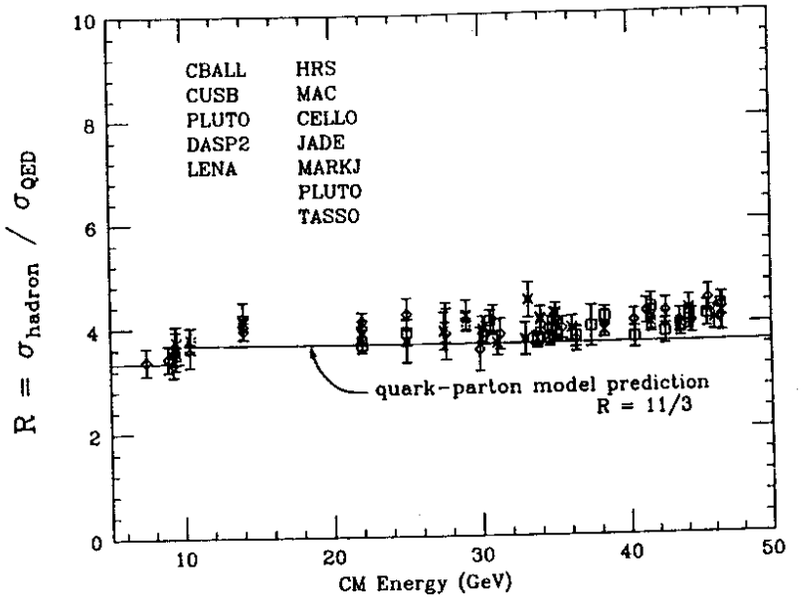

Figure 1.1: $R = \sigma_{hadron}/\sigma_{\mu\mu}$.

1.1 Hadronic Events

The subject of this thesis is the experimental study of the annihilation of high energy electrons and positrons into hadronic final states ($e^+e^- \rightarrow$ *hadrons*). These processes are generally referred to as multi-hadronic annihilation events or, in short, hadronic events.

In the Standard Model, at c.m. energies that are well above the resonance region (associated with the ρ (770 MeV), ω (783 MeV), ϕ (1020 MeV), ψ (3.10 GeV), and Υ (9.46 GeV)), the total cross section for multi-hadronic annihilation has a similar behaviour to that of the QED process $e^+e^- \rightarrow \mu^+\mu^-$, which is $\sigma \propto 1/s$, where s is the center-of-mass energy squared (Fig. 1.1). Typically, as can be seen in the example shown in Fig. 1.2, the final-state hadrons in these events are contained in two highly collimated opposing clusters of particles called "jets". Furthermore, it is observed that the axis of these jets follow an angular distribution of the form,

$$\frac{d\sigma}{d\Omega} \propto (1 + \cos^2\theta), \tag{1.3}$$

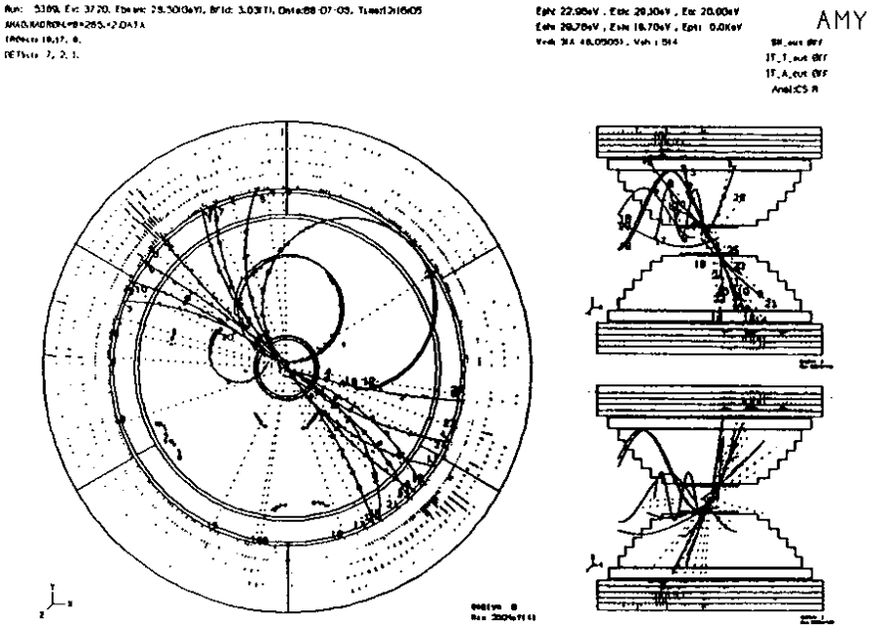

Figure 1.2: A typical hadronic event observed by the AMY detector.

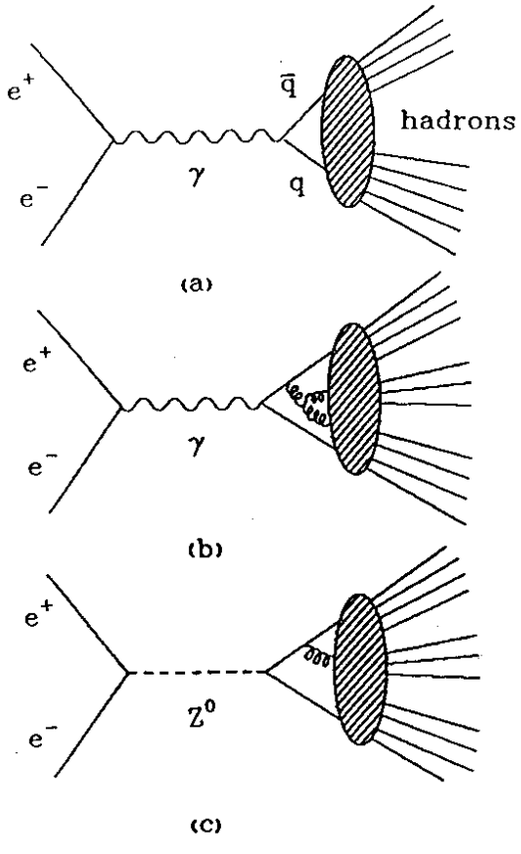

Figure 1.3: Schematic diagrams of $e^+e^- \rightarrow$ *hadrons*. (a) simple quark-parton picture; (b) perturbative QCD corrections; (c) Z^0 propagator.

which is characteristic of the pair creation of spin-1/2 particles in QED. These observations are consistent with a picture of the reaction as proceeding via the production of quark-antiquark pairs followed immediately by the "hadronization" of the quarks into mesons and baryons that move in nearly the same direction as the parent quarks:

$$e^+e^- \to q\bar{q}, \tag{1.4}$$

$$q, \bar{q} \to hadrons. \tag{1.5}$$

This is schematically shown in Fig.1.3(a).

In this picture, the Feynman diagram for hadron production and $e^+e^- \to \mu^+\mu^-$ (mu-pair production) are the same, differing only by the difference in the charges of the quarks. Thus, it is customary to report measurements in terms of the ratio R, which is the total hadronic cross section in units of the lowest order QED mu-pair cross section at the same energy. In the quark model, R is simply related to the quark charges Q_q (in units of proton charge) as

$$R \equiv \frac{\sigma(e^+e^- \to hadrons)}{\sigma(e^+e^- \to \mu^+\mu^-)} \simeq \frac{\sigma(e^+e^- \to q\bar{q})}{\sigma(e^+e^- \to \mu^+\mu^-)} = 3\sum_q Q_q^2, \tag{1.6}$$

where the summation is carried out over all the quark flavors that can be created and the factor 3 reflects the three color degrees of freedom of each quark. With the five known quark flavors, the quantity R becomes $3\cdot(\frac{1}{3}^2+\frac{2}{3}^2+\frac{1}{3}^2+\frac{2}{3}^2+\frac{1}{3}^2) = \frac{11}{3}$. While this simple calculation agrees fairly well with experimental measurements, the agreement is not exact (see Fig.1.1 and 1.4).

The small observed difference between the measured values of R and the simple prediction are explained as higher order QCD corrections, corresponding to the radiation of gluons. The Feynman diagrams for these higher order processes are shown in Fig. 1.3(b); experimentally they appear as hadronic events that contain three or more jets. An example of an event with three distinct jets is shown in Fig. 1.5.

An expression for R that includes QCD corrections up to second order has been given in the so-called $\overline{\rm MS}$ renormalization scheme ("modified minimal subtraction" scheme) by Ref. [6] as follows:

$$R \simeq 3\sum_q Q_q^2 \cdot \left(1 + C_1\frac{\alpha_S}{\pi} + C_2\left(\frac{\alpha_S}{\pi}\right)^2\right). \tag{1.7}$$

Here, $C_1 = 1$ and $C_2 = 1.986 - 0.115n_f$ for massless quarks, where n_f is the number of different quark flavors; and α_S, the "running" strong coupling strength, is, in second-order QCD,

$$\alpha_S(s) = \frac{12\pi}{(33-2n_f)\ln(s/\Lambda^2_{\overline{MS}}) + 6\frac{153-19n_f}{33-2n_f}\ln(\ln(s/\Lambda^2_{\overline{MS}}))}. \tag{1.8}$$

Recently, third order QCD corrections have been analytically calculated and found to be larger than the second order corrections [8]; $C_3 = 70.985 - 1.200n_f -$

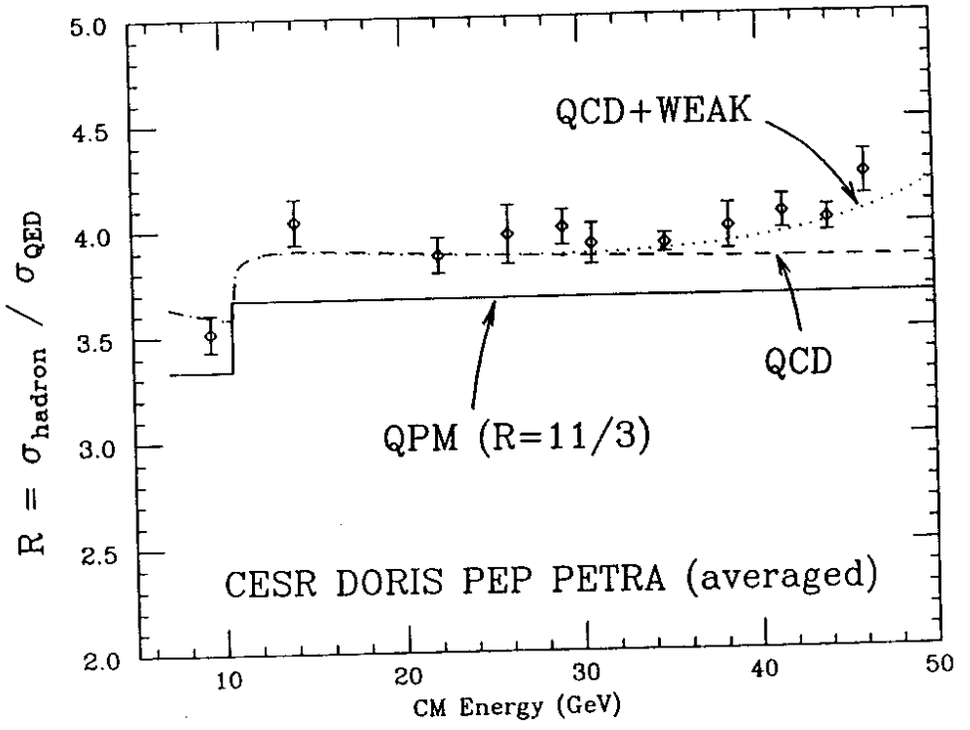

Figure 1.4: Same as Fig. 1.1, but data in similar energy regions are averaged.

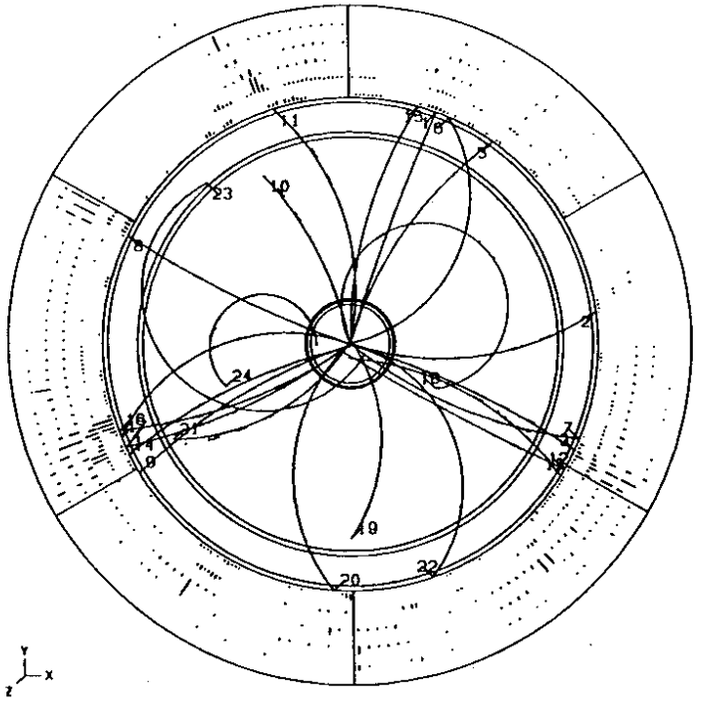

Figure 1.5: A three-jet event observed by the AMY detector.

$0.005n_f^2 - 0.840(\sum Q_q)^2/3\sum Q_q^2 \simeq 64.835$ for $n_f = 5$, that is, $C_3/C_2(\alpha_S/\pi) \simeq 2.3$. This result suggests a possibility that the lower order corrections are accidentally small, and might even pose a question on the validity of the perturbative calculations of QCD. However, this result is very recent and has not been checked by other groups. In the analysis here, results for both second order and third order corrections are presented for comparison.

Also, as the energy increases, annihilations via Z^o intermediate states (Fig. 1.3 (c)) become more important and are seen as a rise in R at the highest energy PETRA data (Fig. 1.4). Including all of these effects results in the following theoretical formula for R (see Ref. [9]):

$$R = 3\sum_q \left[\frac{1}{2}\beta(3-\beta^2)\left(1 + C_1^V\frac{\alpha_S}{\pi} + C_2^V\left(\frac{\alpha_S}{\pi}\right)^2\right)C_{VV} + \beta^3\left(1 + C_1^A\frac{\alpha_S}{\pi} + C_2^A\left(\frac{\alpha_S}{\pi}\right)^2\right)C_{AA}\right], \quad (1.9)$$

where the quark velocity β reflects the effects of the quark masses; the explicit β-dependence of C_1^V, C_1^A is approximated by [7]

$$C_1^V = \frac{4}{3}\pi\left[\frac{\pi}{2\beta} - \frac{3+\beta}{4}\left(\frac{\pi}{2} - \frac{3}{4\pi}\right)\right]$$
$$C_1^A = \frac{4}{3}\pi\left[\frac{\pi}{2\beta} - \left(\frac{19}{10} - \frac{22}{5}\beta + \frac{7}{2}\beta^2\right)\left(\frac{\pi}{2} - \frac{3}{4\pi}\right)\right]. \quad (1.10)$$

The effects of Z^0 intermediate states are included in C_{VV} and C_{AA};

$$C_{VV} = Q_q^2 - 8Q_q g_V^e g_V^q \mathrm{Re}(\chi(s)) + 16(g_V^{e\,2} + g_A^{e\,2})g_V^{q\,2}|\chi(s)|^2, \quad (1.11)$$

$$C_{AA} = 16(g_V^{e\,2} + g_A^{e\,2})g_A^{q\,2}|\chi(s)|^2, \quad (1.12)$$

$$\chi(s) = \frac{1}{16\sin^2\theta_W\cos^2\theta_W}\cdot\frac{s}{s - M_{Z^o}^2 + iM_{Z^o}\Gamma_{Z^o}}. \quad (1.13)$$

Here g_V and g_A are the vector and axial vector couplings of the fermions that are given by the standard model in terms of the parameter θ_W (electroweak mixing angle):

$$g_V^f = T_{3,f} - 2Q_f\sin^2\theta_W, \quad g_A^f = T_{3,f}, \quad \text{for } f = e, q \quad (1.14)$$

where $T_{3,f}$ $(= \pm\frac{1}{2})$ is the third component of the fermion's weak isospin. And M_{Z^o} and Γ_{Z^o} are the mass and the width of the Z^0.

This formula for R contains several parameters that cannot be calculated by the standard model. These parameters can be determined from measurements of R and comparisons of the values obtained in this way with those measured from studies of other processes pose stringent tests on the standard model.

From a theoretical point of view, the QCD scale parameter $\Lambda_{\overline{MS}}$ can be best determined by R measurements. Other methods for determining $\Lambda_{\overline{MS}}$ necessarily

involves theoretical ambiguities due to low energy behaviour of QCD (hadronization) or rather large renormalization scheme dependence in the perturbative calculations [10]. In contrast, hadronization processes have no effect on R (total cross section) measurements and since the TRISTAN energy region is far above flavor production thresholds, the application of perturbation theory for calculating the QCD corrections in the above formula is expected to be reliable (unless, of course, a new quark is found in the TRISTAN energy range). The primary problem for determining $\Lambda_{\overline{MS}}$ by this method lies in the fact that the QCD contribution to R is only about 5%; the precision to which $\Lambda_{\overline{MS}}$ is determined is thus limited by the systematic errors of R measurements. Systematic normalization errors usually attained for R measurements range from 2% to 7% and translate into at least 25% errors of α_S, which translates into errors of more than 80% in $\Lambda_{\overline{MS}}$.

For the electroweak theory, in addition to the fermion and Higgs masses, there are three independent parameters that must be determined experimentally. Once they are determined, the theory can provide unambiguous predictions. The independent parameters can be chosen among many parameters of the theory; for two of them, we choose the electric charge of the electron, e, (or equivalently $\alpha = e^2/4\pi$) and the Fermi constant G_F since these are very precisely determined from the low energy experiments. For the remaining free parameter we could use equivalently the vector boson masses M_{Z^0}, $M_{W^\pm}$, or the electroweak mixing angle $\sin^2\theta_W$. We use M_{Z^0} for the following reasons. The vector boson masses and $\sin^2\theta_W$ are related through the following equations:

$$\sin^2\theta_W = 1 - M_W^2/M_{Z^0}^2, \tag{1.15}$$

$$M_W^2 = \frac{\pi\alpha}{\sqrt{2}G_F \sin^2\theta_W} \tag{1.16}$$

R measurements can determine one of those parameters, say M_{Z^0}; from this, we can obtain the other ones from these equations.

The value of $\sin^2\theta_W$ is currently most precisely obtained from neutrino scattering experiments, while the vector boson masses, M_W and M_{Z^0}, have been directly measured by production experiments using $p\bar{p}$ collisions [11,12]. Comparisons of the results of these experiments with the relations listed above give a small inconsistency (i.e., a $\sim$7% difference between the left hand side and the right hand side of the Eq. 1.16). This apparent inconsistency can be resolved by introducing radiative corrections for the electroweak theory [13], which modify the above relations by a sizable amount. The actual forms of modified relations and, therefore, the definition of $\sin^2\theta_W$, depend on the renormalization scheme chosen for the calculation. On the other hand, M_{Z^0} and M_W, being physically measurable variables, are safely independent of the schemes. In light of this, care must be taken when the values of $\sin^2\theta_W$ are compared for different analyses. We adopt M_{Z^0} as the free parameter to avoid possible confusion.

For our analysis, we use the on-shell renormalization scheme [14], which has an evident physical interpretation and is also convenient. The independent parameters in this scheme are the masses of particles and α. $\sin^2\theta_W$ is no longer

an independent quantity and is just defined by Eq. 1.15. Taking into account the radiative corrections applied to muon decay measurements when they are converted to values for G_F, we get a modified version of Eq. 1.16,

$$M_W^2 = \frac{\pi\alpha}{\sqrt{2}G_F \sin^2\theta_W(1-\Delta r)} \tag{1.17}$$

Here Δr represents weak corrections to the muon decay diagram that are not taken into account in the determination of G_F. (When G_F is extracted from experiments, it is only corrected for QED radiative effects within the framework of the Fermi model.) The dominant contribution to Δr comes from self energy correction to the W propagator. In terms of Δr and G_F, the relation between the electroweak mixing angle and M_{Z^0} becomes

$$\sin^2\theta_W = \frac{1}{2}\left(1 - \sqrt{1 - \frac{4\pi\alpha}{\sqrt{2}G_F M_{Z^0}^2(1-\Delta r)}}\right) \tag{1.18}$$

There are two unknown parameters that enter into the calculation of the radiative correction Δr, the t quark mass, m_t, and the H^0 mass, m_{H^0}; for these we have no experimental input. As shown in Fig. 1.6, in contrast to weak dependence of Δr on m_{H^0}, Δr changes by a considerable amount for various values of m_t; for large m_t its sign even changes.

With no theoretical way to fix this ambiguity, the amount of electroweak corrections necessary to explain the existing inconsistency between various measurements has been estimated, and it is found that $\Delta r = 0.077 \pm 0.037$ fits all the available experimental data reasonably well [15]. (See also Ref. [16]. This result of positive Δr leads to setting an upper limit on the top quark mass of $m_t < 180$ GeV/c^2 with 90% confidence level.) In our analysis we use $\Delta r = 0.070$, which is consistent with the above analysis and corresponds to $m_t = 45$ GeV/c^2, $m_H = 100$ GeV/c^2, and $M_{Z^0} = 92$ GeV/c^2 [17]. It should be noted from Fig. 1.6 that Δr depends only weakly on the value of M_{Z^0}; so it is justified to regard Δr as a constant for a reasonable range of the value of M_{Z^0}.

The width of the Z^0, Γ_{Z^0}, is calculated by using the available data to be 2–3 GeV [18] according to the formula in Ref. [19]. Because R in the TRISTAN (and lower) energy region is not sensitive to the precise value of Γ_{Z^0}, we use $\Gamma_{Z^0} = 2.5$ GeV and treat it as a constant.

In summary, the procedure we use to compare the experimental results with the theoretical predictions is as follows: (1) write the R formula (Eq. 1.9) in terms of $\Lambda_{\overline{MS}}$ and M_{Z^0} using Eq. 1.18, i.e., $R_{theo} = f(\Lambda_{\overline{MS}}, M_{Z^0})$, (2) correct the experimental data for radiative effects to obtain the experimental value, R_{exp}, and (3) compare R_{exp} with R_{theo} to obtain $\Lambda_{\overline{MS}}$ and M_{Z^0}. Then $\sin^2\theta_W$ can be calculated from M_{Z^0} through Eq. 1.18. Since at TRISTAN energies we expect to see a significant rise in R due to the effects of the Z^0 intermediate state in the annihilation process (Fig. 1.4), our experiment is much more sensitive to the electroweak parameters than the PEP and PETRA experiments. The energy

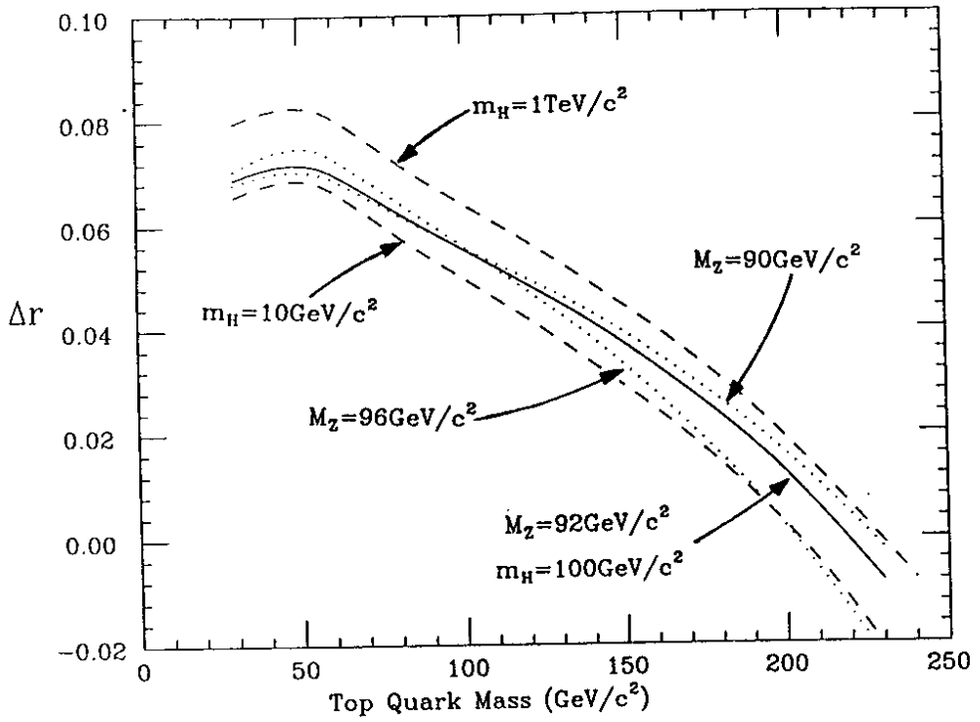

Figure 1.6: Dependence of Δr on m_t, m_{H^0}, and M_{Z^0}. Dashed lines indicate m_{H^0}-dependence for M_{Z^0} = 92 GeV/c², while dotted lines indicate M_{Z^0}-dependence for m_{H^0} = 100 GeV/c².

dependence of the QCD terms come in through α_S, which varies as $\ln s$ and, thus, are expected to be almost constant all over a broad energy range.

Each experiment at PEP and PETRA made an effort to extract α_S and $\sin^2\theta_W$ from their data. However, because of the different analysis methods used in the different experiments, it is difficult to combine their results for these parameters. Instead we proceed by combining all the different measured values of R and applying a global fit using the formalisim just described.

Such a global fit was, in fact, recently carried out by CELLO [20]. They combined the results from CELLO, MARK J, PLUTO, TASSO, JADE, MAC, and HRS [21,22,23] to obtain the result,

$$\sin^2\theta_W = 0.236 \pm 0.020, \qquad \alpha_S\left((34\mathrm{GeV})^2\right) = 0.165 \pm 0.030, \tag{1.19}$$

where the quoted errors correspond to $\chi^2 = \chi^2_{min} + 1$ (39 % confidence level). It was necessary to adjust some of the published R values (by as much as 2 %) because of differences in the radiative corrections that were used. When they included data from energies below the $b\bar{b}$ threshold from CESR and DORIS [24], they got

$$\alpha_S\left((34\mathrm{GeV})^2\right) = 0.166 \pm 0.023 \qquad \text{with } \sin^2\theta_W \text{ fixed at } 0.23, \tag{1.20}$$

demonstrating the validity of the R formula over the quark flavour thresholds.

The CELLO group used a different parametrization for the function χ (cf. Eq. 1.13),

$$\chi(s) = \frac{G_F}{8\sqrt{2}\pi\alpha} \cdot \frac{s M^2_{Z^0}}{s - M^2_{Z^0} + iM_{Z^0}\Gamma_{Z^0}} \tag{1.21}$$

and explicitly avoided using the weak correction factor Δr by regarding M_{Z^0} in χ as a constant (92.3GeV/c²), arguing that, for their energies, the values of R are not strongly dependent on the exact value of M_{Z^0} in χ. With experimental precisions on R of 5-10%, this approximation is applicable in the PEP/PETRA energy region; deviations from the correct formula is less than 1 % even for the highest PETRA energies. However, this no longer applies at TRISTAN energies, where the effects of the Z^0 are larger.

In the analysis reported here we use the method described above, which is theoretically unambiguous, to extract the parameters of the standard model by combining the available R measurements with our results.

1.2 New Heavy Quarks

As mentioned above, the only missing ingredients of the Standard Model are the top quark and the Higgs boson. The t quark will be pair-created in e^+e^- collisions via the process 1.4, provided that the t mass is less than the beam energy. Since the Higgs-fermion coupling is expected to be proportional to the fermion's mass, the coupling between t and H^0 will be large. Thus, when the

t quark is found, definitive searches for H^0 particles produced in decays of $t\bar{t}$ resonance states (toponium states) can be made [26].

If $t\bar{t}$ is produced through the process 1.4, then it can be readily recognized as the increase in R by an amount that is nominally $\Delta R \simeq 3 \times Q_t^2 = 4/3$ (actually, the weak effects and the QCD corrections cause the expected rise to be 1.5) as indicated by the formula 1.9. Thus, a precise measurement of R will indicate or exclude the existence of the $t\bar{t}$ production. In addition, when the production threshold is crossed, the (heavy) t quarks will be produced almost at rest. Since each quark is expected to predominantly decay into three lighter quarks, the spatial distribution of the final-state particles in the $t\bar{t}$ production will tend to be isotropic, in contrast to the collimated jet structure observed for light quark production. This difference in the "event shape" was used to identify the threshold for $b\bar{b}$ production and has been used as a signature for previous $t\bar{t}$ searches [27]. This method for searching for new heavy quarks has a higher sensitivity than that of R measurements and will be discussed later in this section. It is important to note that this event shape difference, originating from the quark kinematics, does not depend much on the (theoretically ambiguous) details of hadronization process.

The standard model makes no direct prediction for the mass of the t-quark. However a number of experimental searches have been made and a number of conclusions about the t quark mass can be made from other experimental facts. We summarize the current knowledge of the t quark mass as follows:

- $m_t > 23.3$ GeV/c^2 from the R measurements and the event shape analysis for e^+e^- collisions at PETRA [27,28,29].
- $m_t < 180$ GeV/c^2 with 90% C.L. from the study of the radiative corrections to the electroweak processes with updated experimental data (as discussed in the previous section) [15,16].
- $m_t > 44$ GeV/c^2 with 95% C.L. from the study of the events with an isolated, high transverse momentum lepton, together with two or more jets, in $p\bar{p}$ collisions, observed by the UA1 group at CERN [30].
- $m_t < m_W$ from the ratio of $W(\rightarrow e\nu)$ and $Z(\rightarrow e^+e^-)$ events produced in $p\bar{p}$ collisions at CERN [31].
- $m_t > 50$ GeV/c^2 from the efforts to incorporate the recently observed $B\overline{B}$ mixing [32] in the standard model [33].

From all of the above information combined, we may conclude 50 GeV/c^2 < $m_t < m_W$, giving TRISTAN, which has a maximum center-of-mass energy of 66 GeV, no hope of pair-producing t quarks. There are, however, a number of caveats to the above mass limits, including:

- The mass limit obtained from the $B\overline{B}$ mixing should be relaxed as low as 35 GeV/c^2 at the 1σ level if the theoretical ambiguities are correctly taken into account [34].

- The lower mass limit given by UA1 relies on theoretical calculations for production processes, which may not be very reliable. In addition, the experimental limits are less restrictive in the lower mass range ($m_t \sim$ 25 GeV/c^2) [35].

Moreover, all the above arguments regarding t mass limits are made in the context of the Standard Model, which is not generally regarded as a complete theory. With new assumptions beyond the Standard Model, for example the existence of a massive charged scalar [36] or inclusion of more generations [37], these mass limits are relaxed considerably. New physics assumptions often predict new sets of particles which might be found in the TRISTAN energies in addition to the top quarks. On the other hand, attempts to modify the standard model to exclude t-quarks [38] have failed experimental tests [39].

In addition to the t-quark, another generation of quarks and leptons (the fourth generation) can exist within the framework of the Standard Model. In Fig. 1.7 we show the pattern of the known fermion masses. In the absence of a definite theoretical prediction for the masses of fourth new generation quarks, this figure may give an indication of what they might be. From the figure it is clear that a fourth generation charge $-1/3e$ quark, the so-called b' quark, might well lie in the TRISTAN energy region. The signatures for the b' quark production are expected to be similar to those of the t quark production, namely, an increase in R and an isotropic distribution of final-state particles [40]. (It was pointed out by Ref. [41] that the b' quark decay may be dominated by flavor changing neutral currents. In the analysis here, we do not consider such possibility.) However, because it has a smaller electric charge, the b' quark will have a production rate that is lower, we expect $\Delta R \simeq 3 \times Q_{b'}^2 = 1/3$ (~ 0.5 with the weak effects and the QCD corrections).

The observation of an anomalous excess of low thrust hadronic events with isolated muons, reported by two PETRA experiments (MarkJ and JADE) for their highest center-of-mass energies (46.30–46.78 GeV) [42,43], has been interpreted as a possible indication of the production of the b' quarks [44]. However, the other experiments at PETRA did not observe such an excess [45]. In addition, although we expect a similar excess for events with electrons for b' production, it was not observed. These observations make the interpretation of these events as the b' production rather difficult. However, if these effects are an indication of the opening of a threshold for some new phenomenon, the AMY experiment, operating at higher energies, should be able to identify it clearly through the study on the hadronic events.

Event Shape Analysis Method

Several variables have been used to quantify the event shape; for the analysis reported here we use the quantities thrust and acoplanarity. It has been argued that since these variables are linear in the particle momenta, they are less sensitive to the uncertainty about quark masses and, thus, theoretically prefer-

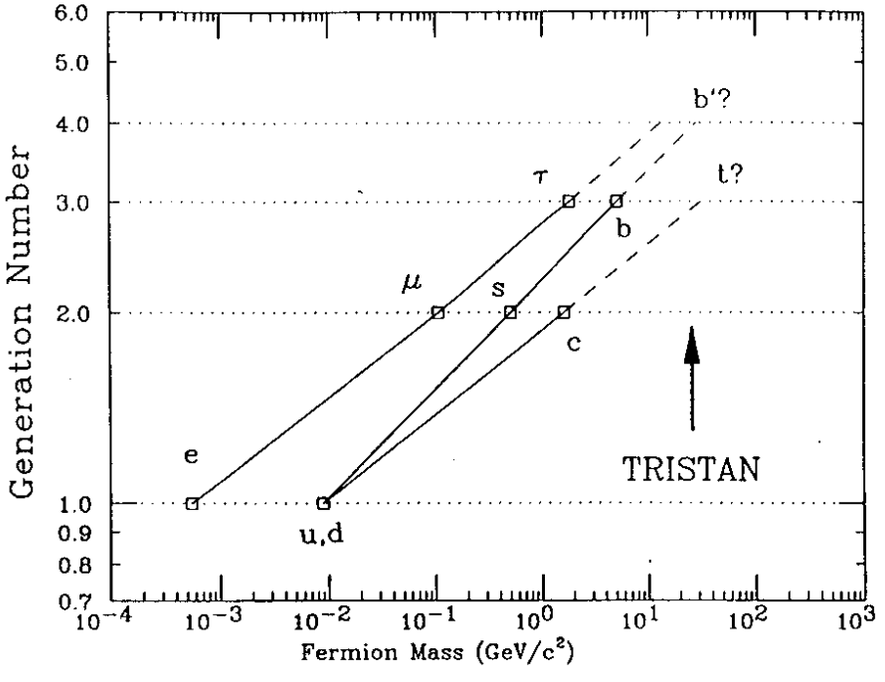

Figure 1.7: Generation number vs fermion masses.

able. The parameter thrust was first discussed by Farhi (ref. [46]); the related parameter acoplanarity was first used by DeRujula (ref. [47]).

The thrust (T) is defined as follows:

$$T = \max_{|\mathbf{t}|=1} \frac{\sum_j |\mathbf{p}_j \cdot \mathbf{t}|}{\sum_j |\mathbf{p}_j|}, \tag{1.22}$$

and the thrust axis is the vector $\mathbf{t}$ for which maximum is attained. The allowed range is $0.5 < T < 1.0$ where $T = 1$ corresponds to perfect back-to-back jets and $T = 0.5$ to perfectly isotropic events. Thus, $t\bar{t}$ production will be recognized as an excess of low thrust events, while light quark production tends to give high thrust values. This is exhibited in Fig. 1.8, where thrust distributions for hadronic events with and without $t\bar{t}$ production, simulated by a Monte Carlo program, are compared. (We describe the system for event simulation in chapter 2.)

However, as mentioned above, the radiation of gluons by quarks creates events with three or more jets, which can result in events with low thrust values that may be confused with $t\bar{t}$ production. Momentum conservation assures that three jet events, which are expected to occupy a considerable fraction $\sim O(\alpha_S)$ of the hadronic events, have a planar or pancake-like shape. Thus, by discriminating planar events from spherical ones, we can further improve the signal/background ratio for $t\bar{t}$ production. We utilize the event shape variable called acoplanarity A to distinguish planar from spherical event shapes. It is defined as follows.

In the plane perpendicular to the thrust axis $\mathbf{t}$, major and minor moments and their axes, $\mathbf{n}$ and $\mathbf{m}$ ($|\mathbf{n}| = 1, |\mathbf{m}| = 1$), are defined as:

$$Major = \max_{\mathbf{n}\cdot\mathbf{t}=0} \frac{\sum_j |\mathbf{p}_j \cdot \mathbf{n}|}{\sum_j |\mathbf{p}_j|} \tag{1.23}$$

$$Minor = \frac{\sum_j |\mathbf{p}_j \cdot \mathbf{m}|}{\sum_j |\mathbf{p}_j|} \tag{1.24}$$

where $\mathbf{m} \cdot \mathbf{t} = 0$ and $\mathbf{m} \cdot \mathbf{n} = 0$.

The acoplanarity A is given by

$$A = 4 \min_{|\mathbf{l}|=1} \left(\frac{\sum_j |\mathbf{p}_j \cdot \mathbf{l}|}{\sum_j |\mathbf{p}_j|} \right)^2 = 4(Minor)^2, \tag{1.25}$$

where $0 < A < 1$. Because planar events and two jet events correspond to low acoplanarity, spherical $t\bar{t}$ events can be distinguished by their high value of acoplanarity (Fig. 1.9).

Here, because of the limited acceptance of the detector, the allowed ranges of the values of T and A are actually limited. For a detector with acceptance $|\cos\theta| < \cos\Theta$, the ranges,

$$\frac{(\pi - 2\Theta) + \sin 2\Theta}{2\pi \cos\Theta} < T < 1.0 \tag{1.26}$$

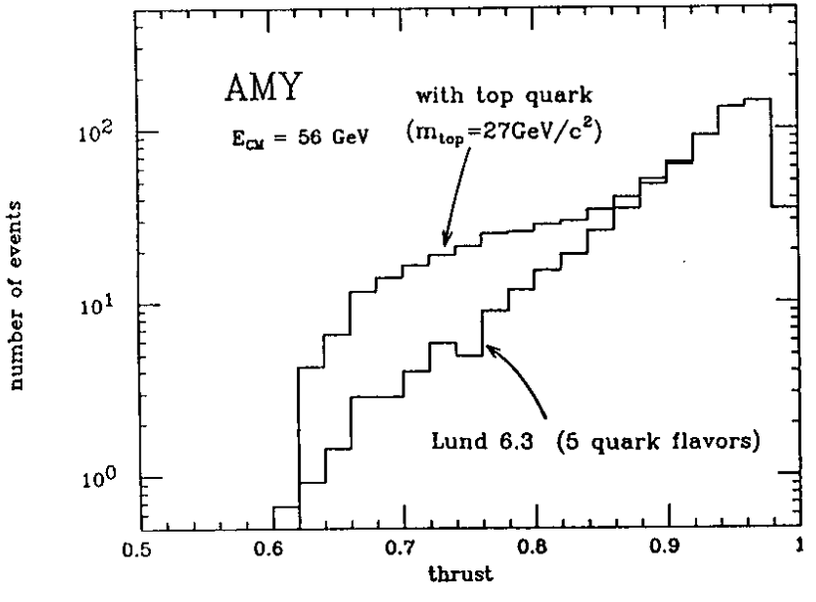

Figure 1.8: Thrust distributions for hadronic events with and without $t\bar{t}$ production. (MC simulation by Lund 6.3.)

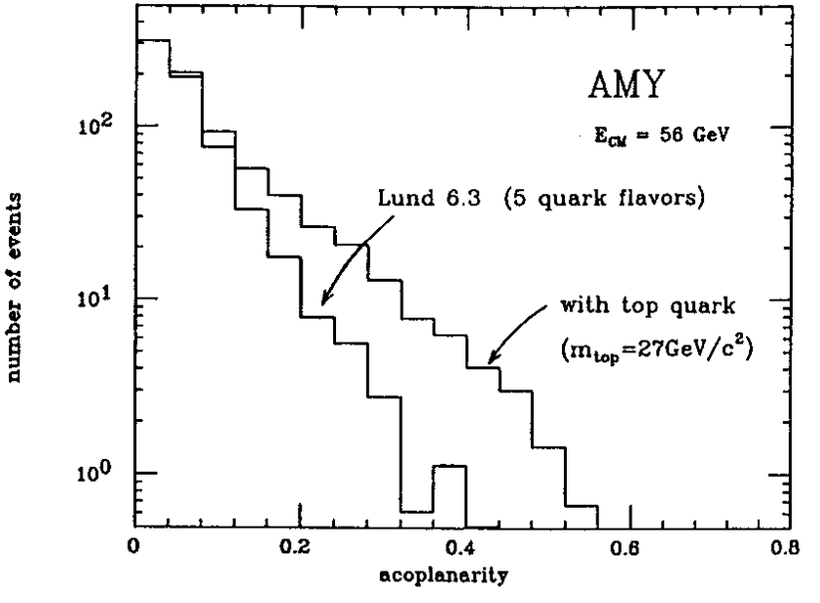

Figure 1.9: Acoplanarity distribution for hadronic events with and without $t\bar{t}$ production. (MC simulation by Lund 6.3.)

and

$$0.0 < A < \cos^2\Theta \tag{1.27}$$

are allowed. For the AMY experiment which has $\cos\Theta \sim 0.8$, These correspond to

$$0.56 < T < 1.0 \quad \text{and} \quad 0.0 < A < 0.64. \tag{1.28}$$

Thus, by counting number of events with, for example, $A > 0.36$, our Monte Carlo simulations indicate that we can expect to see more than ten times as many events with $t\bar{t}$ production as without $t\bar{t}$ production. This method has a much higher sensitivity to $t\bar{t}$ production than that of R measurements, where only about a 30% excess is expected.

Chapter 2

The AMY Experiment

The accelerator, detector, and the software tools used for the analysis presented here are described in this chapter.

2.1 The TRISTAN e^+e^- Collider

TRISTAN [1] (Transposable Ring Intersecting STorage Accelerator in Nippon, or informally known as the TRIal of the STANdard Model) is the name of the new e^+e^- colliding beam complex at KEK (Kou Enerugii Butsuri-gaku Kenkyuu-jyo, or National Laboratory for High Energy Physics) in Tsukuba City, Japan (See Fig. 2.1.).

TRISTAN consists of four serially connected accelerator systems: the positron generator system, the electron linear accelerator (LINAC), the accumulation ring (AR), and the main ring (MR).

Positrons, generated by bombarding 200 MeV electrons onto a Tantalum target, are transferred into the LINAC. The LINAC is 400m long and accelerates electrons and positrons to 2.5 GeV, from which they are fed into the AR. After the accumulation of a sufficient number of particles, (beam currents of ~10mA) in its 377m circumference, the AR accelerates the electron or positron beams up to 8.0 GeV and injects them into the MR.

The 3km circumference MR consists of four straight sections (each 200m long) and four arc sections (each 550m long). Electrons (positrons), grouped in two bunches each of length of a few cm, are circulated clockwise (counter-clockwise) in the MR. The electron and positron bunches are arranged to meet at the center of each straight section, the collision points, where their transverse dimensions are compressed by focusing magnets. Surrounding the collision points are detector systems for studying the products of the collisions. With a total RF power of 25 MW, the MR can accelerate and store beams up to energies of $\sim$ 30 GeV, providing e^+e^- collisions with a center-of-mass energy of 60 GeV. The energy spread of the beam in the MR is relatively large, $\sigma_E/E = 1.64 \times 10^{-3}$ (r.m.s.), i.e., ~50MeV for 30GeV beams; this is due to the relatively small bending radius of the MR arcs.

The first electron-positron collisions occurred in November, 1986, at the

center-of-mass energy of 50 GeV. The physics research program started with an initial test run in January and February, 1987, and has subsequently continued with the beam energies increasing to 57 GeV by the summer of 1988.

The target luminosity of TRISTAN, $\sim 1 \times 10^{31} \mathrm{cm}^{-2}\mathrm{sec}^{-1}$, has been achieved, and currently operation with this luminosity is being pursued. The daily integrated luminosity has been increasing continuously to the point where it has exceeded $300\mathrm{nb}^{-1}$/collision point/day (Fig. 2.16).

2.2 The AMY Detector

The AMY detector (Fig.2.2) [3], located at the OHO experimental hall of TRISTAN, is a general-purpose detector with special emphasis on lepton identification. A superconducting solenoidal coil provides a 3 tesla magnetic field that is coaxial with the beam and extends to a radius of 1.2 meters. This high magnetic field provides for good charged particle momentum resolution (as good as or better than that of larger, more conventional detectors) in a rather compact system. In the following, a brief description of the AMY detector is given, with an emphasis on the "barrel" part of the detector, i.e., the Central Drift Chamber (CDC) and the Shower Counter (SHC), data from which comprise the basis of the analysis presented in this thesis. A more detailed description of the CDC and its associated software, the area of the detector in which the author was primarily engaged, is provided in Appendices.

2.2.1 The Central Drift Chamber and the Inner Tracking Chamber

Charged particle trajectories are measured in two devices, the Inner Tracking Chamber (ITC) and the Central Drift Chamber (CDC). In emerging from the vacuum system of the storage ring, charged particles pass through an amount of material corresponding to a thickness of only 1.7% radiation length before they are measured in these devices.

The ITC (Fig. 2.3) consists of four layers of drift tubes (aluminized plastic tubes with 16μm diameter anode wires stretched along their axes) each approximately 6mm in diameter, which provide position measurements of trajectory coordinates in the plane perpendicular to the beam direction (the $r - \phi$ plane) with a spatial resolution of $\sigma \sim 80\mu$m. The gas in the ITC (50% Ar, 50% C_2H_6) is pressurized to $1.48\mathrm{kg/cm}^2$ to help improve good spatial resolution. The ITC extends from a radius of 12.2cm to 14.2cm and its fiducial length along the beam direction (the z axis) is 55cm. Its robust drift tube structure was particularly useful during the initial test run periods, where, under severe background conditions, it provided a fast rejection of background events at the trigger level.

The CDC (Fig. 2.4), located just outside the ITC, has 40 cylinders of wires extending out to a radius of 65 cm. Twenty five of the cylinders (containing 5616 individual drift cells, each approximately 6 mm in diameter) have wires

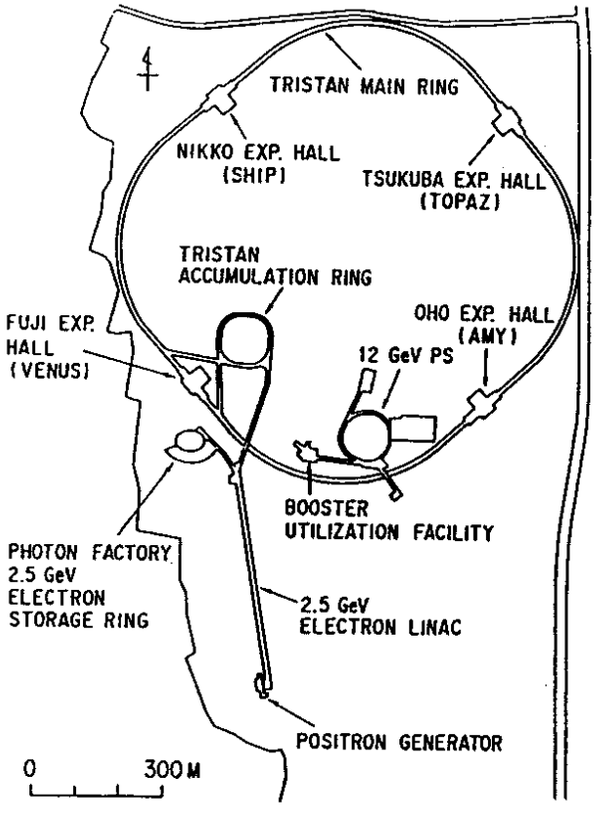

Figure 2.1: An overview of the TRISTAN accelerator complex. The AMY detector is located at the OHO experimental hall.

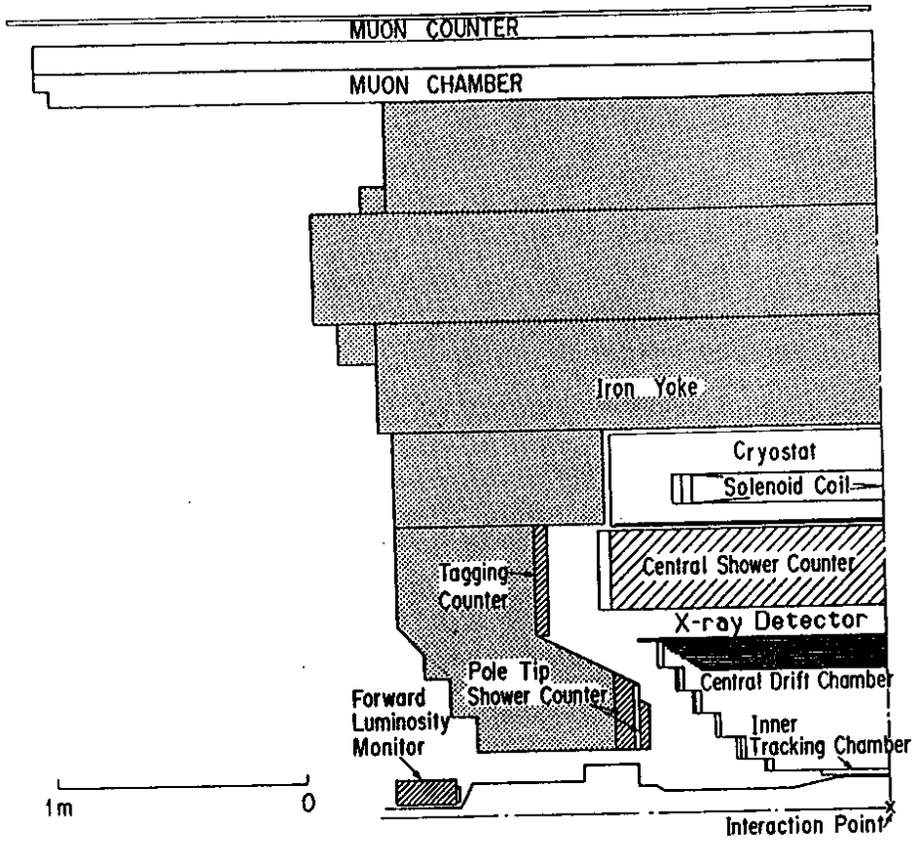

Figure 2.2: The AMY detector. For the 50 and 52 GeV runs, trigger scintillation counters were located where the X-ray detector is currently situated.

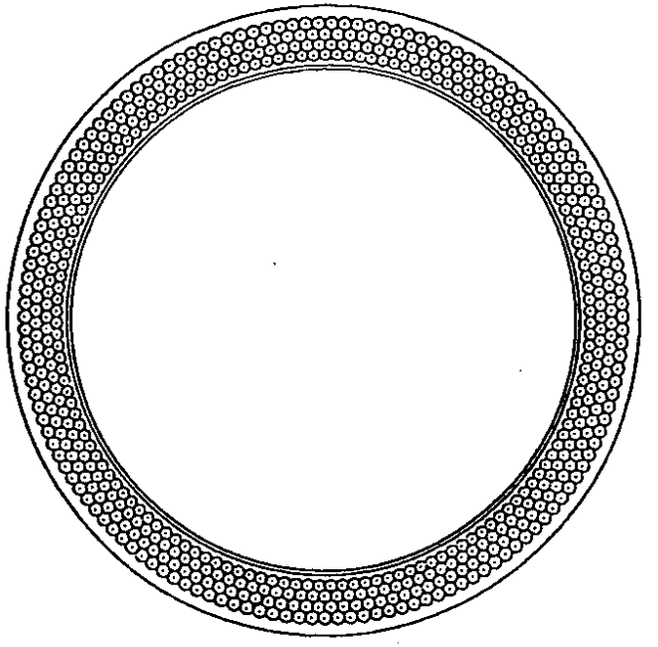

Figure 2.3: A cross-sectional view of the Inner Tracking Chamber

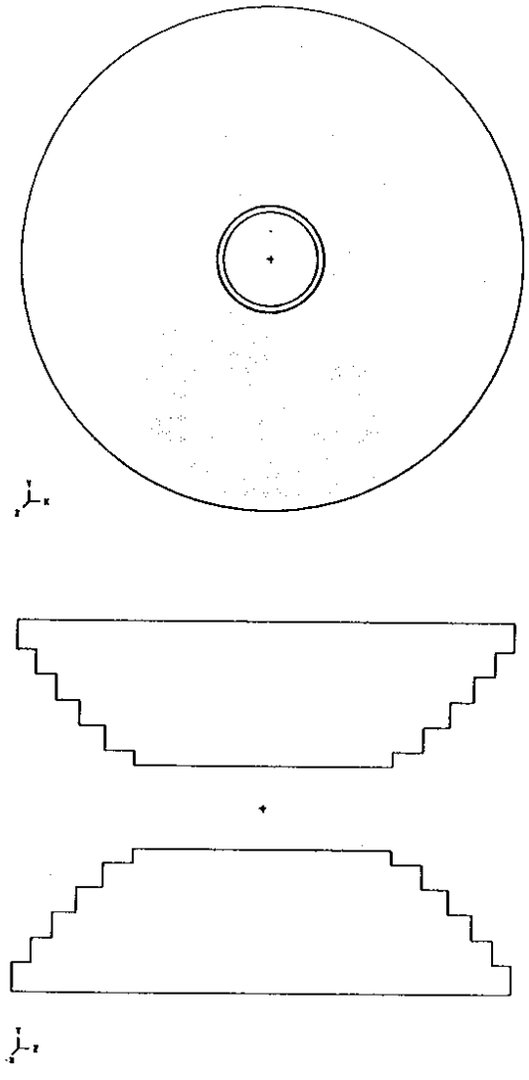

Figure 2.4: The AMY Central Drift Chamber.

parallel to the beam direction (the z-axis) for measuring the $r-\phi$ coordinates of trajectory points; the other 15 cylinders (containing 3432 cells) have wires at a small angle (typically 5°) relative to the beam direction to provide small angle stereo measurements of z-coordinates. The CDC is filled with HRS gas (Ar 89%, CO_2 10%, CH_4 1%) at atmospheric pressure.

The chamber configuration consists of six cylindrical bands of different lengths. This band structure is designed to provide local determinations of track vectors (position and direction), in order to provide quick estimates of multiplicity and momenta of the charged particles for triggering the data-acquisition system, and also to facilitate fast, efficient, and precise measurement of the tracks in the complicated events with high multiplicity. The hexagonal shape of the cells, in addition to realizing the high granularity and quick resolution of the left/right ambiguities, is instrumental in achieving a good spatial resolution in the presence of the high 3 tesla magnetic field, where the Lorentz angle can be as large as 80°.

A procedure of calibration of the detector and the method of reconstructing charged tracks are described in Appendices.

The current spatial resolution of the CDC is $\sigma \sim 170$ μm, resulting in a momentum resolution of $\Delta p_t/p_t \simeq 0.7\%\ p_t(\mathrm{GeV/c})$ for tracks with $|\cos\theta| < 0.87$. This was estimated from Bhabha scattering events ($e^+e^- \to e^+e^-$).

2.2.2 The Shower Counter

Radially outside of the CDC is the Shower Counter (SHC) [48], used for detecting and measuring electromagnetically showering particles. The SHC is made of six azimuthally separated detectors, each called a sextant. Each sextant consists of twenty layers of lead sheets and gas proportional tube planes made of resistive plastic (Figs. 2.5). The proportional tubes are filled with gas at atmospheric pressure (HRS gas for the 55 GeV data run and a Ar 49.3% + C_2H_6 49.3% + C_2H_5OH 1.5% composite for the other energies). The device fully covers the angular region $|\cos\theta| < 0.73$ with a thickness of $14.5/\sin\theta$ radiation lengths. Signals from the SHC are read out both from the anode wires and from the orthogonal cathode strips. They are measured and digitized by FASTBUS ADC modules. The pedestal level of each channel is checked three times a day during the data-taking and is automatically subtracted by the ADC modules.

Twenty-four monitor tubes with embedded radioactive ^{55}Fe sources are attached to the SHC and their data are used to correct the SHC signals for the variation of gas gains due to fluctuations of pressure, temperature, and gas composition. Other detector corrections such as the correction for dead/noisy channels, the correction for different high voltage values used for part of the detector, and the subtraction of the cross-talk signals, are also carried out in the offline analysis.

The cathode strips provide measurements of the shower location with a precision of 3 mm ($\sim$ 4 mrad in angle), reducing the misidentification of pions as electrons due to the accidental overlapping of γ-rays with charged tracks. The method we utilized for reconstructing clusters of shower energies in the cathode

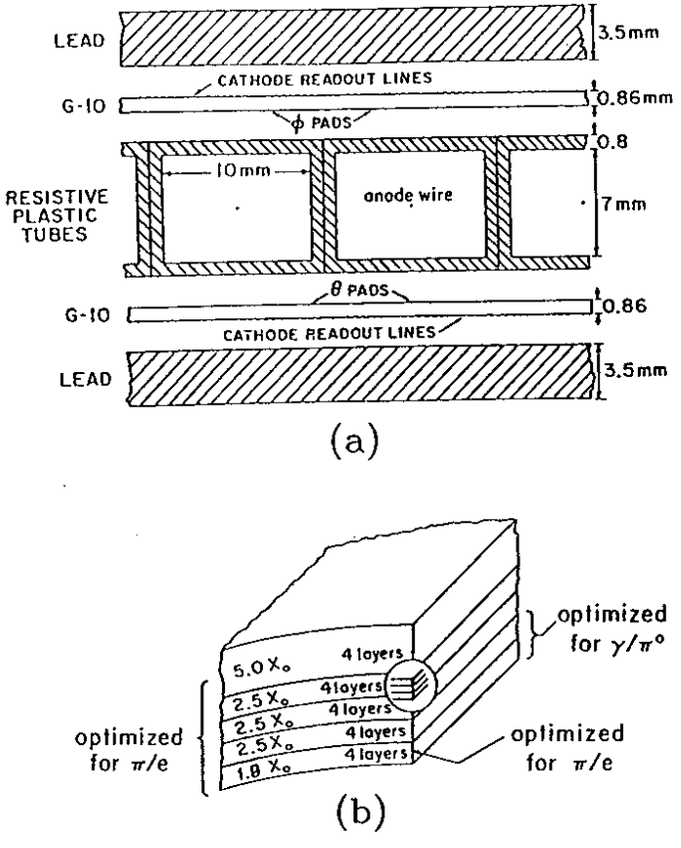

Figure 2.5: The AMY Shower Counter; (a) the layer structure and (b) the longitudinal segmentation.

strips and thus determining energies and positions of the showering particles is detailed in Ref. [49]. The electron identification efficiency in the multi-hadronic events is estimated to be 70–87%, depending on whether it is in the jet or isolated, for an electron with energy larger than 2.5 GeV; the pion rejection factor is approximately 100 [49]. The energy resolution of the SHC has been determined using the reactions, $e^+e^- \to e^+e^-$, $e^+e^- \to \gamma\gamma$, $e^+e^- \to e^+e^-\gamma$, and $e^+e^- \to e^+e^-e^+e^-$, and is found to be $\sigma_E/E \sim 23\%/\sqrt{E(\mathrm{GeV})} + 6\%$.

2.2.3 The Superconducting Magnet

The three-tesla magnetic field is produced by an eight-layer coil, made of a Nb/Ti superconducting cable that has both Cu and Al included for stabilization, that is embedded in a hexagonal iron return yoke [50]. This is an essential component of the AMY detector, for it is the strong magnetic field that allowed us to keep the size of the detector small and still achieve good momentum resolution. In addition, the strong field provides the means for electron identification by tagging synchrotron Xrays that they radiate while bending in the 3-tesla field. Because all of the detection devices, with the exception of the muon identification system, are inside the coil, no efforts for minimizing the coil thickness were necessary and a conventional method for cooling the coil was adopted; the whole volume of the coil is placed in a liquid helium bath that is kept at 4.2K. A 5000-ampere electric current provides the 3 Tesla field; the stored energy is 40 mega-joules.

We measured the magnetic field along the beam line with all the detector components in place and compared the result with a calculation done using the computer program POISSON [51]. They agree within an error of $\pm 0.3\%$ after proper normalization (Fig. 2.6). The field strength inside the detector is then estimated by POISSON, which is expected to give an error of less than 0.4% inside the tracking devices.

There is sizable non-uniformity in the field strength. Figs. 2.7 (a) and (b) show magnitude of its deviation from the central value. The variation inside the volume of the tracking devices ranges from $+5\%$ to -18%, which might seem to make precise tracking rather difficult. However, as described in the appendices, by making careful corrections, we have achieved high resolution measurements of the trajectories of charged particles.

2.2.4 The Muon Identification System

Located outside of the SHC is the 3 tesla magnet and its iron return yoke. The material in these items together with that of the SHC amounts to 1.3 kg/cm^2, (the equivalent of 1.6 m of iron), which corresponds to about nine absorption lengths for strongly interacting particles. Thus, any charged particle that penetrates this material is very likely to be a muon. Particles penetrating this material (the "hadron filter") are detected by the muon identification system (MUO), consisting of four layers of drift chambers and one layer of plastic scintillator, situated outside of the iron return yoke and covering the angular region $|\cos\theta| <$

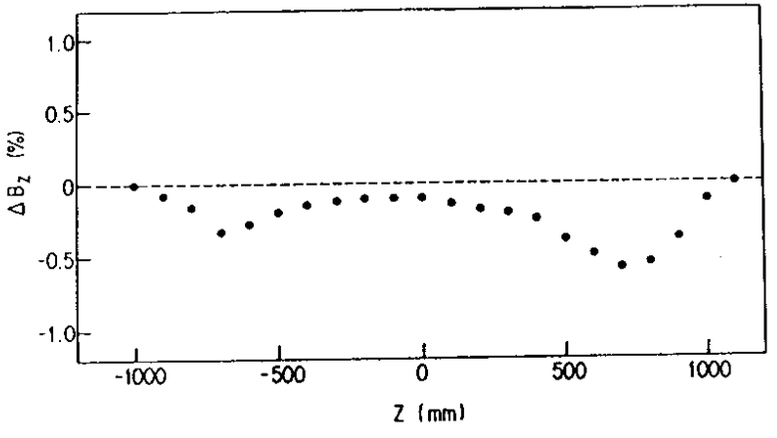

Figure 2.6: A comparison between the magnetic field along the beam axis as determined from the POISSON calculation and from a measurement. B_z(POISSON)-B_z(measured) is plotted.

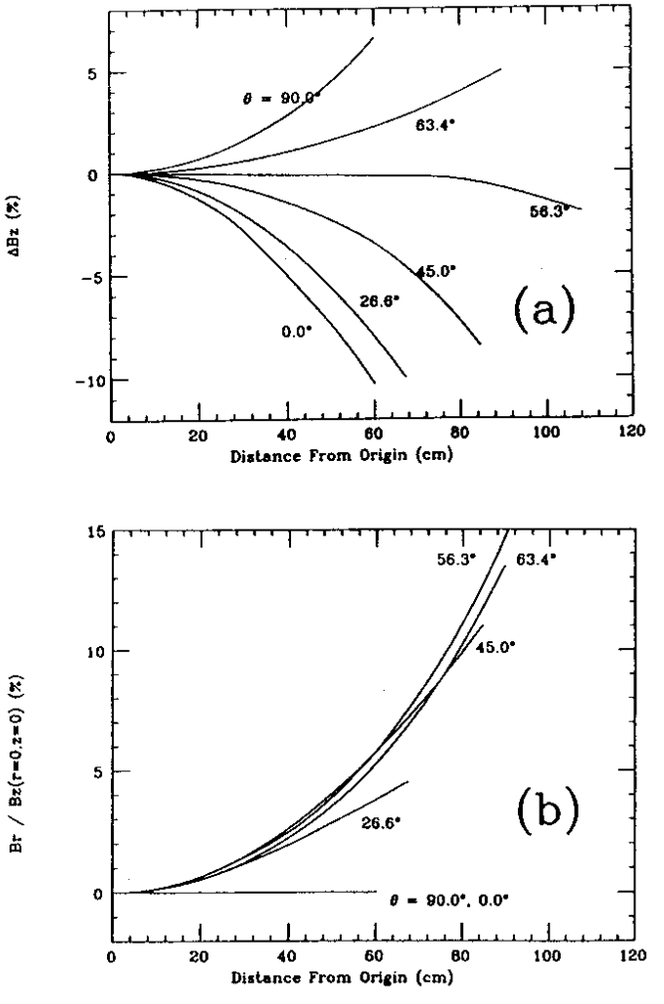

Figure 2.7: The variation of the field strength. (a) The variation in the z-component (the beam direction) of the field. (b) The variation in the radial component.

0.74. The chambers (Fig. 2.8) have a 5 cm × 10 cm cross-section with lengths ranging from 2.9 to 6.5 m and provide spatial resolution of roughly 1 mm. The combined system has a track segment reconstruction efficiency that is more than 98%. Scintillation counters, located just outside the drift chambers, measure the time of penetrating particles relative to the beam crossing time with a precision of ~3 ns, providing discrimination against backgrounds from cosmic rays that are randomly distributed in time. Muons are identified as those particles whose trajectory, when extrapolated through the material of the hadron filter, pass within 1 m in space and 50 ns in time of a track segment as measured in the muon identification system. We estimate the probability for a 5 GeV/c (10 GeV/c) π-meson to penetrate the hadron filter and be mis-identified as a muon to be 0.2% (0.5%). An advantage of the compactness of AMY detector is that fake muon backgrounds due to the decay-in-flight of pions and kaons are minimized; it occurs at the level of $\simeq 1.3\%/p(\mathrm{GeV/c})$ for pions and $\simeq 6\%/p(\mathrm{GeV/c})$ for kaons. With the current scheme of muon identification, the muon identification efficiency is about 96% for $p > 3.0$ GeV/c (82% for $p > 2.0$ GeV/c), and the background contamination for the muons in the multi-hadronic events is estimated to be less than 35%.

2.2.5 The Endcap Detectors

The CDC provides good momentum resolution over the angular region $|\cos\theta| < 0.87$; the SHC and the muon system covers $|\cos\theta| < 0.73$. Particles that are produced at smaller angles, in the region of the pole tips of the magnet's iron return flux, are detected in the Pole Tip Counter (PTC), which covers the region $14.6° < \theta < 26.6°$ and the Forward Tagging counters (FTC), covering $26° < \theta < 38°$.

The PTC [52] consists of two modules of lead/scintillator calorimeters with a total thickness of 14 radiation lengths with a plane of proportional tubes sandwiched between them. It measures the energies and positions of electrons and photons and the positions of charged particles. Its primary function is the determination of the luminosity by detecting Bhabha scattering events. The energy resolution for 28 GeV/c electrons (i.e., Bhabha electrons) is 11%. The position resolution is about 0.2° and 0.8° for θ and ϕ directions, respectively.

The Forward Tagging Counter (FTC) consists of two layers of lead and scintillators (1 cm + 1 cm thickness for each layer) and signals the presence of showering particles (either electrons or γ−rays) that are emitted between the SHC and PTC. The CDC tracks entering in this region are thus identified as electrons or minimum ionizing particles by comparing their energy measurements. The energy resolution for 28 GeV/c electrons is roughly 30%.

In addition, there are counters in the forward region ($\theta \sim 4.0°$) to measure instantaneous luminosity and to monitor beam-related background radiation levels.

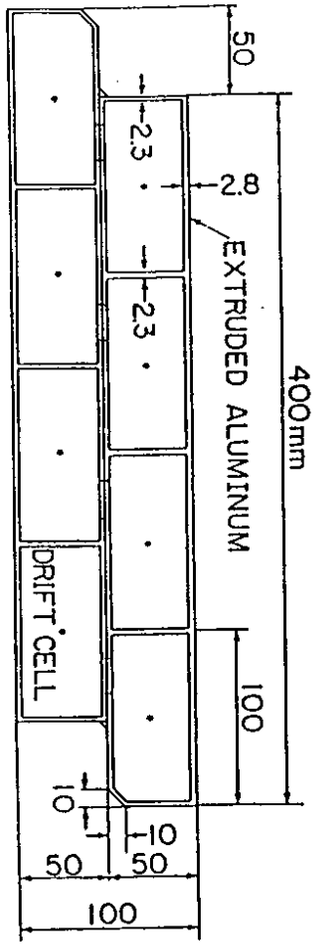

Figure 2.8: A cross-sectional view of muon chamber.

2.2.6 The X-Ray Detector and the Trigger Counters

In the early stages of the operation of the experiment, twelve scintillation counters were placed in the space between the CDC and SHC for triggering and for discriminating background events. These were replaced by the X-Ray Detector (XRD) in summer, 1987. The purpose of the XRD, which is a drift chamber filled with Xenon gas, is to detect the synchrotron X-rays radiated by electrons as they bend in the 3 Tesla magnetic field. This will be used in conjunction with the SHC to provide high quality electron identification. No data from XRD is yet available for the analysis reported here.

2.2.7 Data Acquisition System

The data acquisition system for the detector is schematically illustrated in Fig.2.9.

The frequency of beam crossings at TRISTAN is 200 kHz and the maximum data acquisition rate is 3 Hz. Thus, at the time of each beam crossing, a decision must be made within 5 μsecs as to whether or not an event of possible interest has occurred. If the decision is yes, the data acquisition system is triggered. The trigger logic system must select interesting events with very nearly 100% efficiency while rejecting uninteresting crossings at the level of 100,000 to 1. The first quick decision for triggering the data acquisition system is made in ≤ 1.5 μsecs, well within 5 μsecs, and then more elaborate judgement follows. In order to be sensitive to as many e^+e^- processes as possible, the trigger requirements for the detector are kept as loose as possible, consistent with the maximum possible 3 Hz. As a result, we typically accumulate approximately 5,000 events/hour, of which only one or two are actual multi-hadronic annihilations.

A computer-controlled FASTBUS system is utilized to read and digitize analog signals from the SHC, PTC, FTC, and ITC, and timing signals from the CDC, ITC, and MUO. Triggers, chamber high voltage control, and environmental monitors are all controlled and monitored by means of a CAMAC system. All the digitized data are read in by a VAX-11/780 computer, where they are temporarily stored. Here, various checks are made to monitor operation of the entire detector system. The data are then sent via an optical link to a FACOM M382 computer, where the data format is immediately rearranged for the convenience of later analyses. The data are stored in a cassette-tape library; from there it is accessed for subsequent detailed offline analysis.

2.3 Monte Carlo Simulation

The complexity of our detector and the large variety of final states produced in e^+e^- annihilation processes precludes the possibility of using a simple analytic formula for computing the detector's acceptance with any precision. Instead, we use Monte Carlo (MC) simulation methods to estimate the detection efficiency and the response of our detector to multi-hadron events and various background processes. There are two stages in the MC simulation of physical processes:

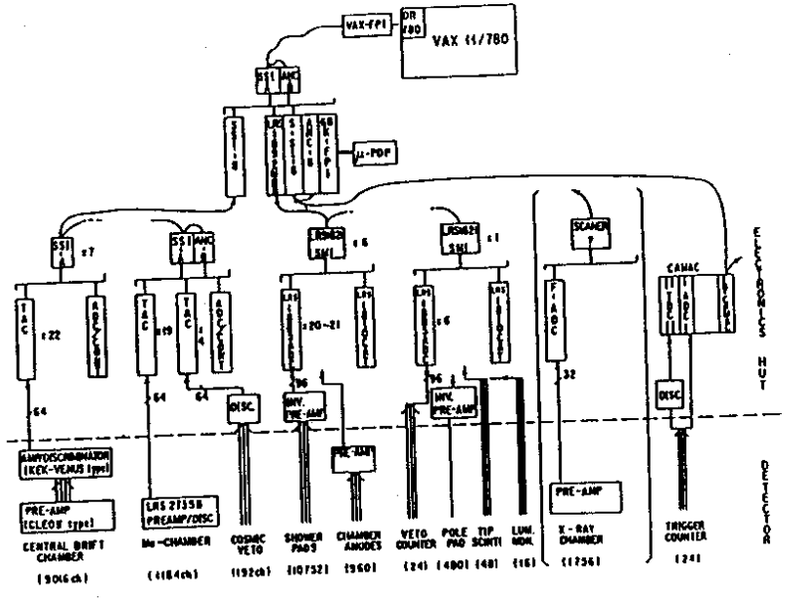

Figure 2.9: Schematic diagram of the AMY data acquisition system.

1. the event generation stage; here an "event" is generated, i.e., species and four-momenta of the final state particles from a particular type of e^+e^- process are produced by MC methods that are based on theoretical models;

2. the detector simulation stage; here we simulate responses of our detector to the particles generated in the first stage, formatting the results in the same way as is done for the actual experimental data so that they can be analyzed by the same data analysis programs.

We will describe, in the following, how these two stages are treated for the analysis presented here.

2.3.1 Event Generation

Discussed below, according to the types of physical processes, are the theoretical ideas and calculations used to generate events of interest. Computer programs that are actually used for event generation are briefly explained and possible sources of ambiguities are pointed out.

Hadronic Event

In general, a hadronic event generator creates a quark-antiquark pair from the e^+e^- annihilation according to the standard electroweak theory.

The quark and/or the antiquark may, then, radiate gluons, and the radiated gluons may radiate another gluons or convert into another quark-antiquark pair. There are essentially two methods to formulate this consecutive development of quarks and gluons (partons).

One is the matrix element method, where the cross sections are calculated up to a certain order of α_S using perturbative QCD, and events are generated according to the calculated cross sections. This method has a drawback that calculations up to many orders of α_S have to be carried out in order to simulate events with many partons in the final state, i.e., events with many jets of hadrons. The event generators we use in our analysis include calculations up to $O(\alpha_S^2)$, corresponding to events with four or less partons in the final states.

The parton shower method, on the other hand, generates showers of quarks and gluons through a cascade-like process. In this method, each parton branches into two partons ($q \to qg, g \to gg, g \to q\bar{q}$) with a calculated probability, resulting in the development of showers of partons, this is continued until the virtual mass of each parton reaches a certain cut-off mass ($\sim$ 1 GeV/c^2). The branching probabilities of partons are calculated in the leading logarithm approximation (LLA) of perturbative QCD, as given by the Altarelli-Parisi equations [53]. It has been proved that the perturbative parton development by LLA is equivalent to a product of the probabilities for individual branchings [54]. Although this method minimizes the ambiguous "hadronization" part by cascading down to about 1 GeV/c^2, it is based on approximate calculations only and is not applicable for large-p_t parton emission processes. A parton shower calculation based on "next-to-leading logarithm" approximation (NLL), where the next leading terms are also summed up through all orders of α_S, is becoming available [55]. Although it has not yet been demonstrated that the formulation of NLL in the parton shower method really gives a correct approximation for QCD cross sections, the NLL approximation is believed to be good even for large-p_t parton emissions and the QCD parameter $\Lambda_{\overline{MS}}$ can be defined in a definite manner.

Since what we actually observe in the detector are hadrons, not partons, the quarks and gluons generated by the Monte Carlo must be turned into hadrons. This transition process from quarks and gluons to hadrons, the so-called quark fragmentation process, involves non-perturbative aspects of QCD, for which we must use some phenomenological models.

There are essentially three different types of fragmentation models: independent fragmentation (IF), string fragmentation (SF), and cluster fragmentation (CF).

The IF model [57] lets each parton independently fragment into hadrons. A quark q is split into a hadron $q\bar{q}_1$ and a remainder-quark q_1, moving essentially in the same direction. The sharing of energy is given by a probability function $f(z)$, called a fragmentation function, where z is the fraction of the original quark's energy that is taken by the hadron. The remainder-quark q_1 is then split into a hadron $q_1\bar{q}_2$ and a quark q_2 in a similar manner, and this process is iterated, yielding a sequence of hadrons. This model failed to reproduce the correlations between particles in different jets, the so-called string effects, that were observed in three-jet events by the PETRA/PEP experiments [56].

In the SF model [58], a "string" is stretched between a quark and an antiquark with a constant force. A gluon is realized as a kink carrying four-momentum on the string. A string breaks into two strings as the quark and the antiquark move apart. The break points thus created are associated with new quarks and antiquarks. This string breaking continues to occur and mesons are formed from resulting "short" strings. The string effects mentioned above were first predicted by this model.

The CF model [59] emerged as the parton shower method was developed. It combines quarks and antiquarks into disjoint color singlet systems, called "clusters", after the parton branching stage. Usually gluons are forced to break up into a quark-antiquark pair beforehand. The clusters are then allowed to decay into (usually two) hadrons that are emitted isotropically in the rest frames of the clusters. Here the soft gluon interference is incorporated using the so-called "angular ordering" technique, this model can also reproduce the string effects.

These models are incorporated into Monte Carlo computer programs that generate hadronic events; these are used for evaluating the detector's acceptance for hadronic events. The accuracy of this procedure is checked by comparing various physical quantities in generated events with those measured in real events. Even so, different models that reproduce the general properties of the real data well may possibly give different values for the acceptance. This is probably due to the possible uncertainties in the event generation schemes (matrix element or

parton shower) and the existing ambiguities in the fragmentation models. Thus, there is a systematic error associated with the evaluation of the acceptance; an analysis of this is given in the next chapter.

We use the Lund MC program (Jetset version 6.3) [60], or Lund 6.3 for short, with the parton shower scheme and the SF model as our standard MC generator of hadronic events. The default values are used for the phenomenological parameters in the code. The generated events describes the particle distributions (Figs. 2.10) and the global distributions reasonably well. (See Fig. 3.2 in the next chapter.)

This program also has options to use the matrix element scheme and/or the IF model. In addition, we used comparisons to results obtained using the Lund 6.2 program [60] and the EPOCS program [61] to estimate systematic errors in the acceptance calculations. These can be used with either the matrix element or parton shower approach, and fragmentation can be done with either the IF or the SF model.

We also use these programs to estimate the acceptance for t quark events. Although t quarks have never been observed, the properties of those events are predicted rather unambiguously (chapter 1). In the generator programs, the produced $t\bar{t}$ are turned into a top meson pair, and the t quark (inside of the meson) decays into a b quark together with lighter quarks or leptons, with kinematics that are determined according to the standard electroweak theory. The fragmentation of the quarks and the decays of mesons follow the same procedures as are used in the light quark events. Although the general event shape of the t quark events are determined primarily by the kinematics of the weak decay of the t quarks, there is non-negligible model dependence; this will be discussed in the next chapter.

EPOCS, to which we added some modifications in order to generate b' events, is used to estimate the acceptance for the b' production events. Here the b' quark is assumed to be lighter than the t quark and thus is made to decay into the c quarks with lighter quarks or leptons, in a very similar manner to that used to generate t quark events. (See the comment in Chapter 1 concerning the possible dominant b' decay through flavor changing neutral currents [41].)

Electroweak radiative corrections are accommodated in these MC hadronic event generators up to the order of α^3 using methods developed by F.A. Berends, R. Kleiss, and S. Jadach (BKJ) [62]. In the BKJ calculations, the correction factor for radiative effects, $(1+\delta)$, is obtained from the set of the Feynman diagrams shown in Fig. 2.11. These diagrams, however, do not compose a complete set of order of α^3 electroweak corrections. The diagrams omitted involve virtual weak boson propagators or corrections to quark vertex as indicated in Fig. 2.12. The BKJ calculations, though incomplete, have been widely used by many PEP and PETRA experiments.

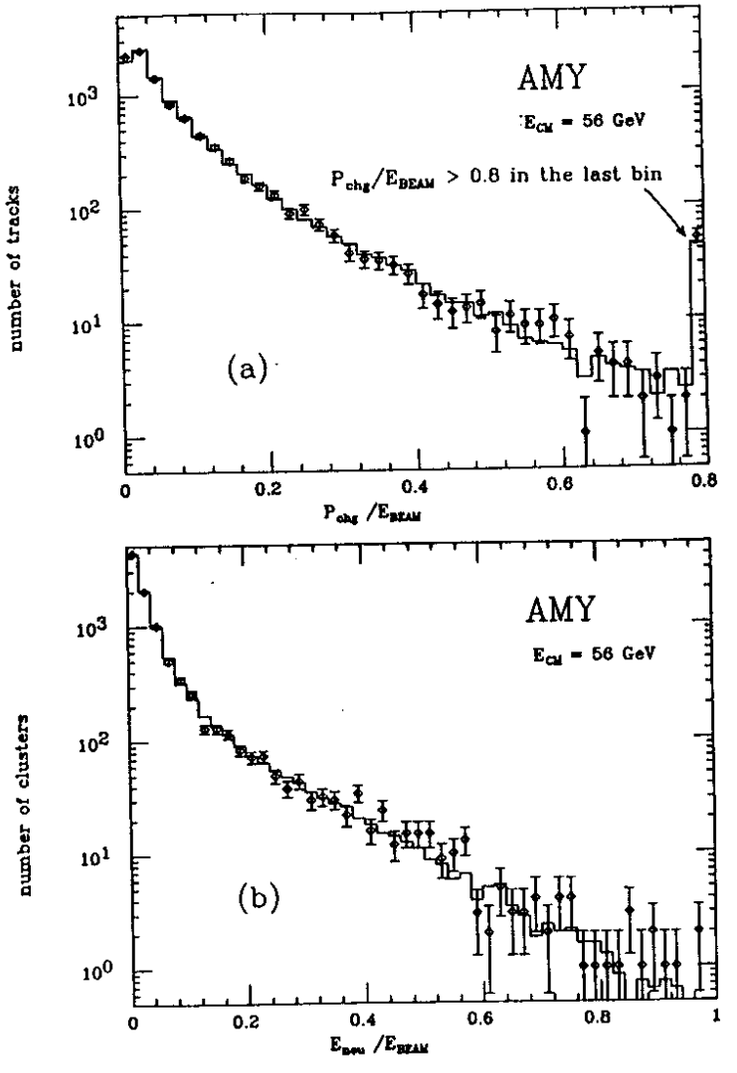

Figure 2.10: The momentum distributions of charged particles (a) and of neutral particles (b) for the real data (points) and the data generated by Lund 6.3. (histogram) for 56 GeV.

J. Fujimoto, K. Kato, and Y. Shimizu (FKS) calculated the full electroweak radiative corrections up to the order of α^3, including all the diagrams shown in Figs. 2.11 and 2.12, using the on-shell renormalization scheme (chapter 1) [63]. Their calculations were formulated with a numerical integration package, BASES [68], that we use to evaluate the effects of the diagrams omitted in the event generators. The omitted contributions are all virtual and small and, thus, their effect on the detector's acceptance (ϵ) is negligible. On the other hand, their effect on the correction factor $(1 + \delta)$ can be sizable. The radiative corrections obtained by the FKS calculations are found to be about 0.9% larger than those obtained by the BKJ calculations at $\sqrt{s} = 57$ GeV, and about 3% larger at $\sqrt{s} = 60$ GeV (Fig. 2.13). We also confirm that the FKS calculations come to agree with those of BKJ within 0.2% if we confine ourselves to only those corrections used by BKJ. For the calculations, we use $M_{Z^0} = 92.0$ GeV/c^2, $\Gamma_{Z^0} = 2.5$ GeV, $m_t = 45.0$ GeV/c^2, and $m_H = 100$ GeV/c^2. In terms of the formalism introduced in Chapter 1, these values correspond to $\Delta r = 0.070$, $M_W = 80.79$ GeV/c^2, and $\sin^2\theta_W = 0.229$ [17]. The value of $(1 + \delta)$ is insensitive to these parameters.

Two-Photon Hadronic Event

The two-photon hadronic process [64], $e^+e^- \rightarrow e^+e^- + hadrons$, is one of the main background sources in the hadronic event sample. Because it is impossible to completely separate these events from hadronic events, we estimate the fraction of the background contamination by using MC generated two-photon events and subtract it statistically.

This process is well described by the quark parton model prediction (QPM) plus the vector dominance model prediction (VDM) [65] provided that the VDM prediction is properly normalized [66]. The relevant Feynmann diagrams for the QPM calculations of this process are shown in Fig. 2.14; here the dominant contributions come from the diagrams that have collisions between two virtual photons (therefore the name "two-photon" hadronic events). Although this process is of order of α^4, the cross section is large because one of the virtual photons is usually almost on shell. The hard component of the two-photon process is described by the QPM.

The VDM process is shown in Fig. 2.15, where hadronic components of the virtual photons, i.e., virtual vector mesons, collide each other. The cross section is evaluated with an equivalent photon approximation [67], which has some ambiguity in the normalization. We estimate a systematic error due to this ambiguity by comparing to our experimental data. The VDM process corresponds to a soft component of the two-photon process.

In addition, the contributions of multi-jet production processes in two-photon collisions (MJP), motivated by the small discrepancy observed by the PLUTO collaboration [69], have been recently calculated [70].

To estimate the background in our hadronic event sample, we sum up these three different components, using a computer code, written by J. Smith [71], that generates events of the VDM and the MJP types. The programs BASES

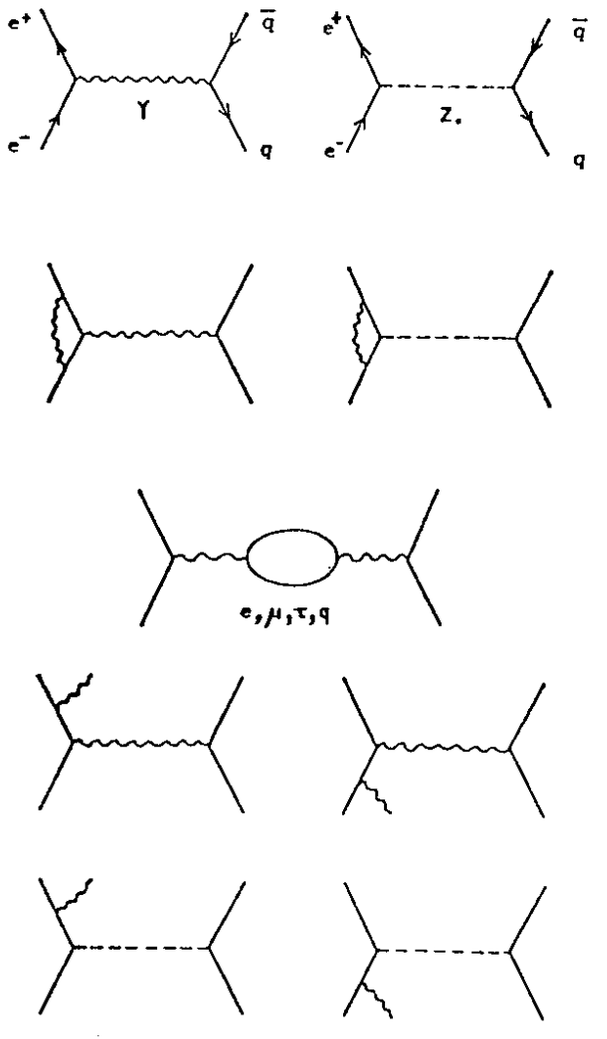

Figure 2.11: The Feynman diagrams used for the BKJ radiative corrections.

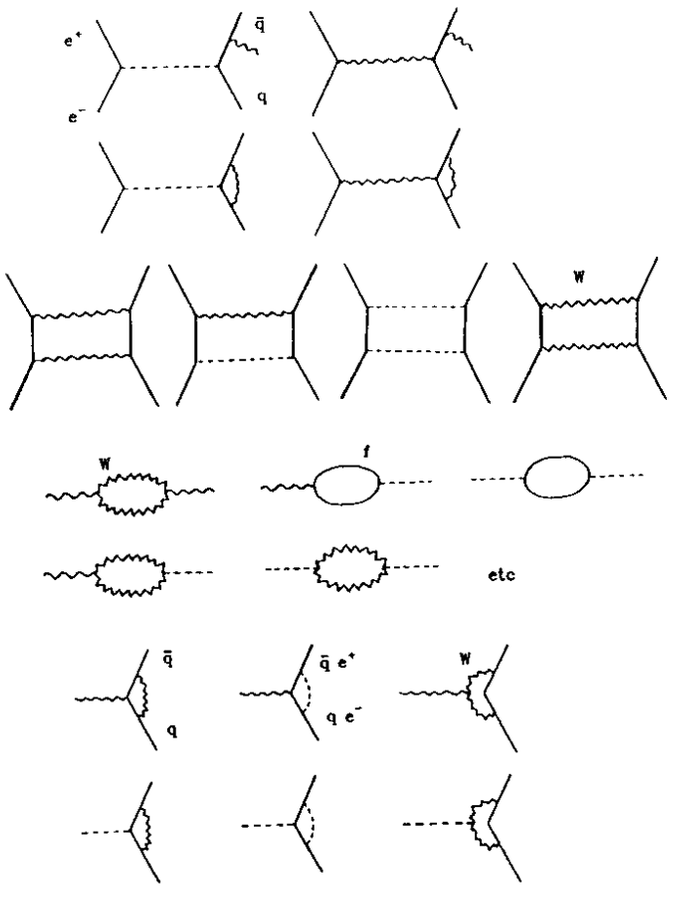

Figure 2.12: The Feynman diagrams omitted for the BKJ radiative corrections.

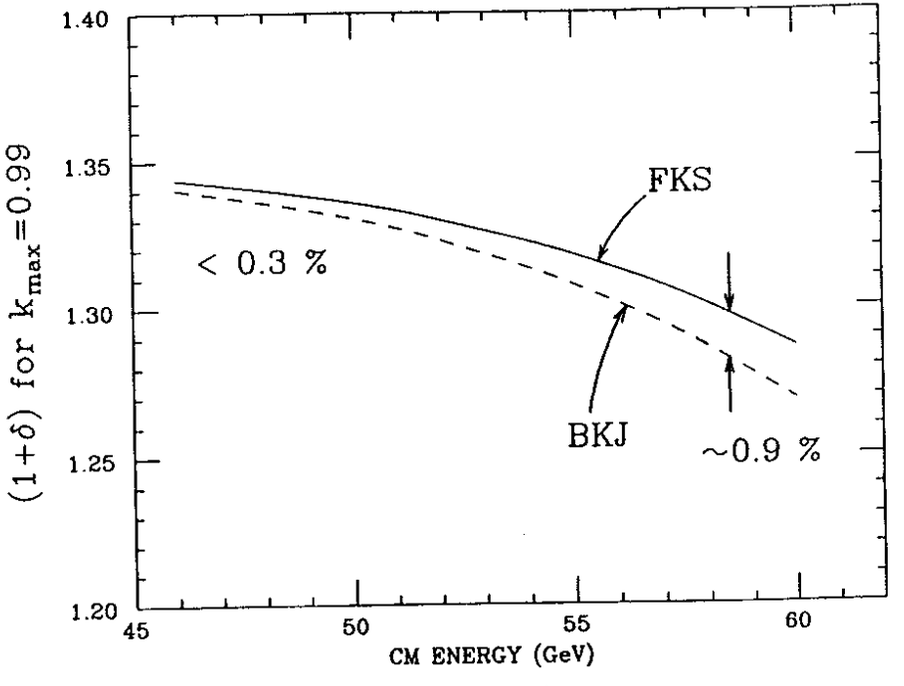

Figure 2.13: Radiative correction factor with the FKS calculation compared to that of BKJ (as incorporated in Lund 6.3). Here, k_{max} is set as 0.99.

and SPRING [68] are used to generate events according to the differential cross section of the QPM component [64].

Tau-Lepton Pair Creation

The process $e^+e^- \to \tau^+\tau^-$ is another possible background source, since τ's predominantly decay into final states containing hadrons. The background is not too severe since the charged particle multiplicity in τ decays is usually quite low (< 5).

The differential cross section for this process is reliably calculated by the standard electroweak theory. EPOCS is used to generate the events and the experimentally known branching ratios for the τ decays are used.

2.3.2 Detector Simulation

Our detector simulation program simulates the interactions and decays of the particles that are generated by the event generator and models detector signals according to our best knowledge of the detector system. In the detector simulator, each particle is "swum" through the detector in small steps. At each step, the particle is allowed to decay or undergo an interaction according to the known probabilities, by means of MC techniques. A charged particle loses its energy through ionization processes in material, and may change its direction by the multiple Coulomb scattering. Its trajectory is bent as it moves under the influence of the magnetic field, and electrons can emit bremsstrahlung photons. Photon may convert into an e^+e^- pair in material, while hadronic particles may undergo nuclear interactions. All these probabilistic processes are included in the calculation.

Electromagnetic showers initiated by photons and electrons inside dense material (e.g. the SHC or the PTC) are developed by the simulation program EGS4 [72]. Hadrons may cause hadron showers inside the iron yoke, which are treated by the program package GRANT [73].

Inside the CDC, as a charged particle passes through one of the wire cells, the closest distance of the particle to the sense wire is determined and converted into a drift time by using the nominal drift velocity of the ionization electrons. Here the drift distance is smeared by the known spatial resolution of the chamber. If more than one charged particles pass through the same cell, only the shortest drift time is recorded.

We have a choice of two different smearing methods. The first (and simplest) one assumes a Gaussian distribution for the spatial resolution, and the resolution is taken as a constant throughout the chamber. For the second method we add a long tail to the Gaussian resolution distribution and different spatial resolutions are used for different positions in the cell. The chamber efficiencies, which are assumed to vary from layer to layer, are also taken into account. The parameters of the simulator are tuned according to the real data.

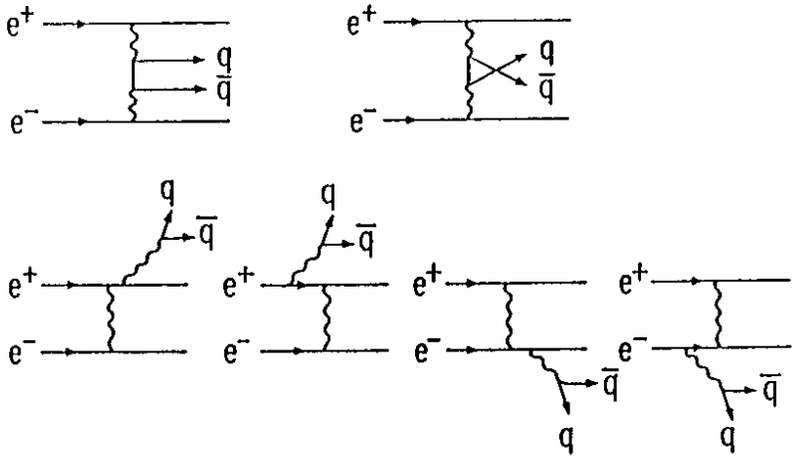

Figure 2.14: Feynman diagrams for the QPM calculations of two-photon hadronic events.

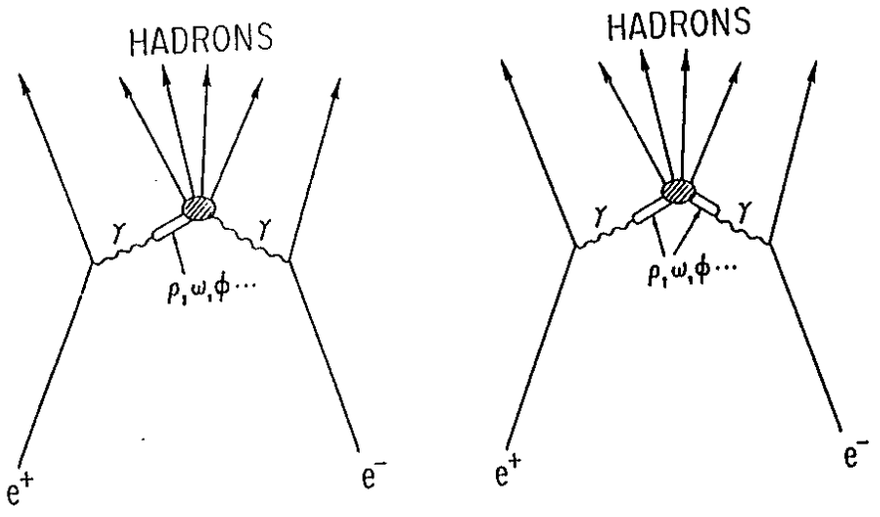

Figure 2.15: The diagrams for the VDM calculations of two-photon hadronic events.

Inside the SHC, the EGS4 code is used to develop electromagnetic showers and to calculate deposited energies. These energies are converted into ADC counts for the corresponding cathode strips and anode wires according to the calibration data of the SHC.

All the detector signals thus obtained are formatted in the same way as the real data, and are subjected to the same analysis programs that analyze the real data.

2.4 Data Sample

The data sample we use for the analysis here were accumulated between May, 1987 and July, 1988, corresponding to all of the physics data taken by summer, 1988. As shown in Fig. 2.16, the 50 GeV data were taken in May, 1987; the 52 GeV data in June and July, 1987; the 55 GeV data in October – December, 1987; the 56 GeV data in January – March, 1988; the 56.5 and 57 GeV data in June and July, 1988.

The integrated luminosities for individual energy points are (errors are statistical only) 0.64 ± 0.02 pb^{-1} for 50 GeV, 3.98 ± 0.04 pb^{-1} for 52 GeV, 3.27 ± 0.04 pb^{-1} for 55 GeV, 5.99 ± 0.05 pb^{-1} for 56 GeV, 0.99 ± 0.02 pb^{-1} for 56.5 GeV, and 4.40 ± 0.05 pb^{-1} for 57 GeV; amounting to 19.3 pb^{-1} in total.

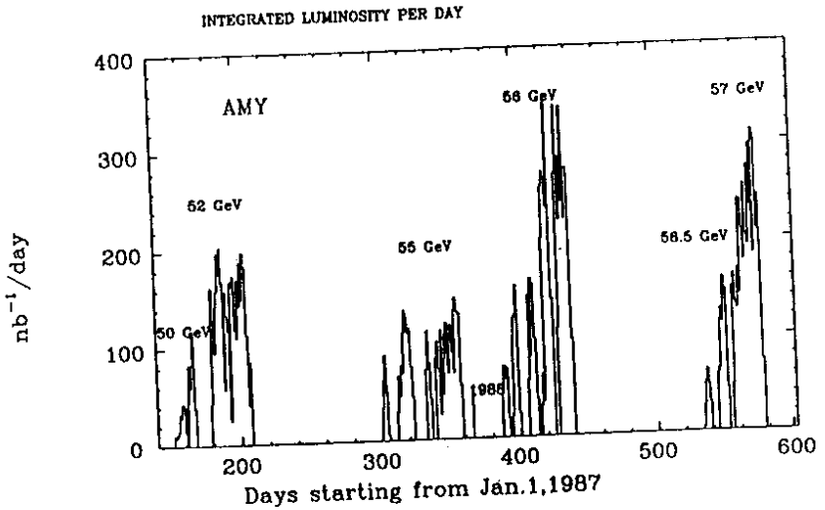

Figure 2.16: Average daily integrated luminosities from January 1987 to July 1988.

Chapter 3

Total Hadronic Cross Section

In order to determine the total cross section for multi-hadronic annihilation, we must ensure that the detector is triggered efficiently by such events, that the luminosity is monitored accurately, and that events are selected efficiently. In addition, corrections for acceptance, background, and higher-order radiative effects must be estimated. In this chapter, procedures and results for the total cross section measurement are described.

3.1 Triggers

We used several different types of triggers to detect hadronic events. They are: (1) shower energy triggers formed from energy measurements in the SHC; (2) triggers based on the numbers of charged track segments in the different bands of the CDC; (3) triggers based on track configuartions in the ITC; and (4) various combinations of the SHC energy and the CDC and ITC tracks. Among these triggers, types (1), (2), and (3) are completely independent of each other. The trigger requirements for these three trigger types are, respectively:

- SHC energy trigger
  - total SHC energy is greater than (approximately) 3 GeV.
  - number of SHC towers with deposited energy greater than 1.5 GeV is two or more.
- CDC track trigger
  - five or more CDC track candidates.
- ITC track trigger
  - Six or more tracks in the ITC.

After the final selection of hadronic events (the selection procedure is described in section 3.3), we cross-checked the trigger efficiencies for hadronic events by comparing the yields for the different independent trigger types. The upper limits for the inefficiencies so obtained, summarized in Table 3.1, are all less than

$\sqrt{s}$(GeV)	50, 52	55	56	56.5, 57
SHC	10.2 ± 1.2	60.3 ± 2.5	23.43 ± 1.6	20.6 ± 1.6
CDC	4.38 ± 0.86	2.72 ± 0.85	3.44 ± 0.68	2.28 ± 0.60
ITC	32.5 ± 1.9	31.3 ± 2.4	31.2 ± 1.7	28.8 ± 1.8
SHC*CDC*ITC	0.15 ± 0.04	0.51 ± 0.17	0.25 ± 0.06	0.13 ± 0.04

Table 3.1: Upper limits for trigger inefficiencies (%) for hadronic events for the three independent triggers. The errors shown are statistical (1σ).

1 %. Since, in addition to these basic triggers, we have other triggers formed from various combinations of the SHC, the CDC and the ITC, the actual inefficiencies are probably lower than these upper limits. An elaborate analysis including some of the other triggers showed that the inefficiencies are less than 0.3%. Therefore, we confidently conclude that the trigger inefficiency for hadronic events has only a negligible effect on our analysis of hadronic events.

3.2 Luminosity Measurement

Small angle Bhabha scattering, $e^+e^- \rightarrow e^+e^-$, which is dominated by t-channel single photon exchange, is the least ambiguous e^+e^- reaction (both theoretically and experimentally) and, thus, has traditionally been used to monitor the luminosity in high energy e^+e^- colliding beam experiments. Detailed theoretical calculations for Bhabha scattering, including higher order radiative corrections (up to $O(\alpha^3)$) in the standard model, have been carried out [74].

Electrons and positrons from the Bhabha process are detected by the SHC in the barrel region and the PTC and FTC in the endcap region. The luminosity is determined by a comparison of the calculated and the measured cross sections in these three devices. We find that the measured angular distribution for Bhabha events agrees reasonably well with the theoretical prediction and the luminosities inferred from the different detection elements are consistent with each other (see Fig. 3.1). We also inferred a luminosity from the measurement of the reaction $e^+e^- \rightarrow \gamma\gamma$. The results, shown in Table 3.2, agree well with those derived from Bhabha scattering. For the cross section determination, we use the luminosity values obtained from Bhabha scattering in the PTC; these, listed in Table 3.4, have the smallest statistical errors.

The estimated systematic errors for luminosity measurements range from 3.3% to 3.7% and are summarized in Table 3.5. The largest error comes from the few millimeter uncertainties in the PTC alignment relative to the beam crossing point.

The position of the PTC along the beam direction was determined with an accuracy of 5 mm, corresponding to an error of 0.08° in theta angle, resulting in a 1.8% uncertainty in the luminosity. The range of accepted Bhabha scattering

$\sqrt{s}$ (GeV)	Barrel Bhabha (pb^{-1})	Barrel $\gamma\gamma$ (pb^{-1})	PTC Bhabha (pb^{-1})
50	0.60 ± 0.04	0.52 ± 0.10	0.64 ± 0.02
52	3.88 ± 0.10	3.89 ± 0.29	3.98 ± 0.04
55	3.42 ± 0.10	3.26 ± 0.28	3.27 ± 0.04
56	6.06 ± 0.13	6.55 ± 0.40	5.99 ± 0.05
56.5	1.05 ± 0.06	0.83 ± 0.14	0.99 ± 0.02
57	4.44 ± 0.12	5.40 ± 0.37	4.40 ± 0.05

Table 3.2: Comparison of luminosity measurements by different devices. Only statistical errors are listed.

angles was known to 0.1°, corresponding to a 2.4% uncertainty in luminosity. These uncertainties in radial and z- directions are summed in quadrature to give an overall 3.0% systematic error arising from uncertainties in the alignment. For a period of time during the 52 GeV running, a section of the PTC proportional chambers was not operational, resulting in an additional systematic error of 1.7% due to the uncertainty in position measurement.

More details of the analysis of luminosity and Bhabha scattering can be found in Ref. [75].

3.3 Hadronic Event Selection

In the first stage of the event selection procedure, all of the recorded events are passed through a two-step software filtering procedure. The first step utilized various cuts on detector signals to reject events which are obviously not e^+e^- annihilations. Here, the cluster-finding algorithm for the SHC is applied and the energies of the SHC clusters are determined using a coarse SHC calibration. Charged track segments in the CDC are reconstructed and the multiplicity and momenta of the charged tracks are estimated. Events that have more than 2.8 GeV of energy deposited in the SHC, or have at least one high-momentum ($P_t > 1.5\text{GeV}/c^2$) or two or more charged tracks in the CDC and more than 1.5 GeV of SHC energy, are accepted. This pass rejects many of the events that are caused by interactions between beam particles and the nuclei of the residual gas in the vacuum system (beam-gas interactions) or by interactions of particles in the beam-halo with the walls of the vacuum system (beam-wall interactions). This first step eliminates about half of all of the recorded events.

Subsequently, the fast track recognition program ACE (see Appendix B) is used to reconstruct the trajectories and determine the momenta of the charged particles.

To pass the second step, events have to satisfy the following conditions:

- Number of "good-vertex tracks" is three or more, where a good-vertex track

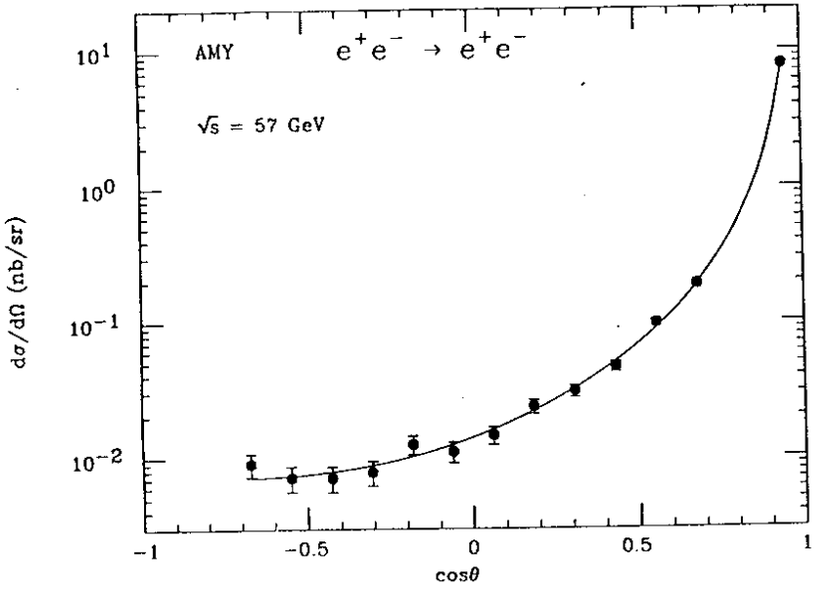

Figure 3.1: The differential cross section of Bhabha scattering, $e^+e^- \rightarrow e^+e^-$. The line is the prediction of the Standard Model. The experimental data are normalized by the PTC data (most forward point).

is defined to be a CDC track with $|R_0| \leq 5$ cm and $|Z_0| \leq 10$ cm. Here R_0 and Z_0 are r- and z-component of the distance of closest approach of the track to the beam interaction point, respectively.

- Total deposited energy in the SHC is greater than 2.8 GeV. This cut is made as loose as possible and consistent with keeping the size of the resulting data sample manageably small.

The resulting event sample is then subjected to a more intensive track finding algorithm, DUET, (see Appendix B) and the SHC cluster-finding algorithm is again applied using a more accurate SHC calibration. This sample is used as the basic data sample for all subsequent analyses for hadronic processes.

In order to investigate possible biases in the selection procedure, part of the selected data sample was visually scanned by physicists using an interactive graphics program, AMYSCAN. (Examples of the event displays of AMYSCAN are shown in Figs. 3.3–3.5.) No evidence of a bias was found. (Visual scanning was used frequently to help us improve the detector analysis programs and determine the cuts that were used for selecting hadronic events.)

Background events still dominate this basic sample. These backgrounds include:

- two-photon collision hadronic events ($e^+e^- \rightarrow e^+e^- + \textit{hadrons}$),
- τ lepton pair production ($e^+e^- \rightarrow \tau^+\tau^-$),
- radiative Bhabha events ($e^+e^- \rightarrow e^+e^- + \gamma$) where the γ ray converted into an e^+e^- pair in the material of the vacuum pipe,
- beam-gas and beam-wall interaction events, and
- cosmic ray shower events.

The multi-hadronic annihilation process, $e^+e^- \rightarrow \textit{hadrons}$, has a number of characteristic features. Since these events tend to be collimated as jets, whose angular distribution is expected to be approximately $(1 + \cos^2\theta)$, many hadronic events have almost all of the final-state particles detected in the barrel part of our detector, i.e., the CDC and the SHC. In these cases, the total energy deposited in the barrel part should be nearly equal to the center-of-mass energy, $\sqrt{s}$, and the momenta of all the detected particles should be balanced. In addition, extrapolating results from previous, lower-energy e^+e^- experiments [2] leads us to expect that the average multiplicity of charged particles at our energy will be large ($\simeq 15$).

Based on these considerations, we define the following "event selection variables" for use in the isolation of hadronic events:

- The visible energy, E_{vis}, defined as a sum of absolute momenta (or energies) of all the "good" CDC and SHC particles ($E_{vis} = \sum_{i=CDC} |P^i| + \sum_{j=SHC} E^j$).

- The momentum balance, P_{bal}, the sum of the z-components of the three-momenta of all the "good" CDC and SHC particles ($P_{bal} = \sum_{i=CDC} P_z^i + \sum_{j=SHC} E^j cos\theta_j$).
- The number of charged particles, N_{chg}, i.e., the number of "good" CDC tracks.
- The total energy deposited in SHC, E_{SHC}. For this, the energies of all SHC clusters are summed; no distinction between "good" and "no-good" clusters is made.

Here a "good" CDC track must have at least 8 axial and 5 stereo hits, and have a good "vertex", i.e., $|R_0| < 5$ cm and $|Z_0| < 15$ cm. Slightly tighter cuts are used for high momentum tracks: either $|R_0| \leq 1$ cm or axial hits ≥ 12 or stereo hits ≥ 10 for tracks with $P > 0.25\times$(beam energy), and either $|R_0| \leq 2$ cm or axial hits ≥ 12 or stereo hits ≥ 10 for tracks with $P > 0.5$ GeV/c.

A "good" SHC cluster is one with energy greater than 0.2 GeV and less than 95 % of its energy deposited in any one of the five longitudinal layers of the SHC. In order to avoid double counting of a charged particle by the CDC and the SHC, a SHC cluster with its energy less than 1 GeV is not regarded as a "good" one if its position matches with a CDC track within 2°. High energy SHC clusters ($E_{SHC} > 1$ GeV) that match with CDC tracks are either electrons, γ rays accidentally overlapped by charged hadrons, or hadrons that interact in the material of the SHC. Because discrimination of electrons from γ-overlapped hadrons or interacting hadrons depends on the details of our electron identification criteria, we decided to allow for double counting for $E_{SHC} > 1$ GeV. It was found from Monte Carlo studies that this does not effect the results of event selection; the number of selected events changes by only 0.2~0.3 % between using and not using the double counting.

In order to reject background events while keeping most of the hadronic events in the sample, the following "hadronic event cuts" are applied:

$$\text{hadronic event cuts} = \begin{cases} E_{SHC} > 5 \text{ GeV} \\ E_{vis}/\sqrt{s} > 0.5 \\ N_{chg} \geq 5 \\ P_{bal}/E_{vis} < 0.4 \end{cases} \tag{3.29}$$

Here, because the earlier $E_{SHC} > 2.8$ GeV cut was applied with a coarse SHC calibration, the first cut serves to tighten it when the more accurate SHC calibration is applied. For the 50 and 52 GeV data, however, only a looser cut of $E_{SHC} > 3.0$ GeV is applied, because the accurate calibration had already been used in the first stage selection. The second cut rejects almost all beam-wall and beam-gas events (for these, the total energy cannot exceed the beam energy) and most of the $\tau^+\tau^-$ and two-photon events. Radiative Bhabha events and $\tau^+\tau^-$ events, which only rarely have a charged multiplicity higher than four, are effectively eliminated by the third cut. The fourth cut ensures that there is no large energy leakage into the beam direction and further removes two-photon events.

In Fig. 3.2 we show the distributions of these cut variables (both for the experimental data and our estimates based on the MC simulation). It can be seen from the figure that our selection of cut values eliminates the background processes with minimal effect on the hadronic events of interest. An assessment of the effect of these cuts on our measurements will be given in the next section.

All of the events that satisfy the hadronic event cuts were visually scanned by physicists. The purpose of the scan is to reject obvious radiative Bhabha events, cosmic-ray initiated events, and beam-wall/gas events.

In the scan we found and rejected ten low-multiplicity events (of which eight have $N_{chg} = 5$ and two have $N_{chg} = 6$), where each track that enters the SHC causes a shower, as radiative Bhabha scattering events. An example of such events is shown in Fig. 3.3. In order to check the unambiguity of the visual scan for rejecting Bhabha events, the hadronic event cuts with a looser $N_{chg} \geq 4$ cut are applied to the basic hadronic sample, and the events that pass the cuts are all scanned and those identified as Bhabha events are kept. The MC simulations of the Bhabha process are also processed through the same loose hadronic event cuts. We find 5.7 ± 1.0 events/pb^{-1} for real data and 6.0 ± 1.2 events/pb^{-1} for MC data. (The quoted errors are statistical.) They agree within the statistical errors and confirm the unambiguity of the visual scan.

Also, twelve events were rejected as cosmic-ray induced events. These are obvious; an example is shown in Fig. 3.4.

In the scan we found sixteen beam-gas/wall events that had passed the hadronic event cuts because they contain either a large fake neutral energy due to electronic noise signals in the SHC or a wrongly reconstructed high momentum CDC track. Electronic noise in the SHC occurred during part of our data taking run when an incorrect high voltage value was applied to one section. A spurious high momentum CDC track is falsely reconstructed when a low momentum track curls around and leaves many hits in the CDC. A typical beam-wall/gas event where this occurs is shown in Fig. 3.5. There it can be seen that these events are also quite distinct and easily recognizable.

Independent scans were made by two physicists and the results were compared to estimate any possible scanner-dependence on the result. No such dependence was observed. In any event, the number of events rejected by the scan is small ($\simeq 1.6\%$), indicating that the visual scanning procedure is not a serious potential source of bias. However, a rather conservative value of 10% is assigned as a systematic error associated with the visual scan, corresponding to a 0.2 % error in the R calculation.

While we can conclude that the contamination from Bhabha scattering, cosmic ray initiated events, and beam-wall events is negligible after the scan, contamination from beam-gas events, which may not be clearly distinguishable from hadronic events, were further estimated, as is described in the next section.

The total number of hadronic events finally obtained was 2280, as summa-

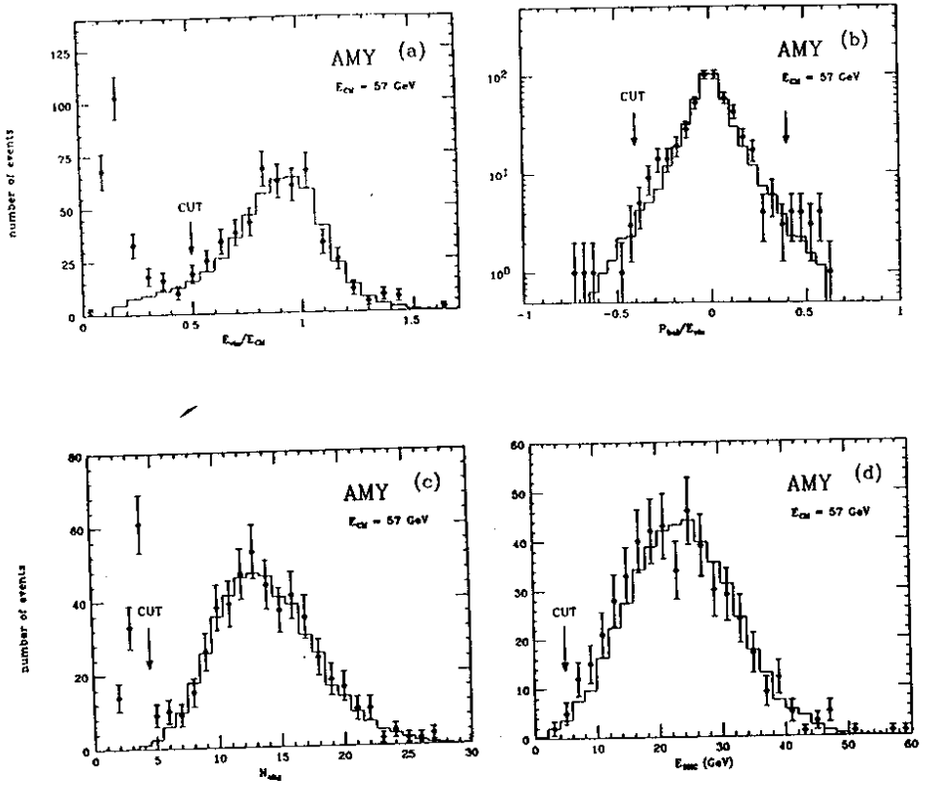

Figure 3.2: Distributions of the event cut variables. (a) E_{vis} distributions of the actual data after all the hadronic event cuts except the E_{vis} cut are applied (points). Also shown are the results of the MC simulation for hadronic events (histgrams). Corresponding distributions are given for: (b) P_{bal}/E_{vis}; (c) N_{chg}; and (d) E_{SHC}.

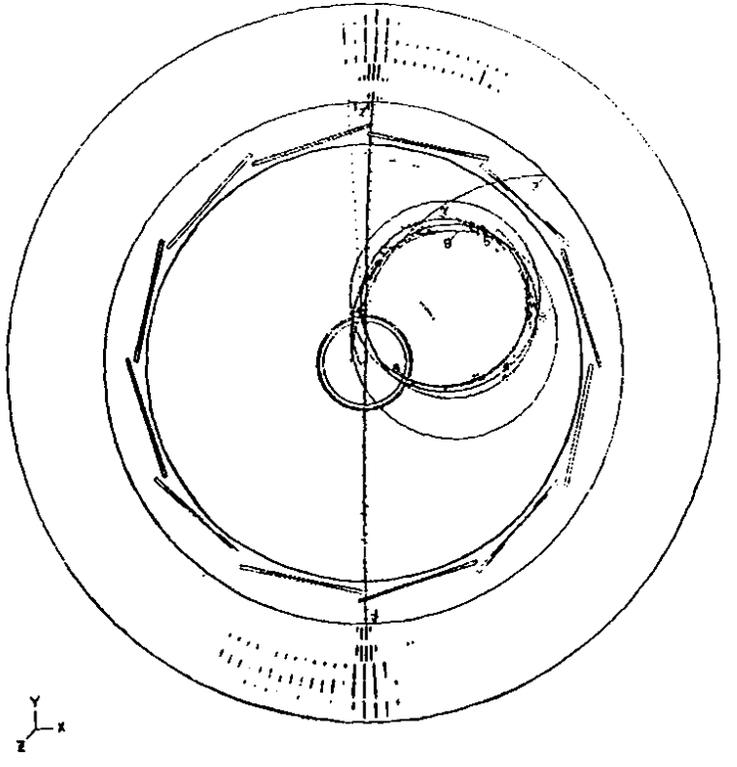

Figure 3.3: A radiative Bhabha event rejected by the visual scan.

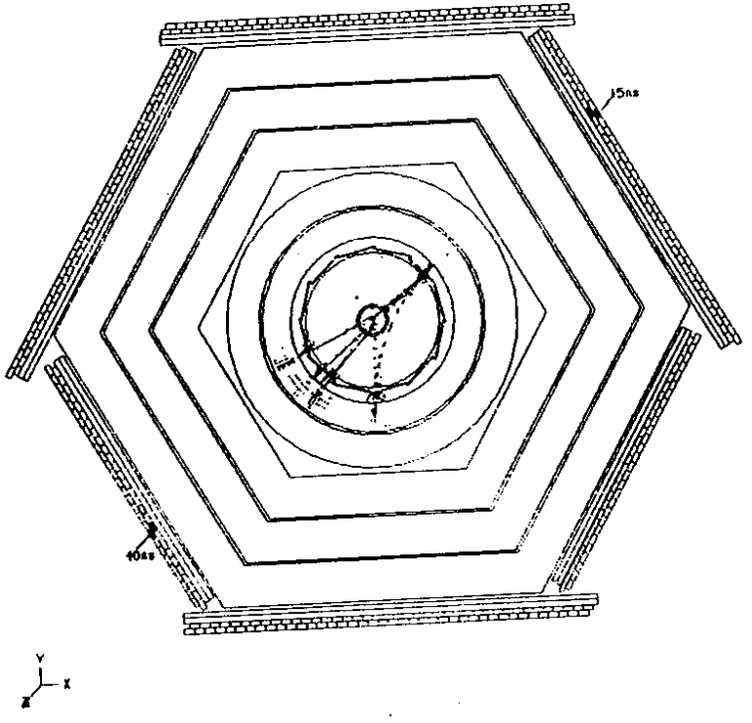

Figure 3.4: A cosmic ray induced event that was rejected by the visual scan.

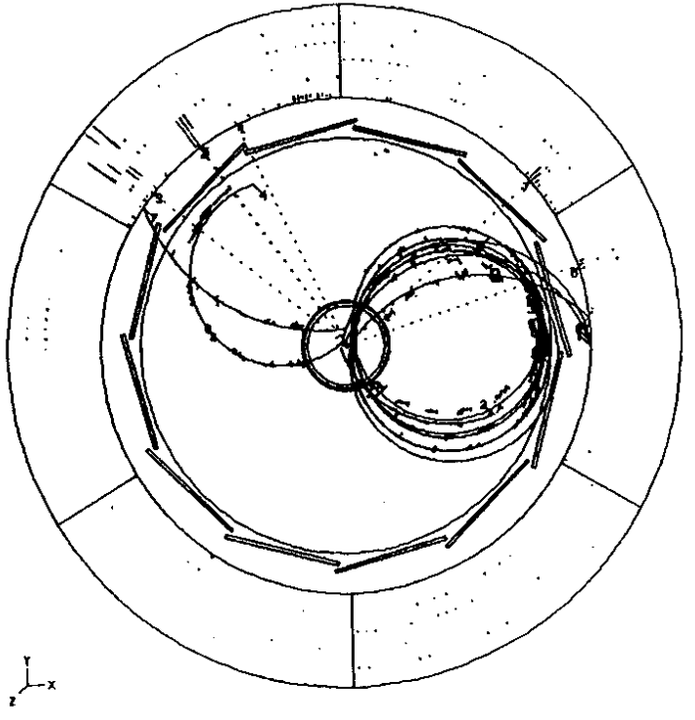

Figure 3.5: A beam-wall event rejected by the visual scan. Large SHC noise signals are seen.

$\sqrt{s}$ (GeV)	raw data	1st filter	2nd filter	had.ev.cuts	visual scan
50	1197857	572154	911	91	88
52	1637857	839054	4027	490	482
55	1926857	1126649	2458	376	368
56	2452022	1553682	5300	735	727
56.5	617819	405324	1343	131	123
57	1291053	865023	3902	495	492

Table 3.3: Number of events in each selection step.

$\sqrt{s}$ (GeV)	50	52	55	56	56.5	57
N_{obs}	88	482	368	727	123	492
N_{bkg}						
$-\tau\tau$	$0.86 \pm .11$	$5.4 \pm .7$	$3.7 \pm .5$	$6.8 \pm .9$	$0.72 \pm .10$	$3.2 \pm .5$
-2γ	$0.49 \pm .12$	$3.1 \pm .7$	$2.5 \pm .6$	4.6 ± 1.1	$0.77 \pm .18$	$3.4 \pm .8$
$\int Ldt$ (pb^{-1})	$0.64 \pm .02$	$3.98 \pm .04$	$3.27 \pm .04$	$5.99 \pm .05$	$0.99 \pm .02$	$4.40 \pm .05$
$(1+\delta)$	1.336	1.330	1.318	1.313	1.310	1.307
ϵ	0.652	0.650	0.633	0.632	0.645	0.645
$\epsilon(1+\delta)$	0.871	0.865	0.834	0.830	0.845	0.843
$\sigma_{\mu\mu}$ (pb)	34.7	32.1	28.7	27.7	27.2	26.7
R	$4.50 \pm .48$	$4.29 \pm .20$	$4.62 \pm .24$	$5.19 \pm .19$	$5.32 \pm .48$	$4.90 \pm .22$
R (theory)	4.22	4.32	4.54	4.63	4.68	4.73
R(with top)	5.68	5.80	6.05	6.16	6.22	6.28

Table 3.4: Summary of calculation of R; Only the statistical errors are shown here. Theoretical values are calculated with $M_{Z^0} = 92.0$ GeV/c^2, $\sin^2\theta_W = 0.230$, and $\Lambda_{\overline{MS}}$=0.2 GeV with $O(\alpha_S^3)$ QCD (t quarks are assumed to be fully excited).

rized in Table 3.3. Note that a small number of background events from τ pair production and two-photon hadronic events were still contained in this sample. These were statistically subtracted using a procedure that is described in the next section.

3.4 Total Hadronic Cross Section

The total hadronic cross section is calculated by correcting the number of hadronic events, obtained in the previous section, for background contamination and detector acceptance, and then normalizing to the integrated luminosity. In order to facilitate comparisons with theoretical predictions (Eq. 1.9) that do not include electroweak radiative corrections (but do include QCD corrections), the total cross section is also corrected for electroweak radiative effects.

By expressing the cross section in units of the lowest-order QED mu-pair production cross section, we obtain the quantity R, already introduced in Chapter 1, as:

$$R = \frac{N_{obs} - N_{bkg}}{\epsilon(1+\delta)\int Ldt \cdot \sigma_0}, \tag{3.30}$$

where N_{obs} is number of the observed hadronic events; N_{bkg} is the estimated number of the background events; ϵ is the detector's acceptance for hadronic events; $(1+\delta)$ is the radiative correction factor; $\int Ldt$ is the integrated luminosity; and σ_0 is the lowest-order QED cross section for $e^+e^- \to \mu^+\mu^-$, $\sigma_0 = 4\pi\alpha^2/3s \simeq 86.85/s$ (nb), where s is the center-of-mass energy squared in units of GeV^2.

The integrated luminosities have been already discussed in section 3.2, and are listed in Table 3.4. In the following, we describe in detail how we obtain each of the other factors and estimates for their systematic errors.

3.4.1 Background Fraction

Potential background sources have been enumerated in the previous section. Here we describe our estimates of the contribution from each of these sources.

Since it is very difficult to distinguish unambiguously the $\tau^+\tau^-$ events and two-photon hadronic events from multi-hadronic annihilation events, we use MC simulations of these processes to estimate how many of them are misidentified as hadronic events. It is found that the MC calculation underestimates the low energy peak in the E_{vis} distribution, a discrepancy that we attribute to an ambiguity in normalization of the VDM component of two-photon events. This corresponds to about a factor of two increase of the VDM component; we assign this as a systematic error that contributes a 0.13 % error to the R measurement. The estimated number of background events from $\tau^+\tau^-$ and two-photon hadronic events is summarized in Table 3.4.

Beam-gas collision events that might pass the visual scan can occur anywhere up- or down-stream of the interaction point. We estimated possible contamination from these events by redoing the first stage filtering on a sample of the data with the vertex condition for "good" charged tracks changed from the usual $|Z_0| < 10$ cm to 15 cm $< |Z_0| < 30$ cm, and then seeing how many events pass the hadronic event cuts. In a data sample corresponding to an integrated luminosity of 6.0 pb^{-1} we find no events that pass this "off-vertex" selection. This gives a 95 % confidence level upper limit on the fraction of background contamination from these events of 0.3 %. We include this number in the systematic errors.

3.4.2 Detector Acceptance

For the purpose of determining the detector's acceptance, we applied the hadronic event cuts to MC simulated hadronic events that were generated with the effects of initial-state radiation included. The resulting distributions for the charged particle momenta and the neutral particle energies agree quite well with those of the real data as can be seen in Figs. 2.10.

The detector acceptance, ϵ, is the number of the MC events that have passed the hadronic event cuts divided by the total number that were generated. This is found to be approximately 64 % and almost independent of the center-of-mass energy (see Table 3.4).

In order to study the relation between ϵ and the particular choice of hadronic event cut values, we determine ϵ for a variety of cut values (see Fig. 3.2). Changes in R for different cut values are shown in Fig. 3.6; these are small ($< 1\%$), even for quite large variations of the cut values. We calculated the shift in R that results from varying each cut value by an amount corresponding to our resolution in that variable. This was used as an estimate of the systematic error due to our choice of cut value. The variations used are indicated in Fig. 3.6. Combining the results for each cut parameter in quadrature gives a systematic error on the acceptance of $\pm 1.5\%$.

The above-mentioned calculation of ϵ relies heavily on the MC simulations, which, in turn, are based on theoretically motivated event generators as was discussed in Chapter 2. Thus, ambiguities in the fragmentation and event generation schemes may result in errors in our determination of ϵ. We estimated the dependence on the event generation schemes by comparing the results of Lund 6.2 (the matrix-element method plus string fragmentation) and Lund 6.3 (the parton-shower method plus string fragmentation), both of which give a rather good description of the real data. We find that $\Delta\epsilon/\epsilon \simeq 0.7\%$, which we use as a systematic error. We estimated the dependence on the choice of fragmentation-scheme by comparing results using string fragmentation (SF) and independent fragmentation (IF). We use Lund 6.2 (with SF option), Lund 6.2 (IF), EPOCS (SF), and EPOCS (IF). We find a variation of $\Delta\epsilon/\epsilon \simeq \pm 0.9\%$, which we also include as a systematic error.

An additional potential source of systematic error in ϵ can be differences between the detector simulation and the actual detector responses. For the simulation of the CDC, we compare the results of the two different simulations: one is a simple one that assumes a constant spatial resolution over the whole detector region; the other is a more detailed version that is carefully tuned to fit the various distributions of the real data. Although the simple version results in a slight shift in the charged multiplicity distribution, the difference in ϵ derived from the two simulations is found to be negligible.

For the SHC, we vary the calibration constants over a range such that the electron energies measured by the SHC are still consistent with the momentum as measured by the CDC. This results in a 0.8% changes in the number of selected hadronic events, which we use as the systematic error due to the ambiguities in the SHC calibration.

We also searched for possible failures of our online data taking system for recording hadronic and Bhabha events. Because the measurement of the total cross section for hadronic events is essentially the number of hadronic events divided by the number of Bhabha events, any systematic difference between hadronic and Bhabha event handling would result in an error in the total cross section. Occasionally, for certain short periods of time ($\sim$ a few seconds) elec-

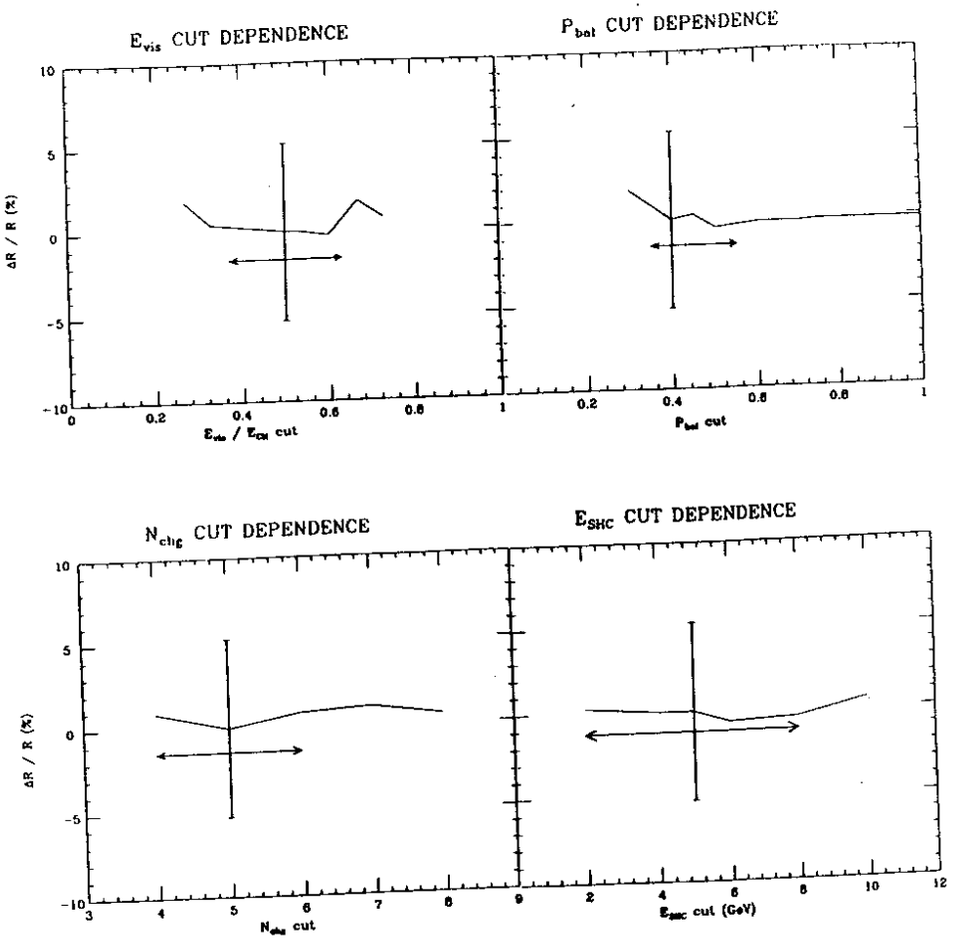

Figure 3.6: Changes in R due to different hadronic event cut values. The size of the variation of the cut value that we used to estimate the systematic error is shown. Typical statistical errors are also shown.

tronic noise corrupted the CDC data records. Also, severe background radiation conditions sometimes caused the high voltage supplies for the CDC to trip, creating dead time of the CDC. Since the luminosity determination relies on Bhabha events in the PTC (see the next section), which are independent of the CDC data, the number of observed hadronic events must be corrected for these effects. We estimate the correction factor by counting the number of Bhabha events detected by the SHC that have no CDC data because of the above-mentioned effects. (The good position resolution of the SHC enables us unambiguously to discriminate Bhabha events from $e^+e^- \to \gamma\gamma$ without help of the CDC by measuring the bending of electrons' and positrons' trajectories in the magnetic field.) We find these effects to be small, approximately 0.3%. We include this correction factor in the estimate of the detector acceptance. The error of this correction factor is included in the systematic error of the acceptance.

Finally, by combining all of these results in quadrature, we find an overall systematic error on ϵ that is 2.0%.

3.4.3 Radiative Corrections

The Lund 6.3 generator, which is used as our standard hadronic event generator to estimate the detector acceptance, incorporates the BKJ radiative corrections [62], which only include the dominant terms (section 2.3.1). We therefore use the FKS calculations [63] to obtain the correction factor for full electroweak radiative effects, $(1+\delta)$. Possible sources of systematic errors in $(1+\delta)$ are investigated here.

Hard initial state photon emission accounts for the biggest contribution to the correction factor, $(1+\delta)$. This is because the large loss of the energy in the initial state results in an e^+e^- system with a lower energy where the annihilation cross section is higher. The cross section for the initial-state hard photon emission is

$$\frac{d\sigma}{dk} = \frac{\alpha}{\pi}\left(\ln\frac{s}{m_e^2} - 1\right)\left(1 + \left(\frac{s'}{s}\right)^2\right)\frac{1}{k}\sigma_h(s'), \tag{3.31}$$

where $s' \simeq (1-k)s$ is the center-of-mass energy squared after the hard photon emission and $\sigma_h(s')$ is the total hadronic cross section at $\sqrt{s'}$. This is divergent both for $k \equiv E_\gamma/E_{beam} \to 1$, and for $k \to 0$. The latter divergence, infrared divergence, is treated in a self-consistent way by setting a lower cut-off, k_{min}, and calculating the correction for $k < k_{min}$ as part of the corrections for vertex and vacuum polarization. The actual value of k_{min} that is chosen does not matter as long as it is small enough so that it does not affect ϵ, but large enough to keep the correction for the hard photon emission smaller than unity.

The $k \to 1$ pole occurs because there the effective e^+e^- center-of-mass energy approaches zero where the annihilation cross section diverges as $1/s$. Because hadronic annihilation, by definition, must have at least two pions in the final state, the maximum value of k is $(1-4m_\pi^2/s)$ where m_π is the pion mass. Because of the large uncertainties in σ_h at lower energies, a reliable calculation for $k \sim 1$ cannot be made. However, when k gets close to 1, the center-of-mass energy of the e^+e^- system is not high enough to produce a hadronic final state that can pass our hadronic event cuts ($E_{vis}/\sqrt{s} > 0.5, N_{chg} \geq 5$ etc.). We introduce a higher cut-off, k_{max}, and ignore those events with $k > k_{max}$. We have chosen $k_{max} = 0.99$. This introduces a dependence of $\epsilon(1+\delta)$ on k_{max} that is estimated in two ways. First, we calculate $\epsilon(1+\delta)$ with different values of k_{max}; the value of $\epsilon(1+\delta)$ decreases by 0.8% (1.2%) when we change k_{max} from 0.99 to 0.90 (0.80). Secondly, we estimate how much $\epsilon(1+\delta)$ can change if we raise k_{max} up to the maximum value $(1-m_\pi^2/s)$. Because we can write

$$\epsilon(1+\delta) = \epsilon_{k<k_{min}}(1+\delta_{k<k_{min}}) + \int_{k_{min}}^{k_{max}} dk\epsilon_k\delta_k, \tag{3.32}$$

we just need to estimate

$$\Delta\epsilon(1+\delta) = \int_{0.99}^{1-4m_\pi^2/s} dk\epsilon_k\delta_k. \tag{3.33}$$

Here ϵ_l and δ_l are the acceptance and the radiative correction factor at $k = l$. By noting that acceptance for $k > 0.99$ should be smaller than that for $0.9 < k < 0.99$, that is $\epsilon_k = 5.4 \pm 0.8$ %, and by using the quark-parton model cross section to estimate δ_k from Eq. 3.31, we obtain the inequality (the error is statistical)

$$|\Delta\epsilon(1+\delta)| < 0.0081 \pm 0.0012. \tag{3.34}$$

Hence, the change in $\epsilon(1+\delta)$ is at most 1 %. From these two different methods, we take the systematic error associated with k_{max} to be 1.0%.

The theoretical calculation used for the radiative corrections also has a few uncertainties. These include the ambiguity existing in the calculation of the hadronic vacuum polarization and the effects of higher order corrections that have not been considered.

The correction factor for the hadronic vacuum polarization is calculated as a dispersion integral over the total hadronic cross section [76],

$$\delta_{had.vac} = -\frac{s}{2\pi^2\alpha}\int_{4m_\pi^2}^{\infty} d\zeta\frac{\sigma_h(\zeta)}{\zeta - s}. \tag{3.35}$$

Here σ_h is the total hadronic cross section which is only known to a precision of 10–15% at lower energies [77]. The FKS calculation uses a quark-parton model cross section for σ_h, while the BKJ calculation in Lund 6.3 incorporates a simple formula that is based on the numerical interpolations of the experimental hadronic cross section [80]. Although these two calculations agree to within 0.2%, the FKS values deviate by as much as 0.5% from the Lund 6.3 result when the light quark masses are varied over a reasonable range of values. Shimizu has also calculated $\delta_{had.vac}$ by numerically integrating experimental cross sections [79]. The systematic error of this calculation is estimated by comparing these different calculations and also by varying the hadronic cross section in the dispersion integral by ±15 %, and is found to be 1.0%.

It has been claimed by several experimental groups [20,22,29] that the higher order radiative corrections can be as high as a few percent. Tsai [81] estimated the higher order QED corrections by summing all leading logarithms and obtained a correction factor at the one-percent level. However, his calculations are not complete and the errors of the calculations are large. In contrast, recently reported exact calculations by Berends et al. [82] indicate that the correction factor is smaller than 1%, as claimed by Marshall [83] (however, it becomes significant for higher energies). Therefore we ignore the higher order radiative corrections here.

Summing up all the above errors in quadrature gives a total systematic error associated with radiative corrections of 1.3%.

3.5 Result and Discussion

The results on the calculation of the R values, discussed in the previous sections, are summarized in Table 3.4. In the table, only the statistical errors are listed. Although we assume particular values of the standard model parameters (M_{Z^0}, m_t, $\sin^2\theta_W$, etc) to calculate radiative corrections and detector acceptance, the obtained values of R are not sensitive to the values used.

The point-to-point systematic errors vary from 1.1% to 2.8% for different center-of-mass energies, as shown in Table 3.5, and the overall normalization error is 4.1%. These results are also shown in Fig. 3.7 together with PEP/PETRA results (averaged) and theoretical predictions. The error bars indicated are the quadratic sums of statistical and systematic errors.

Although the 4.1% normalization error is reasonably small compared to the previous measurements of R by other experiments, possible ways to reduce this number are considered in the following.

The largest contribution to the normalization error comes from the alignment error of the PTC in the luminosity measurement (3.0%). This will certainly be improved as we continue to study the Bhabha events and better understand the systematics. The good agreement between the luminosity measured by the PTC and that measured by the SHC suggests that the systematic error can be reduced below the current 3.0%. If more luminosity is accumulated in the future, the Barrel SHC will be used for the luminosity measurement, reducing this error. Currently, new endcap detectors are being prepared to replace the PTC. One of the purposes of the new detectors is to minimize the systematic errors of the luminosity measurement by providing improved measurements of positions and energies in the endcap region.

The second largest error comes from the dependence on the event selection cuts (1.5%). This indicates that there are still some conceivable differences between our event simulations and the experimental data. Because we have not tried very hard to tune the fragmentation parameters of the MC simulations to realize a best matching with the real data, we expect that efforts in this direction will reduce the error to at least less than 1 %, as has been realized by other

systematic errors	(%)
(luminosity)	
statistics	2.5, 1.1, 1.2, 0.9, 2.2, 1.1
rad. correction, acceptance	1.3
background	0.2
position measurement	0.0, 1.7, 0.0, 0.0, 0.0, 0.0
trigger efficiencies	0.2
chamber efficiencies	0.1
alignment	3.0
(radiative corrections)	
k_{max} dependence	1.0
had. vac. polarization	0.8
(detector acceptance)	
MC statistics	0.8, 0.8, 0.6, 0.6, 0.7, 0.7
MC scheme	0.7
fragmentation	0.9
data recording failure	$^{+0.94}_{-0.00}$, 0.13, 0.17, 0.15, 0.90, 0.34
event selection cuts	1.5
calibration/reconstruction	0.8
(background)	
$\tau\tau$, two-photon	0.2
beam-gas	0.3
visual scan	0.2
point-to-point error	2.8, 2.2, 1.4, 1.1, 2.5, 1.3
overall normalization error	4.1

Table 3.5: Summary of systematic errors of R: Where six numbers are shown, each corresponds to 50, 52, 55, 56, 56.5, and 57 GeV data, respectively.

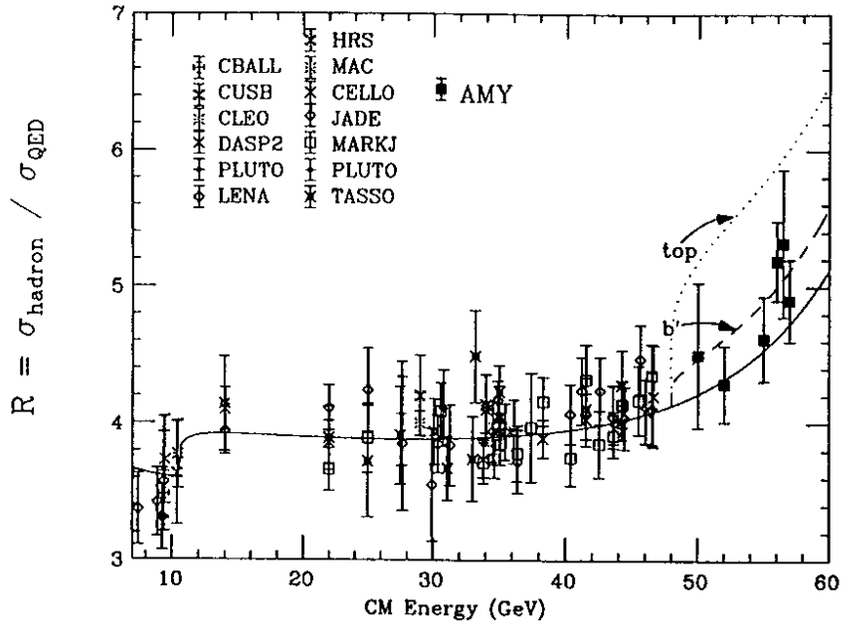

Figure 3.7: The R values from this experiment together with those from other experiments. The full line is the theoretical prediction with 5 quark flavors; the dotted (dashed) line indicates the prediction for t (b') quark production for $m_t(m_{b'}) = 24$ GeV/c^2.

experiments.

The ambiguities in the calculations of the radiative corrections are another source of large errors. In the analysis of hadronic contributions to the electroweak parameter renormalizations, Jegerlehner [77] and Cole et al. [78] independently estimated the uncertainty in $\delta_{had.vac.}$ at $\sqrt{s} = M_W$ to be roughly 3–6% by using the experimental hadronic cross sections; this corresponds to an error of 0.2–0.3% in R. This value may be rather optimistic, but a similar analysis at our energies should yield an error that is smaller than the current 0.8%.

Furthermore, we may have overestimated the systematic errors due to the fragmentation scheme dependence (0.9%) and the MC scheme dependence (0.7%), because descriptions of the real data by some of the MC simulations we used are not excellent. If all the MC simulations used for the evaluation of the MC dependence are tuned to their best, the systematic errors may decrease considerably.

To summarize, it is not unreasonable to hope that with further efforts we will be able to reduce the systematic normalization error down to about the 2% level.

Chapter 4

New Heavy Quarks

In this chapter, we examine the possibility that new heavy quarks (t or b' quarks) may be pair-created in our energy region. First, the obtained R values are compared to the theoretical predictions with and without new heavy quark production. Second, event shape variables are calculated for each hadronic event; an excess in number of spherical events would be a signal for the new heavy quark production.

4.1 Examination of R-values

In Fig. 3.7, we have included the expectations for R in the event of new heavy quark production (here, masses of new quarks are assumed to be 24 GeV/c^2). In the case of b' quark production, we cannot draw any conclusion from the R measurements alone, because the expected increase in R ($\Delta R \sim 11\%$ for full excitation) is small and is overshadowed by the measurement errors ($\geq 6\%$) and by the ambiguities in the standard model parameters ($\sim$ 2.0–2.5% in R for our energy region). We therefore only discuss the possibility of t quark production; this is expected to increase R by as much as 33%.

Fig. 3.7 shows that our R values are consistent with the predictions with known 5 flavors, although the higher energy points are systematically slightly higher. In Table 3.4, the obtained R values are compared with the expectations with and without the t quark production. Here, fully excited t quark production is assumed (i.e., $\beta \sim 1$). At the highest energy (57 GeV), where we are most sensitive to the t production, an upper limit for the possible increase in R,

$$\Delta R < 0.76^{+0.10}_{-0.15} \qquad (95\%\text{C.L.}), \tag{4.36}$$

is obtained. Here the error represents ambiguities in the theoretical calculation due to the experimental errors in M_{Z^0}, $\sin^2\theta_W$, and $\Lambda_{\overline{MS}}$ ($M_{Z^0} = 91.9 \pm 1.8\text{GeV}/c^2$, $\sin^2\theta_W = 0.230 \pm 0.0048$, and $\Lambda_{\overline{MS}} = 0.15 - 0.30$ GeV; it is dominated by the M_{Z^0} error) [15,10]. This upper limit corresponds to $49^{+6}_{-10}\%$ of the fully excited t production.

Thus, we can conclude that our R values are consistent with the prediction with known 5 flavors and that fully excited t production is excluded with 95% confidence level for our energy region.

4.2 Event Shape Analysis

We show distributions of thrust and acoplanarity for each energy in the Figs. 4.1 and 4.2. The predictions of the Lund 6.3 Monte Carlo, both with and without t quarks, are also indicated in the figures. Here we assume that the t quark mass is 1 GeV/c^2 less than the beam energy (so the quark velocity is $\beta \simeq 0.26$) and the threshold behavior of the $t\bar{t}$ production is that given by the quark-parton model, $R_{t\bar{t}} = \frac{3}{4}Q_t^2\beta(3-\beta^2)$, which ranges between 0.51 and 0.54, depending on the c.m. energy.

This value of $R_{t\bar{t}}$ is probably conservative, because neither the QCD correction nor the weak correction is taken into consideration. (Compare these figures with those given in Chapter 1, where all the corrections are taken into account.) The QCD correction would raise $R_{t\bar{t}}$ by more than 5%, while the weak correction does not significantly change it (by less than 1%) for the top quark with $\beta \simeq 0.26$. $R_{b'\bar{b}'}$ is similarly calculated and is 0.13–0.14, where the QCD correction would raise this by more than 5% and the weak correction by 15%.

The figures indicate that the data are consistent with the MC prediction without new heavy quarks, and the expected excess in number of spherical events is not seen. In order to quantify this result, we calculate upper limits on the cross section for new heavy quarks in the following.

We select spherical events by making cuts in the distribution of acoplanarity A. The R values for new heavy quark (Q) production, $R_{Q\bar{Q}}$, are obtained from the experiment as

$$\begin{aligned} R_{Q\bar{Q}} &= \frac{\sigma_{Q\bar{Q}}}{\sigma_0} \\ &= \frac{N^{obs}_{Q\bar{Q}} - N^{bkg}_{Q\bar{Q}}}{\epsilon_{Q\bar{Q}}(1+\delta_{Q\bar{Q}})\int Ldt \cdot \sigma_0}. \end{aligned} \tag{4.37}$$

Here $N^{obs}_{Q\bar{Q}}$ is the observed number of spherical events, i.e., the number of events satisfying the condition of high A (Q represents t or b'); $N^{bkg}_{Q\bar{Q}}$ is the number of background events estimated to originate from light quark production and other sources; $\epsilon_{Q\bar{Q}}$ is the detector acceptance for the spherical heavy quark events; and $(1+\delta_{Q\bar{Q}})$ is the radiative correction factor for the heavy quark production. The expected value of $R_{Q\bar{Q}}$ for fully excited t (b') production is ~ 1.5 (~ 0.5), slightly depending on the center-of-mass energy.

The detector acceptance is calculated using the Lund 6.3 MC program for several different heavy quark masses and is found to be slightly higher for smaller values of the assumed quark mass. This seemingly strange result can be understood in the following way. According to the standard V-A theory, the matrix element for the t decay, $t \to bq'\bar{q}$, becomes

$$|M|^2 \sim 2m_t E_{q'} E_{\bar{q}} E_b \sin^2\frac{\theta_{\bar{q}b}}{2}, \tag{4.38}$$

where $E_{q'}$, $E_{\bar{q}}$, and E_b are the energies of the final state quarks, and $\theta_{\bar{q}b}$ is the angle between the b and the $\bar{q}$ quarks in the rest frame of t. Therefore, the decay

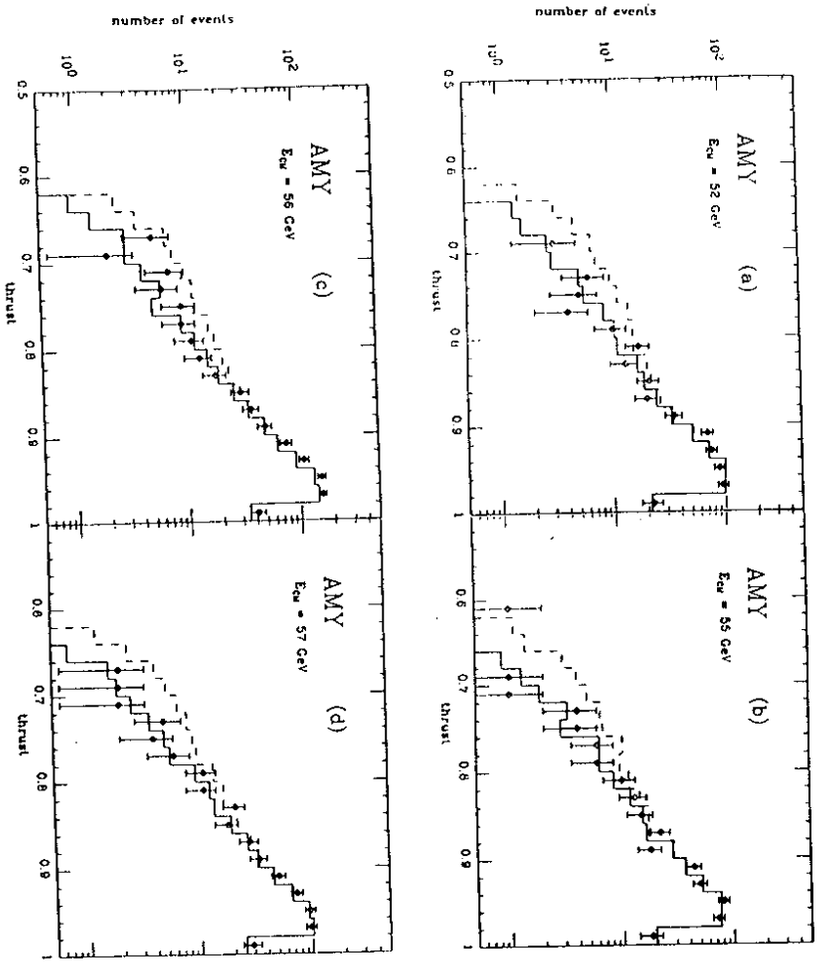

Figure 4.1: Thrust distributions for (a) 52 GeV, (b) 55 GeV, (c) 56 GeV, and (d) 57 GeV data (points). Also shown are the results of the MC simulation with and without t quark production (histgrams). Here, t quark mass is assumed to be 1 GeV/c^2 less than the beam energy and the threshold behavior of $R_{t\bar{t}} = \frac{3}{2}Q_t^2\beta(3-\beta^2)$ is used.

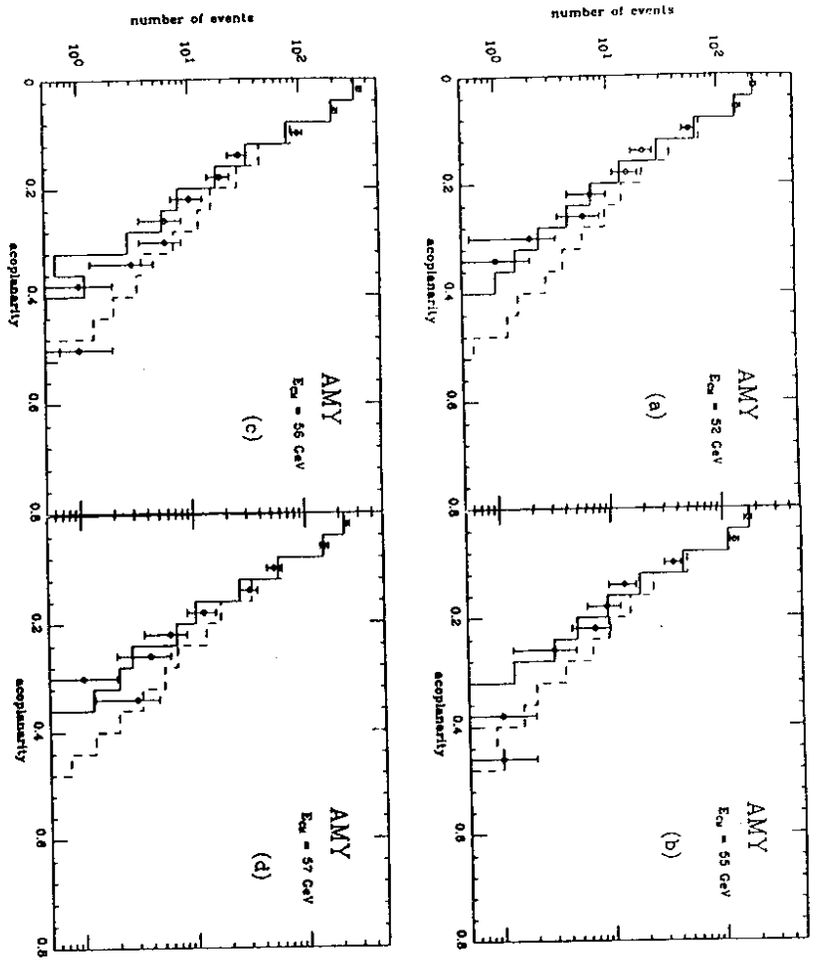

Figure 4.2: Acoplanarity distributions for (a) 52 GeV, (b) 55 GeV, (c) 56 GeV, and (d) 57 GeV data (points). Also shown are the results of the MC simulation with and without t quark production (histgrams). Here, t quark mass is assumed to be 1 GeV/c^2 less than the beam energy and the threshold behavior of $R_{t\bar{t}} = \frac{3}{2}Q_t^2\beta(3-\beta^2)$ is used.

products are likely to form back-to-back jets. When the two decaying t quarks are at rest, the event tends to form a plane, thus giving a low A value. When the t quarks are moving, the Lorentz boost helps to make the event more spherical.

The radiative correction factor is obtained from the FKS calculations [63], which properly incorporate the (assumed) heavy quark mass in the full electroweak calculation. The result of the calculation can be conveniently formulated as $\delta_{Q\bar{Q}} \simeq -\exp(-4.133\beta - 0.689)$, where β is the heavy quark velocity. (For example, $(1+\delta_{Q\bar{Q}}) \simeq 0.86$ for $m_Q = E_{\rm beam} - 1$ GeV/c^2, i.e., $\beta \simeq 0.26$.)

Backgrounds from τ-pair production events are negligible, because those events are mostly jet-like, high thrust events. Some events from two-photon hadronic events, especially VDM events, sometimes appear quite spherical, but the expected number of events is very small, roughly of the order of 0.01 events for the whole data sample (slightly depending on the cut values). Thus, two-photon backgrounds are also ignored.

The systematic errors for $R_{Q\bar{Q}}$ are estimated in a similar way as those for the determination of R; the errors from the luminosity measurements are also the same. For radiative corrections, there is no ambiguity in k_{max}, since it is naturally cut off by the heavy t mass; the other errors associated with these corrections are the same as for the case of R.

For detector acceptance, in addition to the systematic errors considered in the case of the R value measurements, we have to include the dependence on the event shape cuts (cuts on A). Here, the dependence on the MC models is not strong; for example Lund 6.2 with matrix element gives 3.3% smaller value of $\epsilon_{Q\bar{Q}}$ than our standard Lund 6.3 calculations for events with $A > 0.36$ for $m_t = 27.5$ GeV/c^2 and $\sqrt{s} = 57$ GeV.

The total systematic error for $R_{Q\bar{Q}}$, so obtained, is $\sim 7.5\%$, depending on the beam energy and the heavy quark mass.

The dependence of $R_{Q\bar{Q}}$ on the cut values used for A is shown in Fig. 4.3 for the 56 GeV data. Here $R_{Q\bar{Q}}$ remains almost constant for some region of the cut values, independently of whether or not the estimated background fraction from light quark events are subtracted. We use optimum value for the cut: $A > 0.36$, and do not subtract the light quark background (i.e., $N^{bkg}_{Q\bar{Q}} = 0$) in order to set conservative limits. For this cut value, $\epsilon_{Q\bar{Q}}$ is roughly 0.09 for $m_Q = E_{\rm beam} - 1$ GeV/c^2 ($\beta \simeq 0.26$).

We use the highest energy data alone, that taken at 57 GeV, to calculate upper limits on $R_{Q\bar{Q}}$. The obtained upper limits slightly depend on the value of the assumed heavy quark mass, and for $m_Q \leq 27.5$ GeV/c^2 they are $R_{t\bar{t}} < 0.358 \pm 0.027$ and $R_{b'\bar{b}'} < 0.325 \pm 0.024$ with 95% confidence level. Here the errors represent the total systematic errors involved in the calculation of $R_{Q\bar{Q}}$. These limits correspond to $23.1 \pm 1.7\%$ of the full excitation for the t production and $39.6 \pm 3.0\%$ of the full excitation for the b' production.

We can subsequently derive lower limits on new heavy masses by comparing these limits with the theoretical expectations. However, by including lower energy data (56.5 GeV, 56 GeV, etc) in the analysis, we can effectively increase

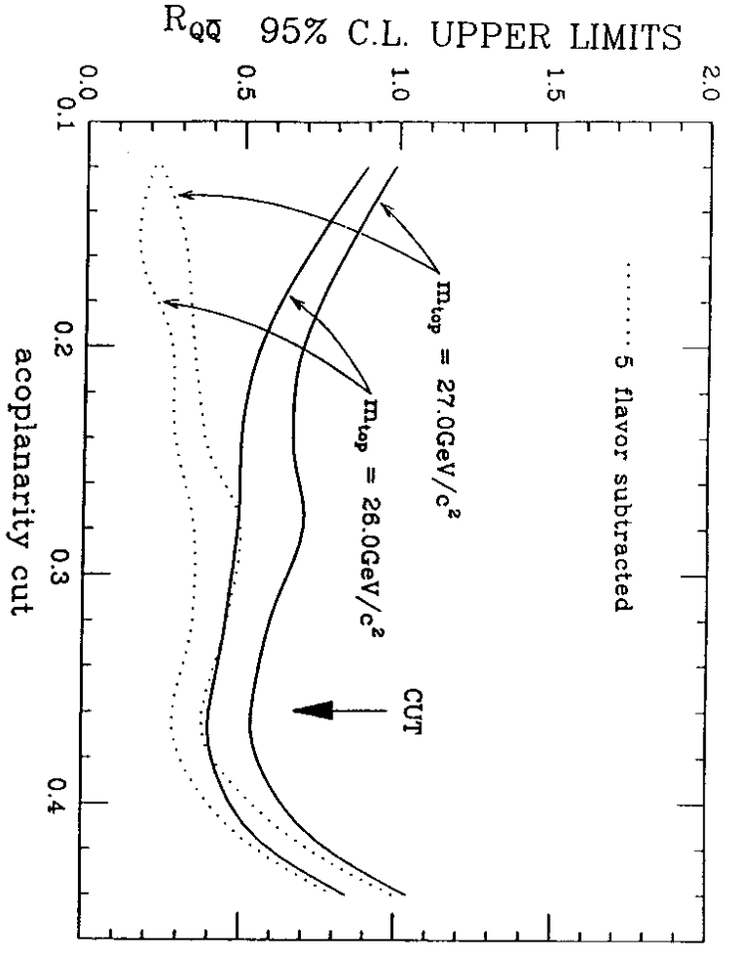

Figure 4.3: $R_{Q\bar{Q}}$ as a function of the cut value for A.

the total luminosity and thus are able to set a better limit on new quark masses, particularly for the case of b' quarks. Our method for doing this is described below.

In order to combine data from different energies, we work in terms of the number of heavy quark events, $N^{obs}_{Q\bar{Q}}$, instead of $R_{Q\bar{Q}}$, for the convenience of the analysis. The experimental upper limit on $N^{obs}_{Q\bar{Q}}$ is just an upper limit on the number of observed events with high A (we assume $N^{bkg}_{Q\bar{Q}} = 0$). The number of expected heavy quark events, $N^{theo}_{Q\bar{Q}}$, is calculated as

$$N^{theo}_{Q\bar{Q}} = \epsilon_{Q\bar{Q}}(1 + \delta_{Q\bar{Q}}) \int Ldt \cdot \sigma_0 \cdot R^{theo}_{Q\bar{Q}}. \tag{4.39}$$

Here, for $R^{theo}_{Q\bar{Q}}$, we use the values from the quark-parton model given above. $N^{theo}_{Q\bar{Q}}$ contains all of the systematic errors discussed earlier in this section.

We show the results in Fig. 4.4. The obtained mass limits are $m_t > 27.6$ GeV/c^2 and $m_{b'} > 25.5$ GeV/c^2 with 95% confidence level. These are rather conservative limits since we have ignored QCD and weak effects. For comparisons, we show in Fig. 4.5 the $N_{Q\bar{Q}}$ plot for high A event rates where we have included both QCD and weak effects. In this case the mass limits are much better, namely $m_t > 28.4$ GeV/c^2 and $m_{b'} > 26.8$ GeV/c^2 at the 95% confidence level. Note, however, these limits should be considered as the mass limits on the t (b') mesons.

To summarize, we found no evident rise in the R values in our energy region and no excess in the number of high-A events. By examining event shape distributions, upper limits for possible increase in R due to the new heavy quark production have been obtained. Sebsequently, we could set lower mass limits for new heavy quarks.

In fact, if we select the hadronic events by tagging high momentum leptons in the events, a more sensitive test on the heavy quark production (especially b' production) can be made, because high momentum leptons are most likely to originate from the weak decays of the heavy quarks. The result of this analysis will be reported elsewhere.

It is, however, important to note that because of its small cross section, possible pair-production of the b' quarks at our highest energies are not completely excluded.

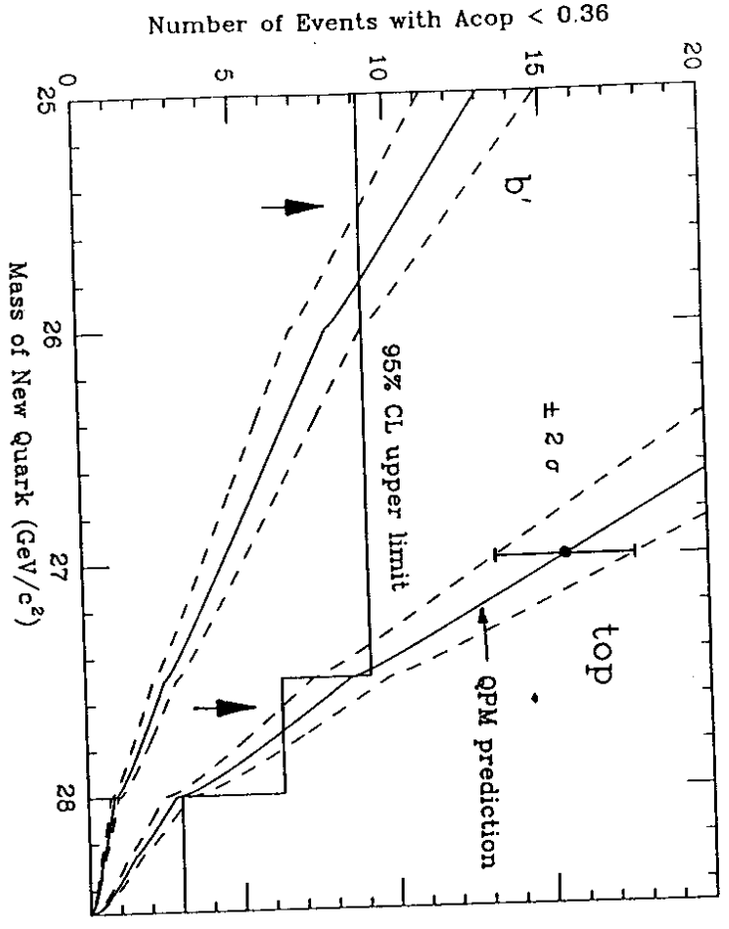

Figure 4.4: The 95% upper limits on number of heavy quark events are compared with the theoretical predictions using the quark-parton model threshold factor. The cut $A < 0.36$ is used to select heavy quark events.

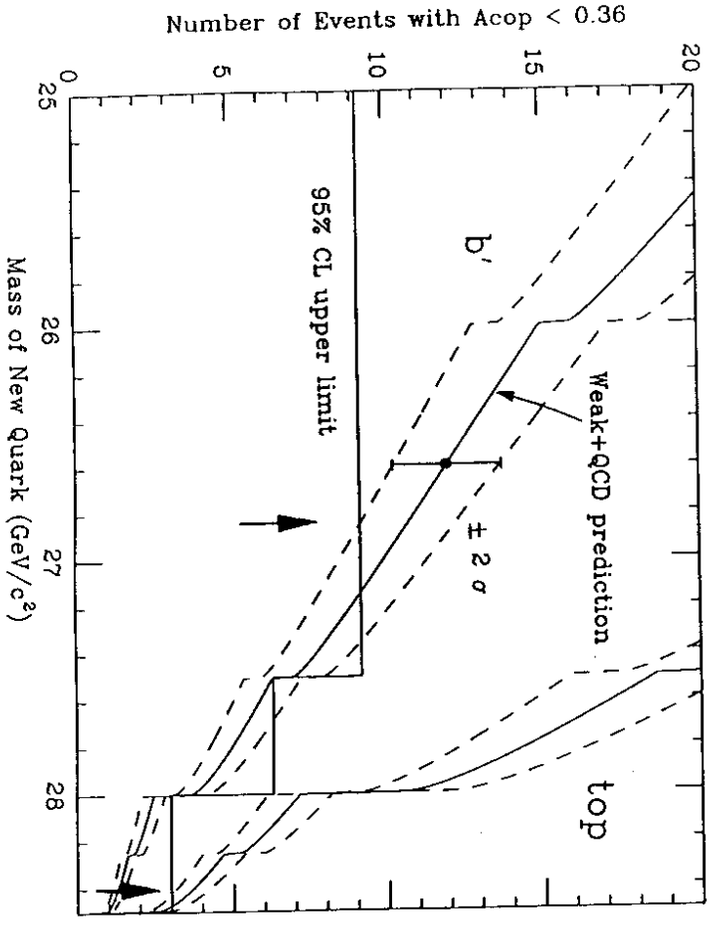

Figure 4.5: Same as Fig. 4.4. Here the QCD and the weak effects are included.

Chapter 5

Comparison of R-values to Standard Model

As was described in the previous chapter, we have found no evidence for new heavy quark production, and everything is fairly well described by the standard model with five known quark flavors. Here we will now turn to extracting the standard model parameters by fitting the measured R values to the standard model prediction (equation 1.9), assuming that only five known quark flavors are produced in our energy region. We follow the fitting method that was recently used by the CELLO group [20], which we will explain in the following.

First we split the error of R into three categories: the statistical error σ_{stat}, the systematic point-to-point error σ_{ptp}, and the common normalization error σ_{norm}. It is assumed that the quadratic sum of these three errors gives the total error of R. Then we define a $n \times n$ error matrix V_{ij} for n measurements of R in the following way. The diagonal element V_{ii} is just the square of the total error for the i-th measurement. The off-diagonal element V_{ij} represents the correlation between the i-th and j-th measurements. We assume that there is no correlation between different experiments; i.e., V_{ij} is set to be zero if the measurements i and j were made by different experiments. For the measurements by the same experiments, V_{ij} is estimated by the square of the common normalization error of the experiment, σ^2_{norm}. For experiments that give different normalization errors for different data running periods, the errors are split into a common normalization error for all the running periods (σ_{norm1}) and an additional normalization error for the individual periods concerned (σ_{norm2}); V_{ij} is estimated by σ^2_{norm1}.

Using a residual vector, $\Delta_i = R_i - R_{fit}$, the fitting procedure is to minimize χ^2 defined as

$$\chi^2 = \Delta^T V^{-1} \Delta. \tag{5.40}$$

We include the data of the PETRA [21], the PEP [22,23], the DORIS, and the CESR experiments [24], as edited and used by the CELLO group [20]; for these the BKJ (or equivalent) radiative corrections have been applied (see section 2.3.1). For those energies, the difference between the BKJ corrections and the FKS corrections (full electroweak corrections) is negligible and it is reasonable to compare their results to our R values, which are corrected using the FKS calculation. We also use a new precise measurement of R that was recently

Experiment	$\sqrt{s}$ (GeV)	R	σ_{stat} (%)	σ_{ptp} (%)	σ_{norm1} (%)	σ_{norm2} (%)
AMY	50.00	4.50	10.6	2.8	4.1	0.0
	52.00	4.29	4.6	2.2	4.1	0.0
	55.00	4.62	5.2	1.4	4.1	0.0
	56.00	5.19	3.7	1.1	4.1	0.0
	56.50	5.32	9.0	2.5	4.1	0.0
	57.00	4.90	4.5	1.3	4.1	0.0

Table 5.1: Summary of the R values from AMY that were used in the fit.

Experiment	$\sqrt{s}$ (GeV)	R	σ_{stat} (%)	σ_{ptp} (%)	σ_{norm1} (%)	σ_{norm2} (%)
Crystal Ball	9.39	3.48	1.15	0.0	4.6	0.0
CUSB	10.40	3.63	1.6	0.0	10.2	0.0
CLEO	10.49	3.77	1.6	0.0	6.4	0.0
DASP2	9.50	3.73	4.3	0.0	7.5	0.0
PLUTO	9.40	3.67	6.3	0.0	7.9	0.0
LENA	7.44	3.37	3.9	0.0	6.7	0.0
	8.91	3.42	2.9	0.0	6.7	0.0
	9.28	3.31	2.7	0.0	6.7	0.0
	9.42	3.57	7.6	0.0	6.7	0.0

Table 5.2: Summary of the R values from DORIS and CESR that were used in the fit.

reported by the CRYSTAL BALL collaboration [25]. All the values of R that we use for the fitting are summarized in Table 5.1–5.3, together with their errors.

Experiment	$\sqrt{s}$ (GeV)	R	σ_{stat} (%)	σ_{ptp} (%)	σ_{norm1} (%)	σ_{norm2} (%)
HRS	29.00	4.20	0.8	0.0	7.0	0.0
MAC	29.00	4.00	0.8	0.0	2.1	0.0
CELLO	14.04	4.10	2.6	2.2	1.7	0.0
	22.00	3.86	3.0	2.1	1.7	0.0
	33.80	3.74	2.6	1.9	1.7	0.0
	38.28	3.89	2.6	1.7	1.7	0.0
	41.50	4.03	4.1	1.8	1.7	0.0
	43.60	3.97	2.0	1.4	1.7	0.0
	44.20	4.01	2.5	1.2	1.7	0.0
	46.00	4.09	5.1	1.9	1.7	0.0
	46.60	4.20	8.5	1.7	1.7	0.0
JADE	14.04	3.94	3.6	0.0	2.4	0.0
	22.00	4.11	3.2	0.0	2.4	0.0
	25.01	4.24	6.8	0.0	2.4	0.0
	27.66	3.85	12.5	0.0	2.4	0.0
	29.93	3.55	11.3	0.0	2.4	0.0
	30.38	3.85	4.9	0.0	2.4	0.0
	31.29	3.84	7.3	0.0	2.4	0.0
	34.89	4.17	2.4	0.0	2.4	0.0
	34.50	3.94	5.1	0.0	2.4	0.0
	35.01	3.94	2.5	0.0	2.4	0.0
	35.45	3.94	4.6	0.0	2.4	0.0
	36.38	3.72	5.7	0.0	2.4	0.0
	40.32	4.07	4.7	0.0	2.4	0.9
	41.18	4.24	5.2	0.0	2.4	0.9
	42.55	4.24	5.2	0.0	2.4	0.9
	43.53	4.05	5.0	0.0	2.4	0.9
	44.41	4.04	5.0	0.0	2.4	0.9
	45.59	4.47	5.0	0.0	2.4	0.9
	46.47	4.11	5.9	0.0	2.4	0.9

Table 5.3: Summary of the R values from PEP and PETRA that were used in the fit (continued to the next page).

Experiment	$\sqrt{s}$ (GeV)	R	σ_{stat} (%)	σ_{ptp} (%)	σ_{norm1} (%)	σ_{norm2} (%)
MARK J	22.00	3.66	2.2	3.0	2.1	0.0
	25.00	3.89	5.4	3.0	2.1	0.0
	30.60	4.09	3.4	3.0	2.1	0.0
	33.82	3.71	1.6	3.0	2.1	0.0
	34.63	3.74	0.8	3.0	2.1	0.0
	35.11	3.85	1.6	3.0	2.1	0.0
	36.36	3.78	4.0	3.0	2.1	0.0
	37.40	3.97	9.3	3.0	2.1	0.0
	38.30	4.16	2.2	3.0	2.1	0.0
	40.36	3.75	4.0	3.0	2.1	0.0
	41.50	4.32	4.6	3.0	2.1	0.0
	42.50	3.85	5.2	3.0	2.1	0.0
	43.58	3.91	1.5	3.0	2.1	0.0
	44.23	4.14	1.9	3.0	2.1	0.0
	45.48	4.17	4.8	3.0	2.1	0.0
	46.47	4.35	3.9	3.0	2.1	0.0
PLUTO	27.60	4.07	7.1	0.0	6.0	0.0
	30.80	4.11	3.2	0.0	6.0	0.0
TASSO	14.00	4.14	7.3	0.0	3.5	2.0
	22.00	3.89	4.4	0.0	3.5	2.0
	25.00	3.72	10.2	0.0	3.5	2.0
	33.00	3.74	7.2	0.0	3.5	2.0
	34.00	4.14	3.1	0.0	3.5	2.0
	35.00	4.23	2.1	0.0	3.5	2.0
	27.50	3.91	8.2	0.0	3.5	2.0
	30.10	3.94	4.6	0.0	3.5	2.0
	31.10	3.67	4.9	0.0	3.5	2.0
	33.20	4.49	6.3	0.0	3.5	2.0
	34.00	4.10	4.9	0.0	3.5	2.0
	35.00	4.04	4.2	0.0	3.5	2.0
	36.10	3.94	4.3	0.0	3.5	2.0
	41.50	4.11	2.9	0.0	3.5	3.0
	44.20	4.28	3.8	0.0	3.5	3.0

Table 5.3: (continuing from the previous page)

In the fit, M_{Z^0} was treated as the only free parameter of the electroweak theory, as discussed in Chapter 1, and $\sin^2\theta_W$ is related to M_{Z^0} through equation 1.18 (Δr was fixed at 0.070). The QCD scale parameter $\Lambda_{\overline{MS}}$ was the other free parameter in the fit. We used both the $O(\alpha_S^2)$ correction and the $O(\alpha_S^3)$ correction, and compared the results of the two fits. In the QCD calculation, the number of flavors, n_f, was taken to be 5 in the enregy region concerned, which is consistent with the $\overline{MS}$ prescription [84].

For the $O(\alpha_S^3)$ QCD correction, the third order correction factor, $1+C_1(\alpha_S/\pi)+C_2(\alpha_S/\pi)^2+C_3(\alpha_S/\pi)^3$, was used in equation 1.9. The relation between α_S and $\Lambda_{\overline{MS}}$, which are correct up to $O(\alpha_S^3)$, are obtained by integrating the third-order renormalization group equation [85],

$$\frac{\partial a}{\partial \ln|s|} = \beta(a) = -\beta_0 a^2 - \beta_1 a^3 - \beta_2 a^4 = -\beta_0 a^2\left(1 + c_1 a + c_2 a^2\right), \qquad (5.41)$$

where $a = \alpha_S/\pi$, $\beta_0 = \frac{1}{12}(33-2n_f)$, $\beta_1 = \frac{1}{48}(306-38n_f)$, and $\beta_2 = \frac{1}{64}(\frac{2857}{2} - \frac{5033}{18}n_f + \frac{325}{54}n_f^2)$; numerically, $\beta_0 = 1.917$, $c_1 = 1.261$, and $c_2 = 1.475$ for $n_f = 5$. The result is

$$\begin{aligned}\ln\frac{s}{\Lambda} &= \frac{1}{\beta_0 a} + \frac{c_1}{\beta_0}\ln\frac{c_1 a}{1+c_1 a} + \frac{c_1}{2\beta_0}\ln\frac{(1+c_1 a)^2}{1+c_1 a+c_2 a^2} \\ &\quad + \frac{2c_2 - c_1^2}{\sqrt{\Delta}\beta_0}\left[\tan^{-1}\frac{c_1+2c_2 a}{\sqrt{\Delta}} - \tan^{-1}\frac{c_1}{\sqrt{\Delta}}\right] \qquad (5.42)\end{aligned}$$

$$\Lambda_{\overline{MS}}^2 = \bar{\Lambda}^2\left(\frac{c_1}{\beta_0}\right)^{\frac{c_1}{\beta_0}} \qquad (5.43)$$

where $\Delta = 4c_2 - c_1^2$ [8]. For a given $\Lambda_{\overline{MS}}$ and s, α_S can be obtained by solving the above equation iteratively. However, in order to faciliate quick evaluation of α_S, a look-up table for $\Lambda_{\overline{MS}}^2/s$ vs. α_S was prepared and used for the fitting calculations.

First, with $\Lambda_{\overline{MS}}$ fixed at 0.2 GeV, we fit the AMY R values alone to obtain

$$M_{Z^0} = 87.6^{+3.5}_{-2.9}\ \text{GeV/c}^2 \quad \text{with } O(\alpha_S^3)\text{ QCD}, \qquad \chi^2/\text{n.d.f.} = 4.5/5. \quad (5.44)$$

Here the fitting error is quoted at $\Delta\chi^2 = 1.0$, corresponding to a 68% confidence level error. Roughly speaking, the fitting error is dominated by the 4.1% overall normalization error.

Second, we fit all the R values listed in Tables 5.1–5.3 with the results;

$$\begin{aligned} M_{Z^0} &= 88.8^{+2.0}_{-2.0}\ \text{GeV/c}^2 & \Lambda_{\overline{MS}} &= 0.29^{+.26}_{-.18}\ \text{GeV} \\ &\text{with } O(\alpha_S^2)\text{ QCD} & \chi^2/\text{n.d.f.} &= 56.9/76, \end{aligned} \qquad (5.45)$$

$$\begin{aligned} M_{Z^0} &= 88.8^{+2.0}_{-2.0}\ \text{GeV/c}^2 & \Lambda_{\overline{MS}} &= 0.17^{+.15}_{-.11}\ \text{GeV} \\ &\text{with } O(\alpha_S^3)\text{ QCD} & \chi^2/\text{n.d.f.} &= 57.0/76. \end{aligned} \qquad (5.46)$$

The fitted curve is shown in Fig. 5.1; it describes all the data points well. The contour plots of χ^2 are shown in Figs. 5.2; the correlation between M_{Z^0} and $\Lambda_{\overline{MS}}$ seems very small. Whether or not the third-order QCD corrections are included, the fitted values of M_{Z^0} are almost identical and are very close to that obtained by the fitting to the AMY data alone. They are smaller than, although marginally consistent with, that obtained at the CERN $\bar{p}p$ collider, 91.9 ± 1.8 GeV/c^2. The value of the Weinberg angle, $\sin^2\theta_W = 0.254^{+0.019}_{-0.016}$, that corresponds to $M_{Z^0} = 88.8 \pm 2.0$ GeV/c^2, is larger than, although marginally consistent with, the world average value, 0.230 ± 0.0048 [15]. The fitted value of $\Lambda_{\overline{MS}}$, on the other hand, are very different for the fits with and without third order corrections. The value with the third-order corrections is about twice smaller than that without them. This result confirms the analyses by Gorishny et al. [8] and Marshall [83]. The values of $\alpha_S(34^2\text{GeV}^2)$ are $0.149^{+0.021}_{-0.024}$ without the third-order corrections and $0.134^{+0.017}_{-0.020}$ with them.

Since there is some ambiguity in dividing the systematic error into the point-to-point and the overall normalization error, we tried several different fits where the error divisions were varied within reasonable limits. The fitting result is found to be insensitive to the particular choice of divisions.

There might be, however, sizable correlations between different experiments through, for example, the radiative corrections. Because most of the experiments used the same program (BKJ) to calculate radiative corrections, the systematic errors in the calculation are correlated between them. The radiative corrections due to hard photon emission are dependent on the hadronic cross section at small $\sqrt{s}$ and therefore might provide a correlation between the R values from different experiments. However, because the radiative corrections always appear as a product with the detector acceptance which are experiment-dependent, these possible correlations may be less significant. We examined the effect of possible correlations by introducing non-zero off-diagonal elements in V_{ij} between the different experiments. We set $V_{ij} = (1\%)^2$ for different experiments and found that the results did not change significantly.

We also did fits without using the DORIS/CESR data; these resulted in

$$M_{Z^0} = 89.2^{+2.1}_{-2.0}\ \text{GeV/c}^2 \qquad \Lambda_{\overline{MS}} = 0.43^{+.43}_{-.29}\ \text{GeV}$$
$$\text{with } O(\alpha_S^2)\ \text{QCD} \qquad \chi^2/\text{n.d.f.} = 52.9/67, \tag{5.47}$$

$$M_{Z^0} = 89.2^{+2.2}_{-2.0}\ \text{GeV/c}^2 \qquad \Lambda_{\overline{MS}} = 0.25^{+.25}_{-.16}\ \text{GeV}$$
$$\text{with } O(\alpha_S^3)\ \text{QCD} \qquad \chi^2/\text{n.d.f.} = 53.1/67. \tag{5.48}$$

A comparison of the $\Lambda_{\overline{MS}}$ values so obtained with the results of Eqs. 5.45 and 5.46 indicates that the QCD corrections are stable across the b-quark flavor threshold. $\Lambda_{\overline{MS}}$ is slightly higher without the DORIS/CESR data, but the large fitting errors make this difference not very significant. These values correspond to $\alpha_S(34^2\text{GeV}^2) = 0.161^{+0.028}_{-0.031}$ without the third-order corrections and $\alpha_S(34^2\text{GeV}^2) = 0.144^{+0.021}_{-0.021}$ with them, in agreement with those obtained with the DORIS/CESR data.

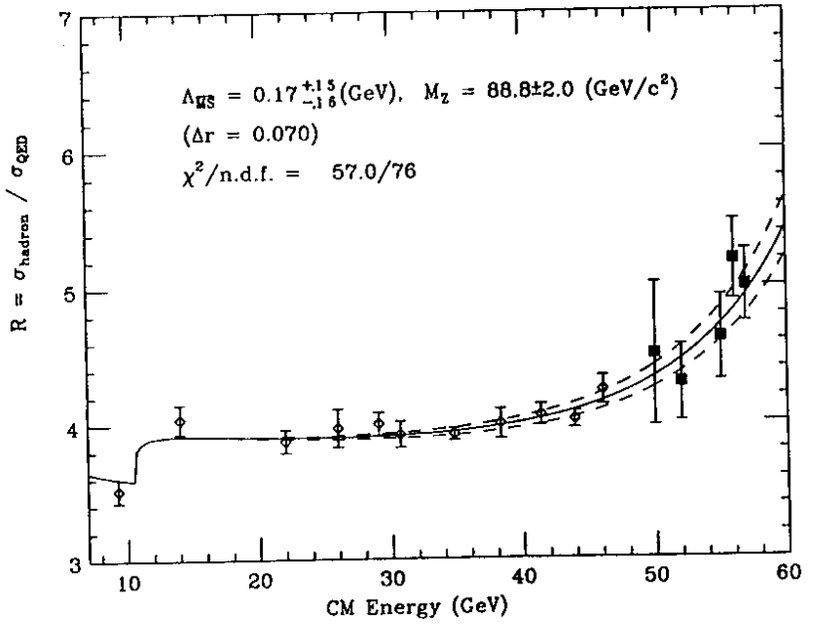

Figure 5.1: The result of the fit for M_{Z^0} and $\Lambda_{\overline{MS}}$ with $O(\alpha_S^3)$ QCD. The fitted curve is shown with the R values that are averaged in similar energy regions. The dotted lines indicate a region allowed by the fitting error of $\Delta M_{Z^0} = \pm 2.0$ GeV/c^2.

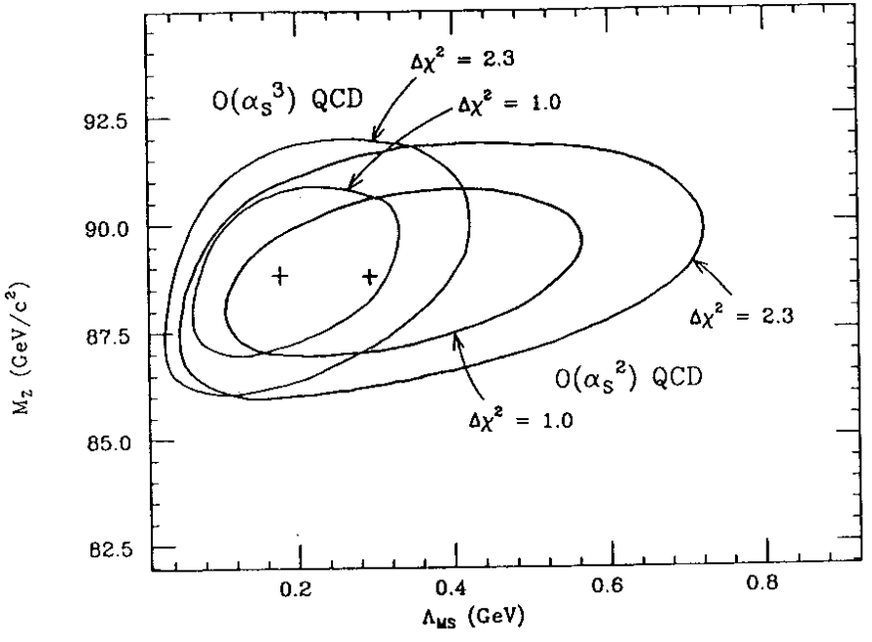

Figure 5.2: The contour plots of χ^2 with $O(\alpha_S^2)$ QCD and with $O(\alpha_S^3)$ QCD.

So far we have used the fixed value of Δr (=0.07), but since the estimation of Δr is ambiguous mainly due to unknown t quark mass (see Fig. 1.6), we estimate the effect of a different choice for the value of Δr by regarding both M_{Z^0} and Δr as free parameters in the fit. Here $\Lambda_{\overline{MS}}$ is fixed at 0.2 GeV using the $O(\alpha_S^3)$ QCD relation. (In this case $\sin^2\theta_W$ is calculated from M_{Z^0} and Δr using Eq. 1.18.) This gives the results:

$$\begin{aligned} M_{Z^0} &= 87.6^{+2.3}_{-1.8}\ \mathrm{GeV/c^2} & \Delta r &= -0.03^{+.11}_{-.09} \\ \text{with } O(\alpha_S^3)\ \mathrm{QCD} & & \chi^2/\mathrm{n.d.f.} &= 56.3/76. \end{aligned} \tag{5.49}$$

The contour plot of χ^2 is shown in Fig. 5.3. In Fig. 5.3 only a small dependence of M_{Z^0} on the value of Δr is seen. Thus, the value of M_{Z^0} obtained from the fits to the R values tends to be small even if the size of the radiative corrections, i.e, the t quark mass, is allowed to vary. The fit values correspond to $\sin^2\theta_W \sim 0.228$, which is in good agreement with the world average value. It is worth noting that the fit result for Δr indicates heavier t quark mass, although its fitting error is fairly large.

Our data contribute in determining M_{Z^0} while their contribution to the determination of $\Lambda_{\overline{MS}}$ is rather small, because the QCD effects decrease logarithmically to only about 5% at the TRISTAN energy. In order to evaluate how much our data contribute to the fit results of the electroweak parameters, simultaneous fits of M_{Z^0} and $\sin^2\theta_W$ were made to our data only, the lower energy data only, and all the data, and the fit results for these three cases were compared. ($\Lambda_{\overline{MS}}$ is fixed at 0.2 GeV using the $O(\alpha_S^3)$ QCD relation for these fits.) The results are shown in Figs. 5.4 and 5.5. It is evident that while our data are rather insensitive to the value of $\sin^2\theta_W$, its contribution in decreasing the errors of M_{Z^0} is significant. It is also noticed that the values of M_{Z^0} obtained without our data also indicate a lower value as compared to that measured at the CERN $\bar{p}p$ collider. The fit to all the combined data resulted in

$$\begin{aligned} M_{Z^0} &= 87.6^{+2.3}_{-1.8}\ \mathrm{GeV/c^2} & \sin^2\theta_W &= 0.228^{+.031}_{-.022} \\ \text{with } O(\alpha_S^3)\ \mathrm{QCD} & & \chi^2/\mathrm{n.d.f.} &= 56.3/76. \end{aligned} \tag{5.50}$$

The fit value of $\sin^2\theta_W$ agree very well with the world average value (0.230 ± 0.0048). However, the value of M_{Z^0} is somewhat smaller, although marginally consistent with, that obtained by the direct measurement (91.9 ± 1.8 GeV/c^2).

In summary, global fits of our R values, taken together with the lower energy measurements, result in reasonably good χ^2 values, and the fitted values describe all the R values in a broad energy range well. The fits consistently give a rather low value of M_{Z^0}, $\sim$ 89 GeV/c^2, suggesting that our seemingly large R values can be an indication of slightly lower M_{Z^0} than that measured at the $\bar{p}p$ collider, although it is still marginally consistent with the $\bar{p}p$ result. The effects of the third-order QCD corrections were also examined and found large: the resulting $\Lambda_{\overline{MS}}$ is about half that without the third-order corrections. However, the errors from the fit are large ($\sim$ 100%). In terms of α_S, these results correspond

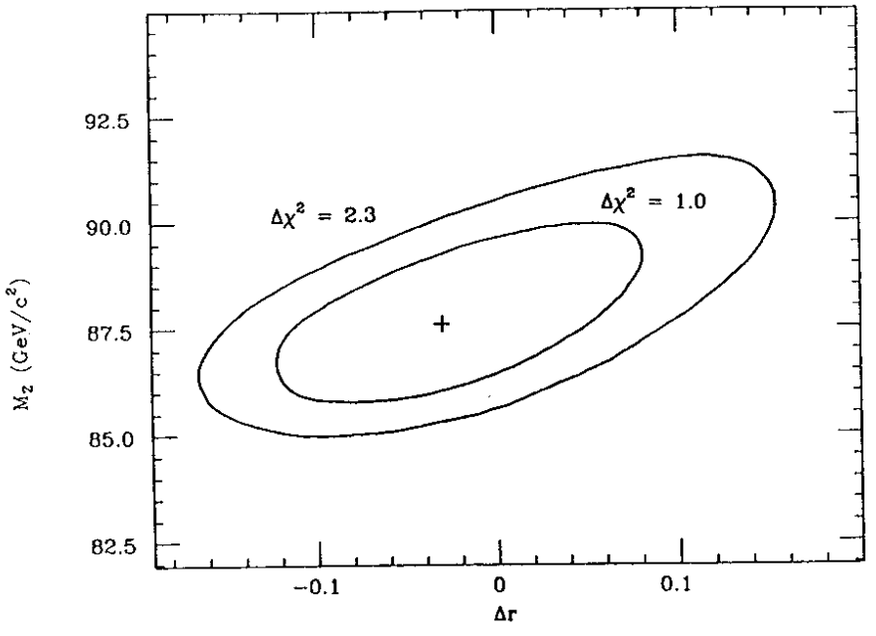

Figure 5.3: The contour plot of χ^2 for the fit varying M_{Z^0} and Δr.

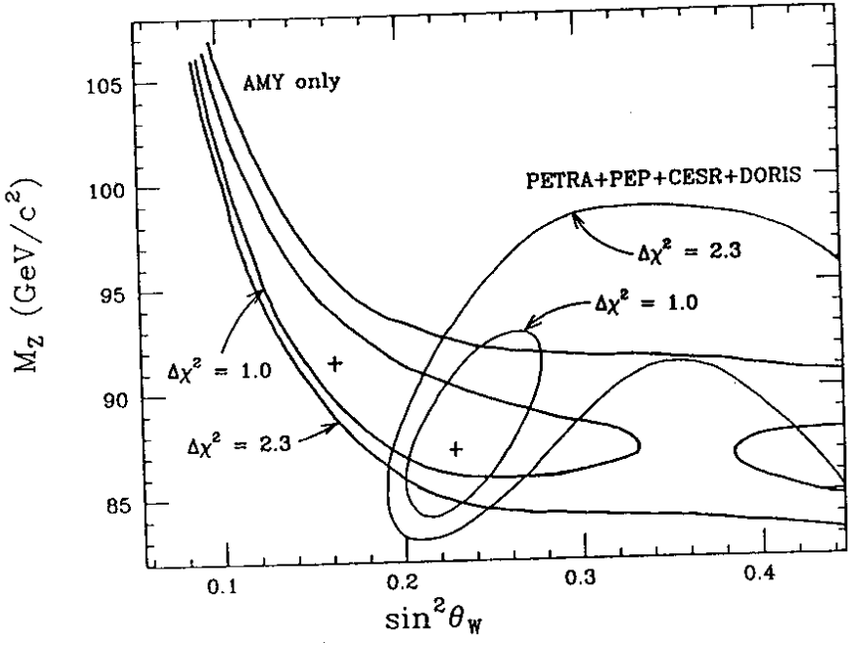

Figure 5.4: The contour plot of χ^2 for the fits varying M_{Z^0} and $\sin^2\theta_W$. The results of the fit to the AMY data only and that to the other data are compared.

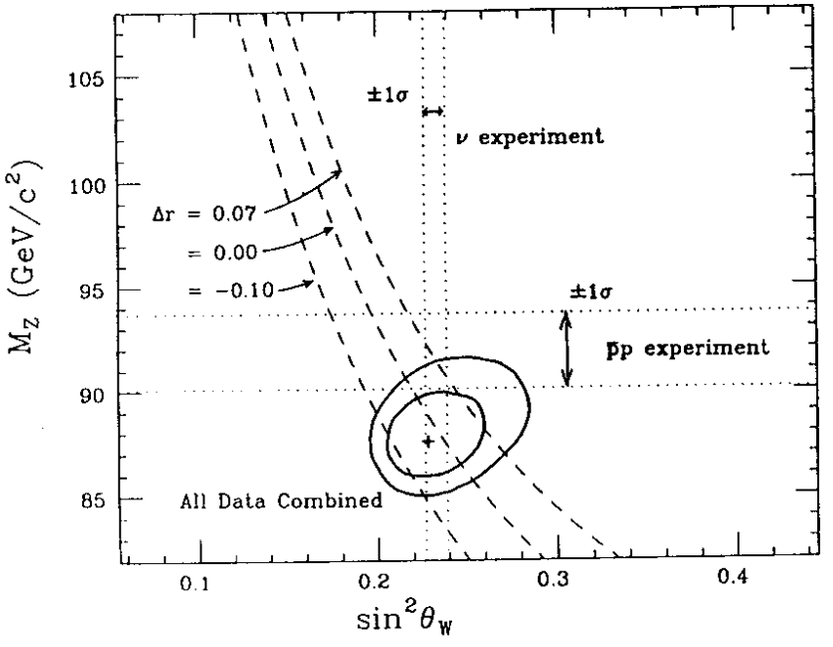

Figure 5.5: The contour plot of χ^2 for the fits varying M_{Z^0} and $\sin^2\theta_W$. All the data were used for the fit.

to $\alpha_S(34^2\text{GeV}^2) = 0.134^{+0.017}_{-0.020}$ ($\alpha_S(34^2\text{GeV}^2) = 0.149^{+0.021}_{-0.024}$) with (without) the third-order corrections. These results are compatible with the values of $\Lambda_{\overline{MS}}$ measured by other methods [10].

Chapter 6

Conclusion

In this thesis we have reported on a study of the hadronic events observed by the AMY detector at the TRISTAN e^+e^- collider.

With a data sample corresponding to an integrated luminosity of 19.3 pb^{-1} with center-of-mass energies ranging from 50 GeV to 57 GeV, a total of 2280 hadronic events were selected. The R values (or the total cross sections) were then determined with an overall normalization error of 4.1% and point-to-point systematic errors that range from 1.1% to 2.8%. The normalization error corresponds to $\Delta M_{Z^0} \sim 2.6$ GeV/c^2 or $\Delta \sin^2\theta_W \sim 0.02$ at $\sqrt{s} = 57$ GeV.

For the first time, the complete electroweak calculations were used to correct the data for the radiative effects. It was found that the approximate calculations used for the PEP and the PETRA experiments begin to deviate from the complete calculations as energy becomes higher, to the point where they are no longer valid at the highest TRISTAN energies.

Although the 4.1% normalization error is reasonably small compared to that of other experiments, possible ways to reduce this number were considered. We have identified improvements that make it reasonable to expect that it could be reduced down to about the 2% level.

The R values thus obtained were compared to the standard model prediction with five quark flavors. The results are consistent with the model, although the data tend to be systematically higher than the prediction. Using this result, open production of top quarks is excluded in our energy range with a 95% confidence level.

By further examining event shape variables (thrust and acoplanarity), a more sensitive search for new heavy quarks was carried out. No significant deviation from the prediction with five quark flavors was found. At the highest energy, 57 GeV, 95% confidence level upper limits for the possible increase in R due to the new heavy quark production were obtained as $R_{t\bar{t}} < 0.358 \pm 0.027$ and $R_{b'\bar{b}'} < 0.325 \pm 0.024$ for the heavy quarks with masses less than 27.5 GeV/c^2. Using the threshold behavior of the quark-parton model, conservative lower limits of the new heavy quark masses of $m_t > 27.6$ GeV/c^2 and $m_{b'} > 25.5$ GeV/c^2 were established. More realistic limits including the electroweak and the QCD effects were also determined; the results are $m_t > 28.4$ GeV/c^2 and $m_{b'} > 26.8$ GeV/c^2.

It is, however, important to note that, because of its small expected cross section, the possibility of pair-production of b' quarks at our highest energies is not completely excluded.

Finally, global fits of standard model predictions to our measured R values, together with results from lower energies, were carried out. The obtained χ^2 is acceptable, and the fitted values describe all the R values reasonably well. Our data, in spite of having smaller statistics, are more sensitive to M_{Z^0} than the PEP and the PETRA experiments, and help to decrease the errors in the determination of M_{Z^0}. The fits consistently give a rather low value of M_{Z^0}, $\sim 89 \pm 2$ GeV/c^2. It is suggested that our seemingly large R values can be an indication of slightly lower M_{Z^0} than measured at the $\bar{p}p$ collider, although it is still marginally consistent with the $\bar{p}p$ result.

The effects of including the recently calculated third-order QCD corrections were examined. The effects are large: the resulting $\Lambda_{\overline{MS}}$ is approximately half that determined without the third-order corrections. This result casts a question on the reliability of the QCD perturbative calculations for the R values. It may be that the second-order corrections just happen to be small and the perturbation series become stable for subsequent orders. However this question will have to wait for the fourth-order calculations to be done; this is not expected to occur any time in the near future. In terms of α_S, these results correspond to $\alpha_S(s) = 0.134^{+0.017}_{-0.020}$ ($\alpha_S(s) = 0.149^{+0.021}_{-0.024}$) at $s = 34^2\text{GeV}^2$ with (without) the third-order corrections and are compatible with the values measured by the other methods.

Appendix A

The CDC and its Calibration

The design, construction and operation of the Central Drift Chamber of the AMY detector is described. The chamber has a very high cell density and operates in a non-uniform magnetic field of more than 3 tesla. In order to make the chamber transparent to X-rays in the 10 KeV range, low-Z materials were used in its construction. The procedures used to calibrate the chamber and for determining the relation between the drift-times and the drift-distances are discussed.

A.1 The Central Drift Chamber

In recent years, the use of large solid-angle magnetic detectors in conjunction with colliding-beam storage rings has proliferated to the point where there are about twenty such devices either currently in operation or under construction. Most of these detectors are remarkably similar; typically there is a tracking region that extends for 1~1.5 meter in a magnetic field of $B \simeq 1$ tesla. The transverse momentum (p_t) resolution for such devices is given by the relation [87]

$$\frac{\Delta p_t}{p_t} \propto \frac{\sigma_s p_t}{L^2 B \sqrt{N}} \qquad (A.51)$$

where σ_s is the spatial resolution, L is the tracking distance, and N is the number of measured points. With gas tracking detectors that have typical spatial resolutions of $\sim 150\mu$m, these systems provide a transverse momentum resolution of order $\Delta p_t/p_t \sim 1\% \times p_t(\mathrm{GeV/c})$. Since the p_t resolution is inversely proportional to L^2B, any reduction of the size of the tracking region requires a quadratic increase in the size of the magnetic field, if one is to preserve the resolution. Thus, a factor of 2 reduction in tracking length requires a factor of 4 increase in field to the ~3 or 4 tesla range.

In large solid-angle devices, a reduction in the size of the charged particle tracking volume allows for a corresponding reduction in size for all of the other elements of the detector. In addition to reducing the constraints on the configuration of the storage ring components, it can result in a significant reduction in cost and enable the use of more expensive materials in the detection elements. Also, backgrounds to muon identification caused by π and K decay-in-flight are reduced.

There are, however, many difficulties that must be faced when operating detectors in such high magnetic fields. For example, in gas detectors, the bending in the magnetic field causes the drift trajectories of ionization electrons to make an angle with respect to the electric field line (the so-called Lorentz angle). In a 3 tesla field, this angle can be of order 80°, resulting in complex spiraling drift trajectories rather than simple straight line drift paths that are desirable in high resolution drift devices.

The AMY detector is an attempt to reduce the size of a general purpose detector by using a 3 tesla solenoidal magnetic field. The device consists of tracking and shower detectors located inside of a solenoidal magnet. The coil is surrounded by a steel flux return yoke followed by a drift chamber/scintillation counter muon identification system. The primary charged particle tracking detector is a 40-layer cylindrical drift chamber (CDC) comprised of 25 axial and 15 small angle stereo layers. In this appendix we give a description of the AMY CDC, including details of the design, construction and some results from our initial operation in the 3 tesla magnetic field.

One of the challenges for a large solid-angle detector is to distinguish electrons (and positrons) from the much more numerous charged π and K mesons that are produced. In AMY, the intent is to exploit the fact that secondary electrons produce synchrotron radiation as they bend in the high magnetic field. For example, a 10 GeV/c electron radiates 11 X-rays, totalling about 1 MeV in energy, as it traverses the tracking volume of the AMY detector. To exploit these signals, it was necessary to make the CDC transparent to ~5 KeV X-rays. This places restrictions on the structure and the materials used for the CDC; aluminium wires were used for field shaping and the gas volume is contained between very thin entrance and exit windows.

Mechanically, the chamber is a cylindrical structure containing 32,042 wires (9,048 sense wires and 22,994 field shaping wires) strung between two endplates, as illustrated in Fig. 2.4. The endplates are held apart at the inner radius ($r = 15$ cm) by a 1.0 mm thick tube made from KEVLAR and at the outer radius ($r = 67$ cm) by six Aluminum posts. The endplates are composite structures of 6 disks, which hold the wires, and hoops, which separate the disks. The length of the wires increases from 93.3 cm for the innermost disk to 179.8 cm at the outermost disk. The component parts of the endplates are bound together both by stainless steel screws and structural epoxy (3M 2216). In addition to providing structural strength, the epoxy provides the gas seal at each mechanical interface. The gas seal at the outer radius is provided by a single turn of 150 μm thick mylar foil. The outer mylar gas seal is supported between each of the six outer posts by thin composite structures ("windows") of aluminized mylar, ROHACELL foam and ordinary mylar.

Each disk contains a number of cylindrical layers of close packed hexagonally shaped drift cells: a typical arrangement is indicated in Fig. A.1. Ionization signals are detected by 20μm diameter gold plated tungsten sense wires situated at the center of each cell. The outer corners of the hexagonal cells are defined by 160μm diameter gold plated aluminum field wires. The sense wires are typically

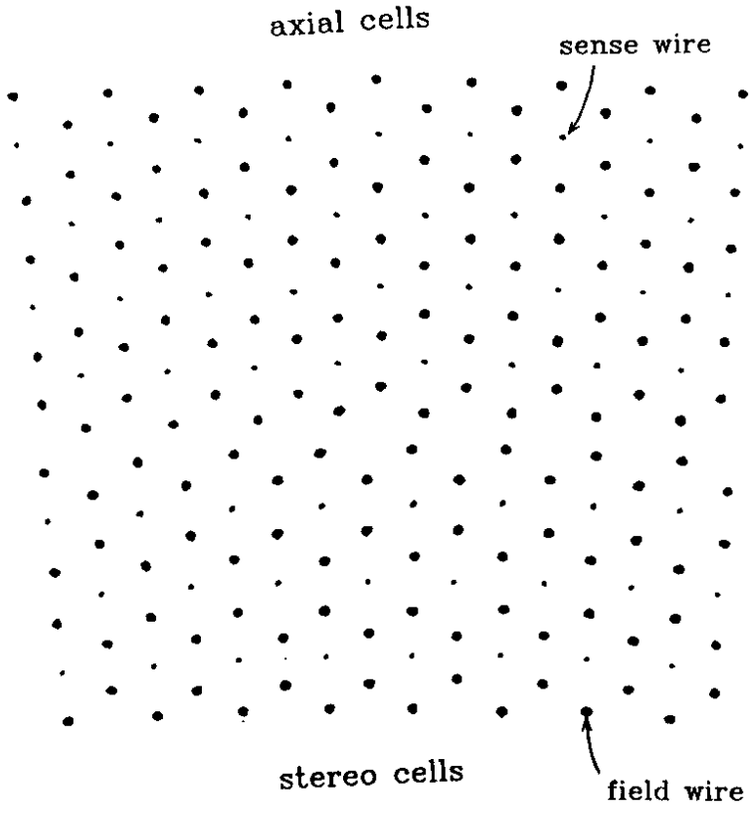

Figure A.1: The cell configuration of drift cells in a CDC disk.

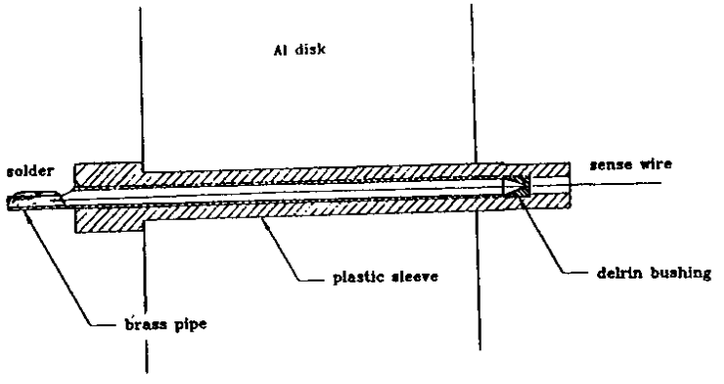

Figure A.2: The mechanism to hold wires at the CDC endplate.

held at +1.8kV; this provides an electric field to cause the ionization electrons to drift to the sense wire and a gas gain of approximately 40,000 due to multiplication processes near the sense wire. The average cell radius is 5.5 mm. Because of the different radius of each layer, the cell size differs slightly from layer to layer. Disk 1 has five cylinders of axial wires; Disks 2 through 6 each have 3 cylinders of small angle stereo wires near the inner radius followed by 4 cylinders of axial wires. The stereo angle is about 4.7°; it varies slightly from disk to disk.

The wires are held at each endplate by special bushings that are inserted in holes in the disk sections of the endplates, as shown in Fig. A.2. The overall uncertainty of the position of the sense wires is of order $\pm 50\mu m$ (σ). The wire is held in place and connected electrically to the brass post of the bushing by means of solder. Electrical connections to the sense and field wires are made by means

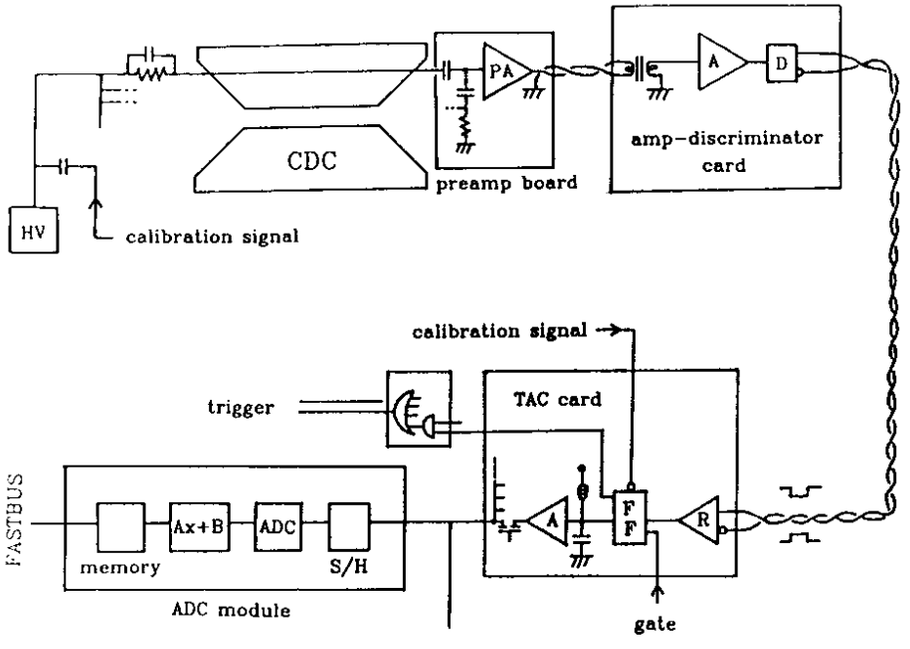

Figure A.3: Diagram of a sequence of electronics processing the CDC signals.

of a set of printed circuit boards with minispring connectors arranged to match the pins in the wire bushings. One set of inter-connection boards strapped all of the field wires together and to ground. The other set is comprised of eight layer printed circuit boards that attach to the sense wires. These boards distribute the HV and pre-amplify the signals from each sense wire. In addition, these boards distribute and gate timing calibration signals for each of the electronics channels. Tubes carrying cooling water are attached to the endplates to remove the $\sim$ 700 Watts of heat produced by the preamplifiers at each end of the drift chamber.

Signals from each sense wire are processed by a sequence of electronic circuits as illustrated in Fig. A.3. A hybridized current sensing preamplifier with a gain of 8 mV/μA and a rise time of 4.8 nsecs is mounted directly on the endplate of the chamber and provides a differentially driven signal that is transformer coupled

to an Amplifier-Discriminator circuit that is located near the detector. Sense wire signals that are above $\sim 1\mu$A fire the discriminator, producing differential ECL logic signals that are transmitted via twisted pair cable to a FASTBUS based TAC/ADC system in a nearby electronics hut. The time resolution of the TAC/ADC system is 0.3 nsecs (σ).

A.2 Chamber Calibration

The detector is triggered on Bhabha events in the SHC by large pulse heights in the shower counter and independently by two-track configurations in the tracking chambers. A sample of approximately 1600 Bhabha scattering events ($e^+e^- \rightarrow e^+e^-$), collected at $E_{cm} = 52$ GeV, was used to evaluate the performance of the central tracking chamber and the central shower counter. We summarize the results of these measurements here.

For no magnetic field, the drift trajectories follow the electric field lines as shown in Fig. A.4, and are easily understood. With a central field of 3 tesla, the effects of the large Lorentz angle results in complicated trajectories; Fig. A.5 shows a computer model calculation of what they look like. This is a big effect; for $B = 0$, the maximum drift time is about 150 nsecs (corresponding to the maximum drift distance of 5.5 mm), for $B = 3$ tesla this increases to about 700 nsecs. However, thanks to the hexagonal shape of the drift cells, contours of equal drift-times (isochrones) are fairly circular for most of the drift region. Thus, the drift-distance is simply a monotonically increasing function of drift-time, independent of the entrance angles of the particles.

We determined the time-to-distance function as follows. We have a pulser-calibration system, with which we pulse the TAC modules and the chamber every day to calibrate the timing and the linearity of the system. Using the obtained calibration data, the data from the CDC are automatically converted into nanoseconds, and relative timings between different channels are adjusted to coincide within 10 nsecs. By examining the leading edge of the drift time distributions, the starting time (t_0) was determined as a single constant for the entire chamber. By noting that drift-distance is a monotonic function of drift-time, a zero-th order time-to-drift function was guessed in such a way that the obtained drift-distance distribution would become flat.

With this simple time-to-drift function, the track finding program ACE could reconstruct the tracks in the Bhabha events very efficiently. The r-ϕ projection of the two tracks in the Bhabha event was then fitted to a circle. From the fitted curves we can infer the distance between the trajectory and the wire position for each cell and use this to iteratively improve on the time-to-drift relation. Corrections such as flight-time of the particles and the propagation delay along the sense wires are carried out here. A scatter-plot of inferred drift-distances vs. the measured drift-times for all cells is shown in Fig. A.6. The width of this distribution, for a given drift-distance, which is a measure of the resolution, appears very broad. What is happening becomes clearer when we separate the

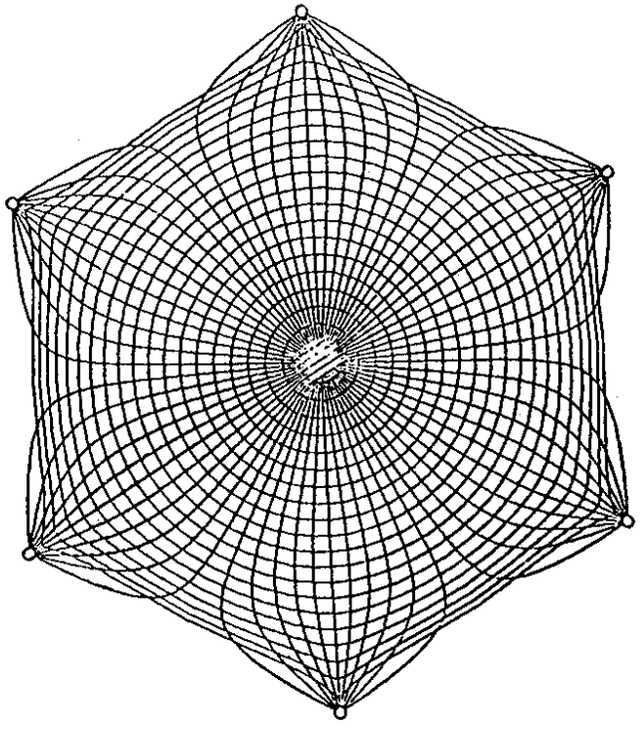

Figure A.4: The drift trajectories inside a CDC cell calculated for the case of no magnetic field.

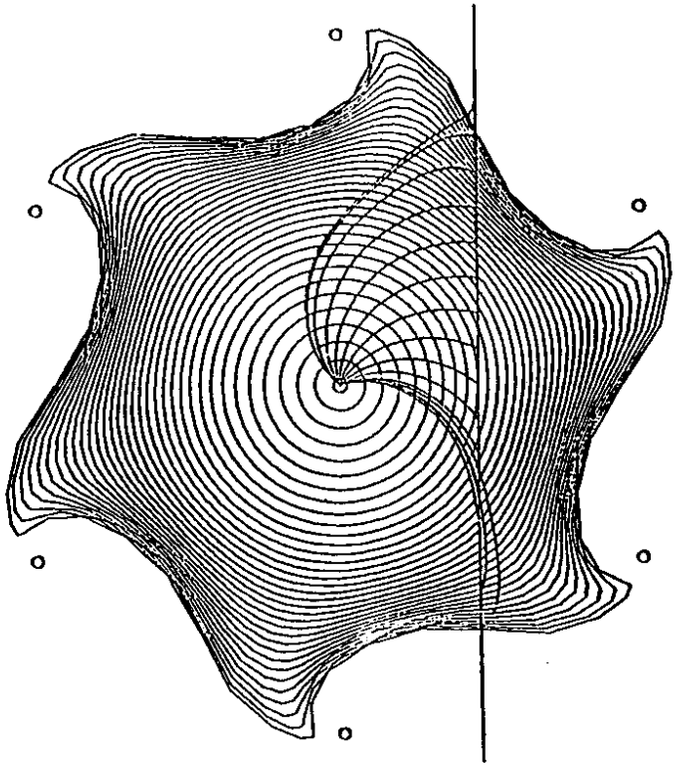

Figure A.5: The drift trajectories inside a CDC cell calculated for the case of 3 tesla magnetic field.

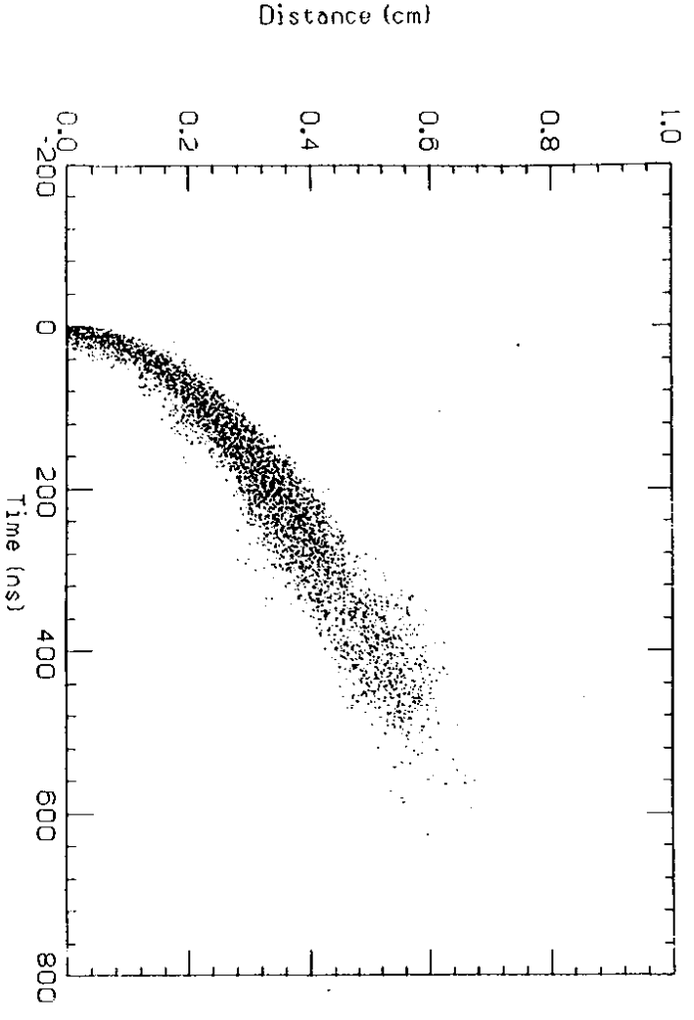

Figure A.6: A scatter-plot of inferred drift distances vs. the measured drift times for all cells.

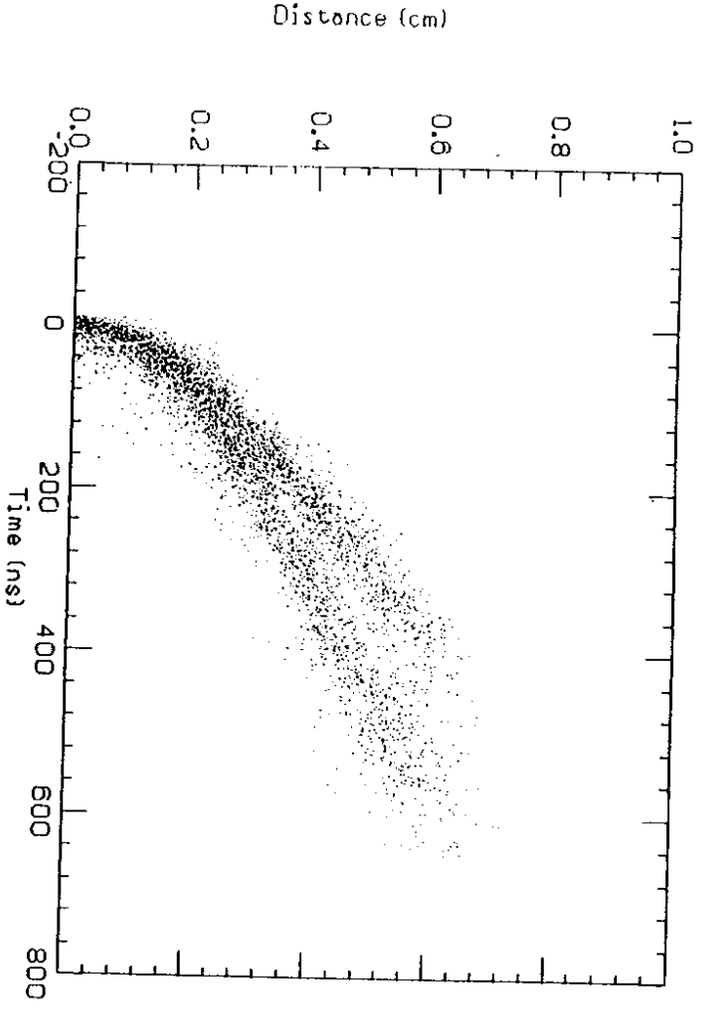

Figure A.7: A scatter-plot of inferred drift distances vs. the measured drift times for all cells, plotted only for outer layers.

inner cells in a given disk (cylinders 2 and 3) from the outer cells (cylinders 1 and 4). Fig. A.7, which shows the scatterplot for only the outer layers (1 and 4) of each disk, demonstrates a curious forked structure.

This forked distribution comes from a left-right asymmetry induced by the combined effects of the Lorentz angle and an inner-outer E-field variation that exist on the inner and outer layers of each disk [86]. One prong of the forked distribution corresponds to the drifts from the left for inner layers and from the right for outer layers while the other prong corresponds to the opposite situation. The drift from the left side of the inner-most layer of a band is similar to that from the right side of the outer-most layer in a band and vice versa.

We have used a time-to-distance relation of the form

$$d = \begin{cases} v_0 t & t \le t_c \\ v_0 t_c + (F(t) - F(t_c))(1 + a_4 B) & t > t_c \end{cases} \qquad \text{(A.52)}$$

where t_c is 5 ns, $v_0 = 44$ μm/ns (the nominal saturated drift velocity in HRS gas) and $F(t) = \sqrt{a_1 t + a_2 t^2 + a_3 t^3}$. We use four different sets of coefficients a_i, one set for the left side of the inner-most layer and the right side of the outer-most layer, etc. The term $a_4 B$ is used to take into account the variation of the magnetic field (it varies from +5% to -18% of its central value over the volume of the chamber). With these drift functions, we get a spatial resolution vs drift-distance as shown in Fig. A.8. At distances less than ~1mm, the resolution is dominated by fluctuations in the ionization process and for distances greater than ~4mm by diffusion in the gas. In the region between, we measure our resolution to be $\sigma \simeq 170\mu$m. We get a measure of our momentum resolution by comparing the curvature for the e^+ and e^- tracks in the Bhabha events as shown in Fig. A.9. From the width of this distribution, we infer a transverse momentum resolution of $0.8\% \times p_t$, where p_t is in GeV/c.

Because the field is non-uniform, charged particle trajectories are slightly distorted from the simple helices that occur in a uniform field. At the high resolutions that we are currently achieving, this is a non-negligible effect. To deal with this, we use a perturbative technique that corrects the fitted trajectories for this effect. Upon application of this correction, the p_t resolution improves to $0.7\% \times p_t$.

Thus we have successfully achieved excellent resolution. However, there are still necessary corrections that we have ignored that should further improve the performance. First, the dependence of the entrance angles of the particles is becoming important at the current level of the spatial resolution. Also, different electric field strengths from layer to layer, due to different cell sizes at each layer, require specialized layer-by-layer corrections. As we accumulate more Bhabha events, gain more experience with the instrument, and study these corrections, we expect this performance to continue to improve.

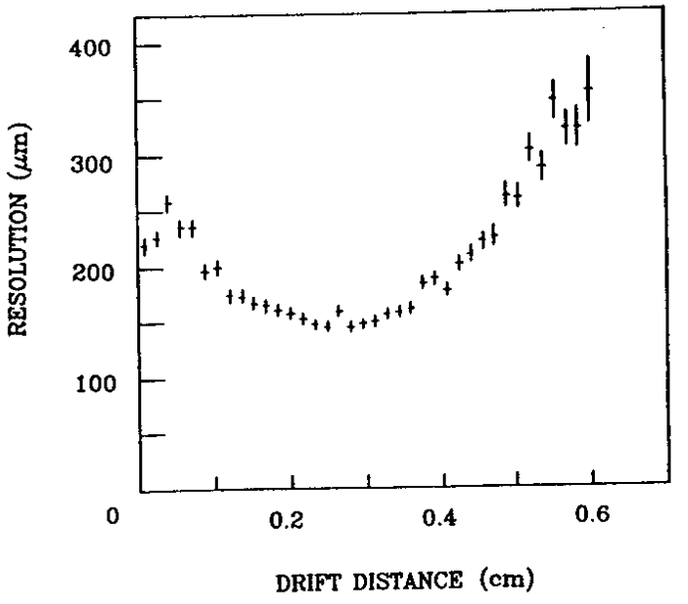

Figure A.8: The spatial resolution as a function of a drift distance.

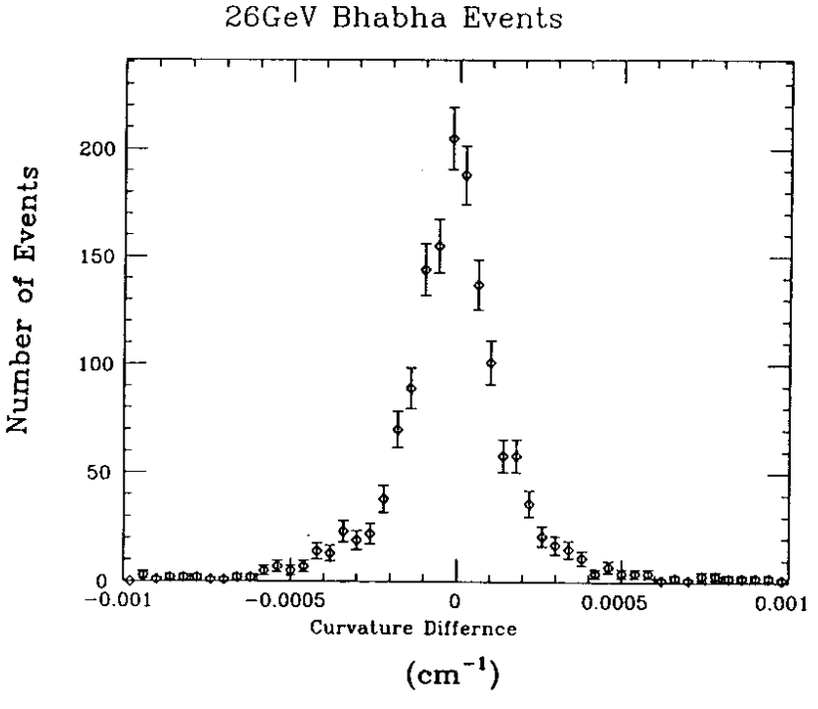

Figure A.9: Distribution of difference in curvatures of e^+ and e^- for Bhabha events.

Appendix B

Track Reconstruction of CDC

Hadronic events observed at the TRISTAN e^+e^- collider tend to have narrow jets of many charged particles. Reconstruction of the particle trajectories under such circumstances is not an easy task and requires some special considerations for both the hardware and software of the tracking device.

The central drift chamber (CDC) of the AMY detector features fine granularity and a multi-band structure to aid efficient and fast tracking. The chamber configuration of the CDC is indicated in Fig. 2.4 (Chapter 2). It consists of 6 bands; the innermost band has 5 axial cylinders of wires; each of the outer 5 bands has 4 axial and 3 stereo cylinders of wires. This band structure allows for the quick determination of independent track vectors at each band. The cell configuration of an outer band is shown in Fig. A.1 (Appendix A). The staggered hexagonal cell configuration enables a fast resolution of left-right ambiguities in addition to providing high granularity and good performance under high magnetic field.

We have developed a tracking algorithm named ACE (AMY CDC Event Tracker), which makes the most of these features of the CDC to provide fast and efficient track reconstruction, even for high multiplicity, narrow jets. This program has been used to reconstruct charged tracks of the CDC for all types of events observed by AMY.

We also use a second-stage tracking program, DUET [89], in order to improve the result of ACE's tracking for very complicated events. This program was originally developed for the tracking of the CLEO detector at the CESR e^+e^- storage ring.

In what follows, we describe the algorithms used to reconstruct tracks and the current status of the track reconstruction.

B.1 Track Finding in r-ϕ Plane

The algorithm of ACE consists of 3 steps: in the first step it finds tracks in the plane perpendicular to the beam axis (the r-ϕ plane); then stereo wires are used to obtain z coordinates for each r-ϕ track; in the third step, the chamber corrections are made and the three-dimensional tracks are fit and the momentum

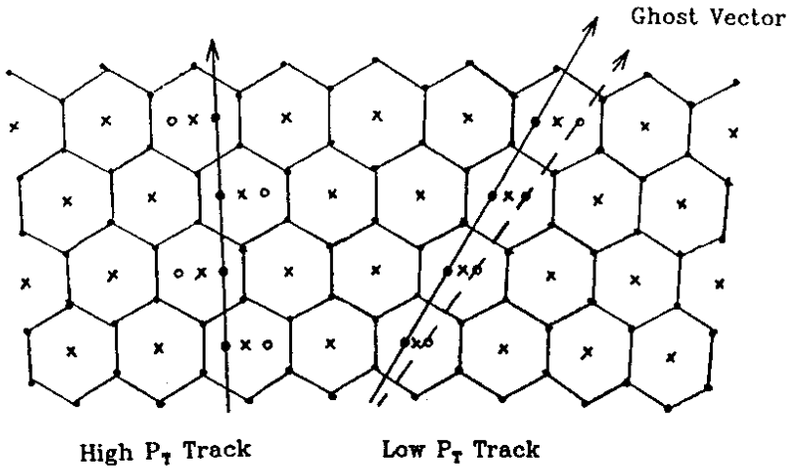

Figure B.1: The response of a CDC band to charged tracks.

vectors are calculated. In this section we describe how ACE reconstructs tracks in the r-ϕ plane.

First of all, the hit axial wires are scanned. In Fig. B.1 we show an example of the response of a CDC band to charged tracks which come from the primary vertex, i.e., our co-ordinate origin. Two hit positions are indicated for each hit wire because of the left-right ambiguities. High momentum tracks (i.e. $p_t > 1$ GeV/c) are always close to the radial direction and the resolution of the left-right ambiguities is quite straight-forward. Lower momentum tracks, which traverse outer bands with large angles relative to the radial direction, are also shown in Fig. B.1. In these cases the mirror image of the correct left-right choice may yield a "ghost" track vector.

For each hit wire on the innermost layer (or next to the innermost) of a band,

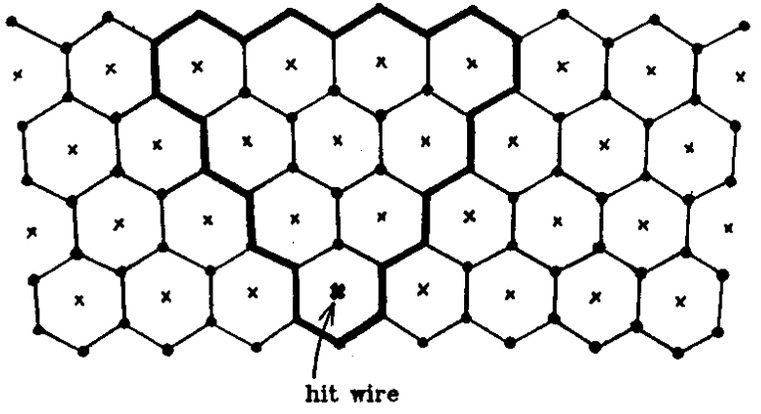

Figure B.2: ACE's search window for vector reconstruction.

hit wires are searched for in the neighboring wires in the other layers of the band. This search for hit wires is done within the pattern of the wires indicated in Fig. B.2. This search region is sensitive to track vectors with p_t as low as 250 MeV/c for the middle bands. Here we use a "road" method to find candidates of track vectors with all the ambiguities resolved. At least 3 hits (each hit in a different layer) are required to make a vector. This allows for one (or two in the case of band 1) missed hit in a band, reducing our sensitivity to chamber inefficiency and hit sharing two close tracks traversing the same wire cell.

All the vector candidates are then fitted to straight lines of the form, $\psi_i - \phi = \xi(r_i - r_1)$, where i =1,2,3,4. Here r_i refers to the radius of the i^{th} layer of the band, and ψ_i the azimuthal angle of the corresponding hit. ϕ and ξ are obtained from the fit. Only the vectors with reasonable χ^2 are accepted. The "ghost vectors," which usually have as good χ^2, are also accepted. Note that by reconstructing vectors we efficiently reject noise hits caused by background synchrotron radiation, electronics noise, etc.

Using the assumption that the track is a circle passing through the origin, the track parameters C and ϕ_0 are calculated from ϕ and ξ for each track vector, where C is the curvature of the track circle (defined as an inverse of the radius) and ϕ_0 is the azimuthal production angle (see Fig. B.3) [3]:

$$\phi_0 = \phi - \beta, \quad C = -\frac{2\sin\beta}{r_1}, \tag{B.53}$$

where $\beta = \arctan(r_1\xi)$. All the track vectors that are part of the same track should have the same values of C and ϕ_0. Comparing C and ϕ_0 for vectors in different bands, therefore, enables us to find complete tracks very quickly. Shown in Fig. B.5 is a ϕ_0-C scatter plot of the vectors for the sample event shown in Fig. B.4. (This is a real event observed at $\sqrt{s}$ = 55 GeV.) Clusters of points corresponding to tracks are clearly seen.

As can be seen from Fig. B.5, the vectors tend to cluster along lines with similar gradients, this is because the errors in calculating C and those in calculating ϕ_0 are closely correlated. It is easily shown from Eq. B.53 that

$$\frac{dC}{d\phi_0} = -\frac{2\sqrt{1-(r_1C/2)^2}}{r_1}. \tag{B.54}$$

For tracks with p_t >400 MeV/c, i.e., $r_1C/2 \ll 1$, this equation reduces to

$$dC/d\phi_0 \simeq -2/r_1. \tag{B.55}$$

The average value of $2/r_1$ for the CDC is about 0.045 cm^{-1}, which agrees with the global slope of Fig. B.5.

Since clusters tend to be separate along the direction that is perpendicular to the global slope (we label the coordinate along this direction ϕ_R), a parallelogram-shaped window, as indicated in Fig. B.5, is used to search for clusters. In order to properly define distance along ϕ_R, the distances along the C and ϕ_0 axes are

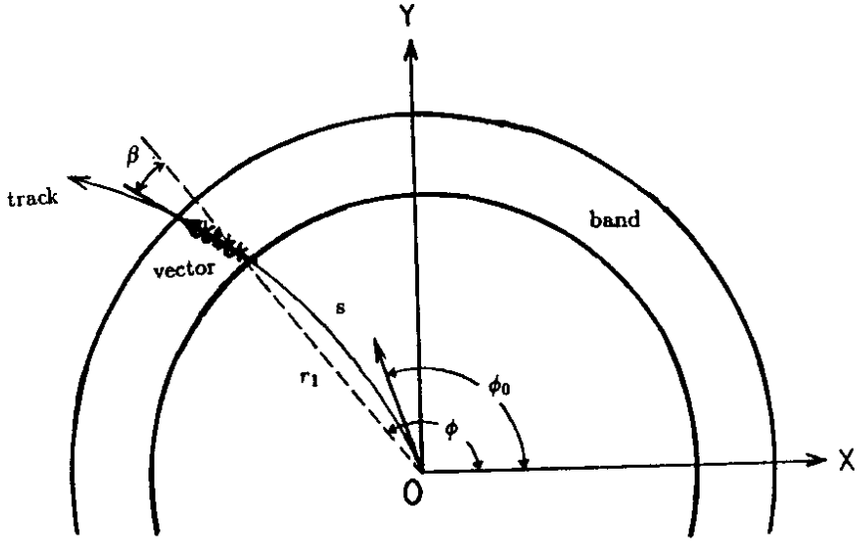

Figure B.3: Track geometry for a uniform magnetic field.

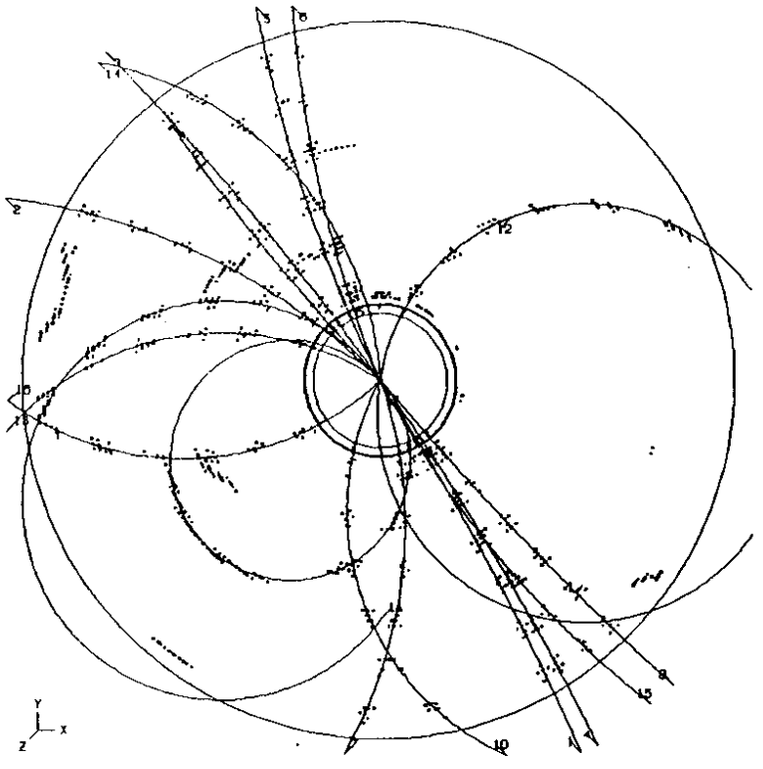

Figure B.4: An example event reconstructed by ACE.

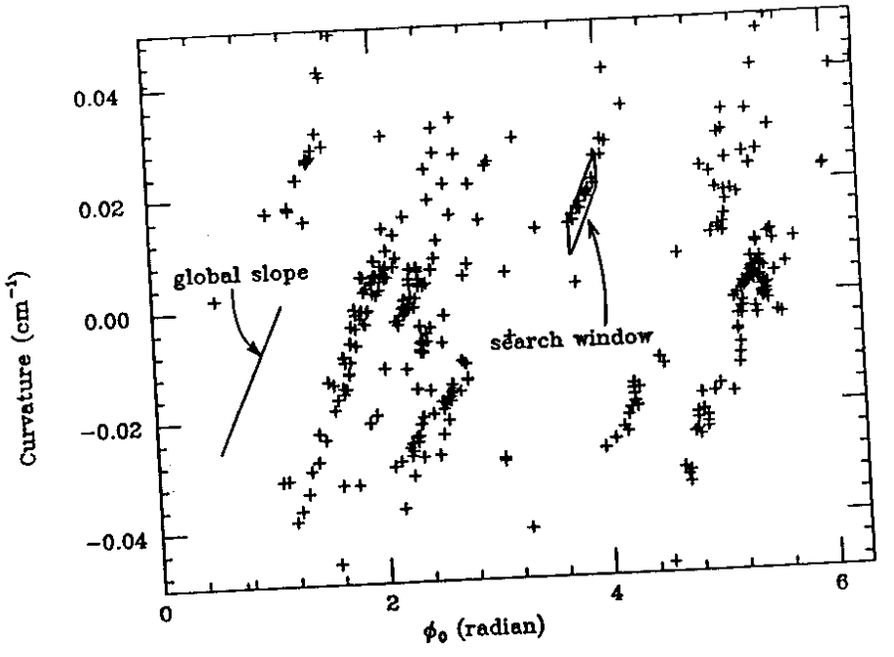

Figure B.5: An example of a scatter-plot of ϕ_0 and C for track vectors found for the event shown in Fig. B.4.

rescaled according to the calculated errors of C and ϕ_0 (σ_C and σ_{ϕ_0}). These are estimated from the spatial resolution of CDC. Searches for clusters start from the outermost vector and go inward. A found cluster is stored only if it contains vectors from different bands. Two vectors are enough to make a cluster. The size of the window is taken to be large enough, typically three times the expected spread ($\pm 3\sigma$) of the cluster, to avoid distributing vectors from the same track into two clusters. If all the vectors in the outermost band are exhausted, then the vectors in the next outermost band that are not members of any cluster are used to set windows. This process is repeated until all the vectors in the outer bands (bands 2–6) are tried.

A cluster thus found usually contains ghost vectors in addition to real ones. Furthermore, it may consist of two close tracks. Therefore, good combinations of vectors have to be identified inside of each cluster. Here we utilized a modified "Link-and-Tree" method [88] to find good track candidates in the cluster. We treat a vector as a "super-hit", which is the elementary linking object in the "Link-and-Tree" method. Two vectors in adjacent bands are linked if the distance between them in the rescaled ϕ_0-C plane is smaller than a certain value. By linking all possible combinations of vectors in the cluster, we make "trees" of vectors. Then the longest chain in the tree is chosen as the best track candidate. (The length of the chain is defined as the number of vectors in it.) Because at this point the track parameters (ϕ_0 and C) are already known to a good precision, the drift distances are corrected using them and possible missed hits due to inefficiencies in the vector-finding procedure are searched.

The best track candidate in the cluster is then fit to a circle. Note that only reasonably good track candidates can survive to the point of being fit; thus time-consuming circle-fits are avoided as much as possible. Only those circle-fits that result in a good χ^2 are finally accepted. We do not accept a track whose closest approach to the origin is more than a certain value (typically 5 cm), reflecting earlier assumptions made for calculating C and ϕ_0. (This number, 5 cm, is determined according to the size of the search window used for the clustering procedure and, therefore, depends on the spatial resolution.) For the accepted tracks, the hits located far from the fitted track are eliminated while new hits that are within an acceptable distance from the track are included. This process of fitting and refining the hits is repeated until no hit gets rejected or newly accepted.

B.2 Z-Reconstruction and Final Fits

For each r-ϕ track thus found, z coordinates are reconstructed by selecting an appropriate combination of stereo hits. (We call it a z-track.) Reconstructed r-ϕ tracks with many hits and low values of χ^2 are likely to be good high momentum tracks and are subjected to the z-track reconstruction first. For each r-ϕ track, all the hit stereo wires which cross the track in the r-ϕ plane are collected. The z-coordinate and the arc length, s, defined in Fig. B.3, are then calculated for

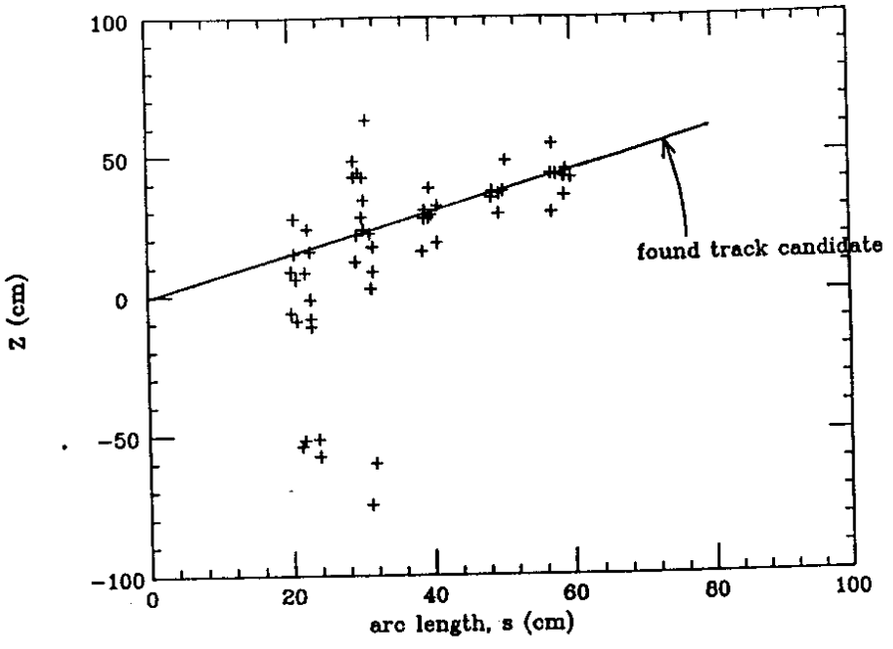

Figure B.6: An example of a s-z plot.

each stereo hit. It is easy to see that z and s are in proportion to each other for those hits that comprise a real track. As an example, we show in Fig. B.6 the s-z scatter plot of the stereo hits collected for one of the r-ϕ tracks in Fig. B.4. The correct z-track appears as a straight line in the plot. Therefore the z-track reconstruction is equivalent to finding straight lines in the s-z plot. We adopted an algorithm very similar to that used for the r-ϕ track finding: first track vectors are reconstructed in each band; then, using a modified "Link-and-Tree" method, the vectors are linked and the z-track candidates are sorted out; finally a straight-line fit is applied and the best track which passes the final criteria is stored. It is important to note that, unlike the r-ϕ tracking, the z-track finding has no bias toward tracks coming from the primary vertex.

Since we have only 3 layers of stereo wires in each band, vectors consisting

of only two hits are also accepted. This choice leaves us many fake vectors; with left-right ambiguities, two hits yield 4 vectors in total. In order to limit the number of vectors, we reject vectors that extrapolate to more than (typically) 50 cm away from the primary vertex at $s = 0$, and vectors whose directions are almost parallel to the beam axis are also rejected.

Subsequently, the vectors are linked by comparing their gradients and intersections in the s-z plot. Any three vectors which are linked in a row are regarded as a tree only if the gradient between the first two vectors is close to that for the last two vectors. This efficiently helps reduce the number of trees. However, we keep as many track candidates as possible, and reject them only after fits, because the straight-line fit is much faster than the circle fit. Finally, the best z-track, whose χ^2 is better than a certain value and whose $|z_0|$ (z_0 is z at the smallest r) is less than 50 cm, is chosen and associated with the r-ϕ track.

At this point, since we have tracks that are reconstructed in three dimensional space, the final chamber corrections are carried out using the track parameters to identify where the track passes through the chamber. The chamber corrections include the time of flight of the particles, the signal propagation time along the sense wire, and the left-right and z dependence of the time-distance function. After these corrections are made, each track is fit to a helix. Because there is a sizable non-uniformity of the magnetic field inside the CDC, a fitting routine that takes this non-uniformity into consideration is finally used (Appendix A). Since this routine corrects the particle's trajectory itself, the correct direction of the particle at any spatial point can be obtained in addition to the correct momentum vector.

B.3 Results of Tracking

We have been running ACE with our real and simulated events on the FACOM M-382 system of the KEK computer center. In the following, we present the current status of the ACE tracking.

ACE is very fast: it takes less than 20 msec per track for a typical multi-hadronic event, whether it is simulated or real, on a FACOM M-382 computer (Fig. B.7). It is also quite efficient: roughly 95 % of the particles coming from within 5 cm of the primary vertex and with $p_t \geq 500$ MeV in simulated hadronic events are reconstructed with the quality expected from the assumed spatial resolution (Fig.B.8).

However, there are a few drawbacks to ACE. First, it fails to find tracks that do not pass nearby the origin, so some secondary particles which are created at a distance from the primary vertex may not be reconstructed. But since the track vectors of those secondary particles are already reconstructed by ACE, it would not be difficult to extend the current algorithm so that they could also be linked to form tracks. Secondly, ACE is not very efficient for low momentum tracks, i.e., tracks with $p_t < 400$MeV/c. This is because at least two fairly radial vectors are required for reconstruction. This problem could be solved by expanding the

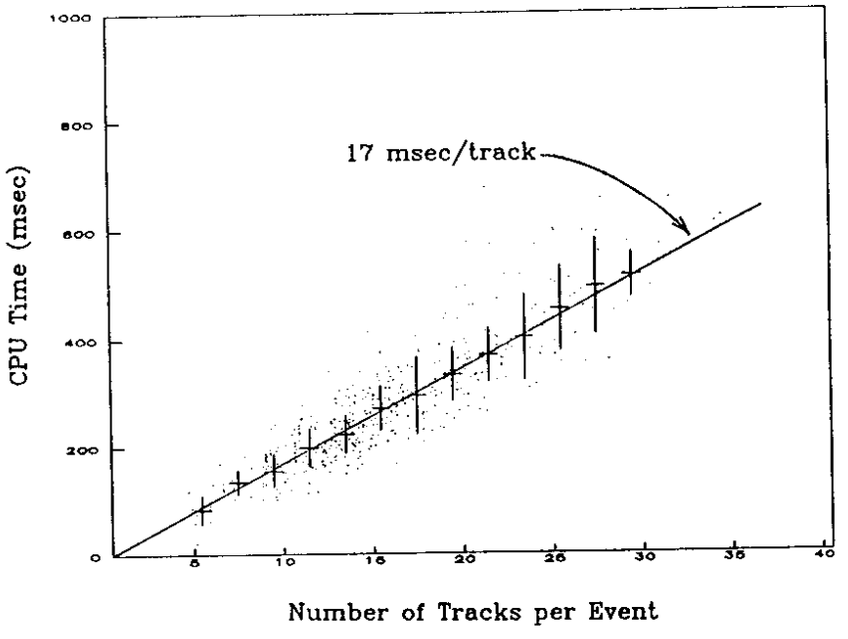

Figure B.7: CPU time per event vs. charged track multiplicity.

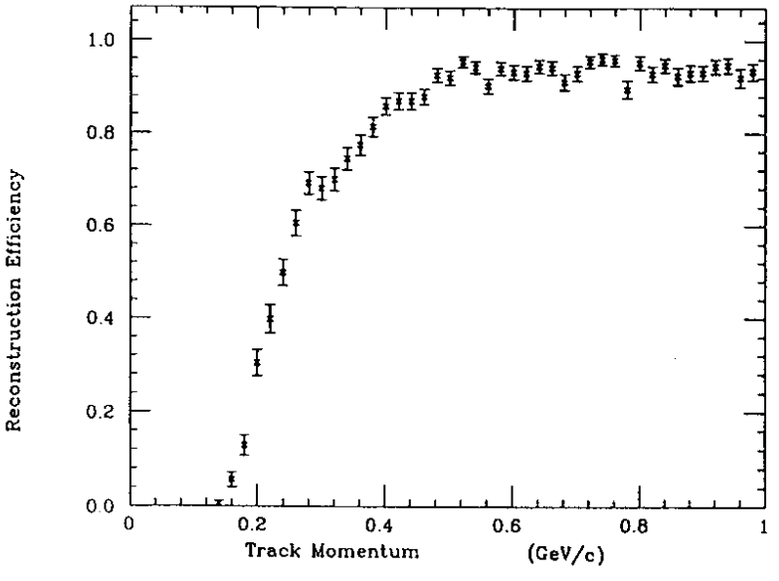

Figure B.8: Track reconstruction efficiency of ACE; Calculated for the simulated hadronic events.

search pattern for the vectors after the high momentum tracks have been found.

Thus, these problems are likely to be overcome by slight modifications of ACE that are forth-coming. But, currently, in order to cure these problems, we have adopted the use of a second-stage tracking program, DUET [89].

DUET was originally developed for the tracking in the CLEO detector at the CESR e^+e^- storage ring. By modifying and adding some routines to the code, this program was adjusted for tracking in the AMY CDC. The necessary modifications included the re-definitions of the detector geometry, the modification of the input/output data structures, and the adjustment of the sections of the code that performed the chamber corrections. Many parameters inside the code had to be tuned so that more efficient and faster reconstruction could be achieved.

In this program, the Link-and-Tree method developed by Kowalski and Cassel [88] is further extended. The Link-and-Tree method is an unbiased and exhaustive search method which proves to be faster than a conventional Road method. At the price of providing high quality tracking, DUET consumes a considerable amount of CPU time. Therefore, DUET is used only to improve the tracking of ACE. It takes the tracks found by ACE, refines them, and also tries to reconstruct missed tracks. In this way DUET refines or finds secondary tracks that were biased or missed by ACE.

Several schemes to improve DUET's slow tracking were devised. For example, only about half of the axial layers are used for the track finding, while all of them are used in the final fitting. (On the other hand, all the stereo layers are used in both stages, because the tracking of the stereo wires is relatively faster.) Some low momentum tracks, which curl around inside the CDC because of the 3 tesla field, leave many hits in the chamber. Clumps of hits created this way cause DUET to try an almost infinite number of combinations of the hits for its disparate search for tracks. This problem was solved by artificially deleting some of the hits if there are such clumps of hits. Currently, it takes about 15 seconds to process a typical hadronic event through DUET (on a FACOM M 382). As evidence for the good tracking achieved by ACE and DUET, a signal corresponding to $K^0_S \to \pi^+\pi^-$ in the hadronic event sample has been efficiently reconstructed (see Fig. B.9).

B.4 Conclusion

Here, we have described a new track finding program designed to take full advantage of the band structure of the AMY CDC. This program, ACE, has been successfully used as a charged track finder for events of all types that are being studied by the AMY collaboration. It serves the purpose of intensive tracking for very complicated events with high multiplicity with help of a second-stage tracker, DUET. Furthermore, because it is fast, it is also used at an early stage of event selection to filter large samples of data.

It is demonstrated that a tracking device that allows for the local reconstruction of track segments is very powerful for analyzing complex events with narrow

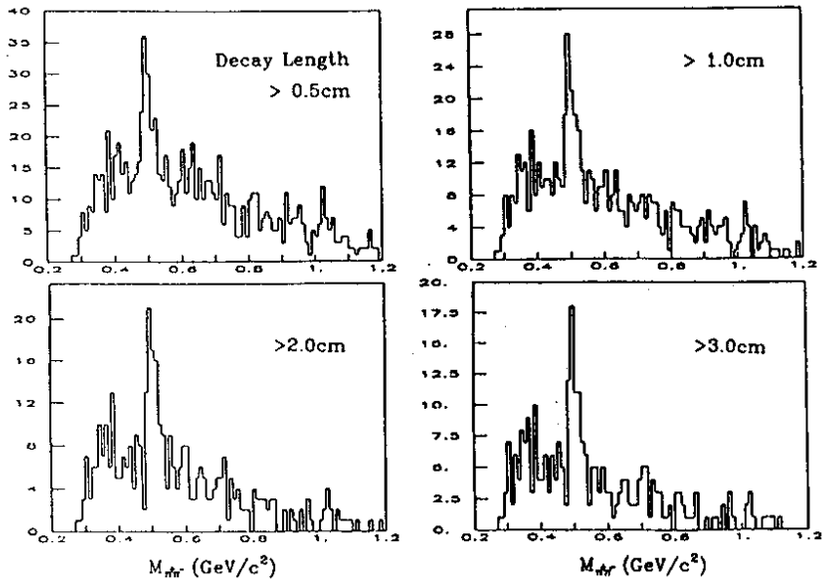

Figure B.9: Invariant mass distribution of π^+ and π^- in the hadronic events. A peak of K^0_S is clearly seen at the correct mass.

jets and high multiplicity.

Appendix C

List of the AMY Collaborators

The AMY Collaboration

A. Bacala,[b] R. Imlay,[b] P. Kirk,[b] J. Lim,[b] R.R. McNeil,[b] W. Metcalf,[b] C.P. Cheng,[c] J. Li,[c] Y.K. Li,[c] Z.P. Mao,[c] Y.T. Xu,[c] Y.C. Zhu,[c] A. Abashian,[d] K. Gotow,[d] E.H. Low,[d] M.E. Mattson,[d] F. Naito,[d] L. Piilonen,[d] K.L. Sterner,[d] R. Childers,[e] C. Darden,[e] S. Lusin,[e] C. Rosenfeld,[e] S. Wilson,[e] M. Frautschi,[f] H. Kagan,[f] R. Kass,[f] C.G. Trahern,[f] Winston Ko,[g] R.L. Lander,[g] K. Maeshima,[g] R.L. Malchow,[g] J.R. Smith,[g] K. Sparks,[g] M.C.S. Williams,[g] K. Abe,[h] Y. Fujii,[h] Y. Higashi,[h] S.K. Kim,[h] Y. Kurihara,[h] A. Maki,[h] T. Nozaki,[h] T. Omori,[h] H. Sagawa,[h] Y. Sakai,[h] Y. Sugimoto,[h] Y. Takaiwa,[h] S. Terada,[h] K. Tsuchiya,[h] F. Kajino,[j] D. Perticone,[k] R. Poling,[k] T. Thomas,[k] J. Green,[l] I.H. Park,[l] S. Sakamoto,[l] F. Sannes,[l] S. Schnetzer,[l] R. Stone,[l] S. Trentalange,[l] J. Vinson,[l] Y. Ishi,[m] K. Miyano,[m] H. Miyata,[m] Y. Yamashita,[n] D. Blanis,[o] A. Bodek,[o] H. Budd,[o] R. Coombes,[o] S. Eno,[o] C.A. Fry,[o] H. Harada,[o] Y.H. Ho,[o] Y.K. Kim,[o] T. Kumita,[o] T. Mori,[o] S.L. Olsen,[o,i] P. Perez,[o] A. Sill,[o] N.M. Shaw,[o] E.H. Thorndike,[o] K. Ueno,[o] H.W. Zheng,[o] K. Eguchi,[p] H. Itoh,[p] H. Ichinose,[q] S. Kobayashi,[q] A. Murakami,[q] K. Toyoshima,[q] J.S. Kang,[r] H.J. Kim,[r] M.H. Lee,[r] S.S. Myung,[r] G.N. Kim,[s] E.J. Kim,[s] D. Son,[s] H. Kosuka,[t] S. Matsumoto,[t] T. Sasaki,[t] T. Takeda,[t] R. Tanaka,[t] R. Chiba,[u] S. Igarashi,[u] H. Yokota,[u] T. Ishizuka,[v] and K. Ohta[v]

[b] *Louisiana State University, Baton Rouge, LA 70803*
[c] *Institute for High Energy Physics, Beijing*
[d] *Virginia Polytechnic Institute and State University, Blacksburg VA 24061*
[e] *University of South Carolina, Columbia, SC 29208*
[f] *Ohio State University, Columbus Ohio 43210*
[g] *University of California, Davis, Davis, CA 95616*
[h] *KEK, National Laboratory for High Energy Physics, Ibaraki 305*
[i] *Tsukuba University, Ibaraki 305*
[j] *Konan University ,Kobe 658*
[k] *University of Minnesota, Minneapolis MN 55455*
[l] *Rutgers University, Piscataway NJ 08854*
[m] *Niigata University, Niigata 950-21*
[n] *Nihon Dental College, Niigata 951*
[o] *University of Rochester, Rochester NY 14627*
[q] *Saga University, Saga 840*
[r] *Korea University, Seoul 132*
[s] *Kyungpook National University, Taegu 635*
[t] *Chuo University, Tokyo 112*
[u] *Tokyo Institute of Technology, Tokyo 152*
[v] *Saitama University, Urawa 338*

Bibliography

[1] TRISTAN Project Group, *"TRISTAN Electron-Positron Colliding Beam Project"*, *KEK Report* 86-14 (1987).

[2] S.L. Wu, *Phys. Report* **107**, 59 (1984).

[3] AMY Collaboration, *Proposal*, TRISTAN-EXP-003 (1984).

[4] S.L. Glashow, *Nucl. Phys.* **22**, 579 (1961);
S. Weinberg, *Phys. Rev. Lett.* **19**, 1264 (1967).

[5] D. Gross and F. Wilczek, *Phys. Rev. Lett.* **30**, 1343 (1973);
H.D. Politzer, *Phys. Rev. Lett.* **30**, 1346 (1973);
S. Weinberg, *Phys. Rev. Lett.* **31**, 494 (1973);
H. Fritzsch, M. Gell-Mann, and H. Leutwyler, *Phys. Lett.* **47B**, 365 (1973).

[6] W. Celmaster and R.J. Gonsalves, *Phys. Rev. Lett.* **44**, 560 (1979);
V.G. Chetyrkin, A.L.Kataev, and F.V.Tkachev, *Phys. Lett.* **85B**, 277 (1979);
M. Dine and J. Sapirstein, *Phys. Rev. Lett.* **43**, 668 (1979).

[7] T. Appenlquist and H.D. Politzer, *Phys. Rev.* **D12**, 1404 (1976);
A. DeRujula and H. Georgi, *Phys. Rev.* **D13**, 1296 (1976);
J. Jersak, E. Laermann, and P.M. Zerwas, *Phys. Lett.* **98B**, 363 (1981);
Phys. Rev. **D25**, 1218 (1982);
S. Gusken, J.H. Kuhn, and P.M. Zerwas, *Phys. Lett.* **155B**, 185 (1985).

[8] S.G. Gorishny, A.L. Kataev, and S.A. Larin, *Phys. Lett.* **212B**, 238 (1988).

[9] R. Bundy, *Phys. Lett.* **45B**, 340 (1973).

[10] D.W. Duke and R.G. Roberts, *Phys. Report* **120**, 275 (1985).

[11] G. Arnison et al. (UA1 Collaboration), *Phys. Lett.* **166B**, 484 (1986).

[12] R. Ansari et al. (UA2 Collaboration), *Phys. Lett.* **186B**, 440 (1987).

[13] W. Hollik, *Preprint*, DESY 86-049 (1986);
W. Marciano and A. Sirlin, *Phys. Rev.* **D29**, 945 (1984).

[14] K. Aoki, Z. Hioki, R. Kawabe, and T. Muta, *Progr. Theor. Phys. Supplement* **73**, 1 (1982);
D.A. Ross and J.C. Taylor, *Nucl. Phys.* **B51**, 25 (1973).

[15] U. Amaldi et al., *Phys. Rev.* **D36**, 1385 (1987).

[16] G. Costa et al., *Nucl. Phys.* **B297**, 244 (1987).

[17] Z. Hioki, *Prog. Theor. Phys.* **71**, 663 (1984).

[18] R.M. Godbole, S. Pakvasa, and D.P. Roy, *Phys. Rev. Lett.* **50**, 1539 (1983);
V. Barger, A.D. Martin, and R.J.N. Phillips, *Phys. Lett.* **125B**, 339 (1983).

[19] D. Albert et al., *Nucl. Phys.* **B166**, 460 (1980).

[20] W. deBoer, *Preprint*, MPI-PAE/Exp.El. 167 (1986);
H.J. Behrend et al. (CELLO Collaboration), *Phys. Lett.* **183B**, 400 (1987).

[21] W. Bartel et al. (JADE Collaboration), *Phys. Lett.* **129B**, 145 (1983);
B. Adeva et al. (Mark-J Collaboration), *Phys. Rev. Lett.* **50**, 799 (1983);
R. Brandelik et al. (TASSO Collaboration), *Phys. Lett.* **113B**, 499 (1982).

[22] E. Fernandez et al. (MAC Collaboration), *Phys. Rev.* **D31**, 1537 (1983).

[23] D. Bender et al. (HRS Collaboration), *Phys. Rev.* **D31**, 1 (1983);
L. Criegee and G. Knies (PLUTO Collaboration), *Phys. Rep.* **83**, 153 (1982).

[24] R. Giles et al. (CLEO Collaboration), *Phys. Rev.* **D29**, 1285 (1984);
E. Rice (CUSB Collaboration), *Ph.D. thesis*, Columbia Univ. (1982);
S. Weseler (DASP2 Collaboration), *Diploma thesis*, Univ. of Heidelberg (1981);
H. Albrecht et al. (DASP2 Collaboration), *DESY report* 82-037 (1982), unpublished;
B. Niczyporuk et al. (LENA Collaboration), *Z. Phys.* **C15**, 299 (1982);
Ch. Gerke (PLUTO Collaboration), *Dissertation*, Univ. of Hamburg (1979).

[25] Z. Jakubowski et al. (Crystal Ball Collaboration), *Preprint*, DESY 88-032, SLAC-PUB-4567 (1988).

[26] F. Wilczek, *Phys. Rev. Lett.* **39**, 1304 (1977).

[27] B.H. Wiik, *DESY Report* 80-124 (1980); *Proc. XXth Intern. Conf. on High Energy Physics*, Univ. of Wisconsin, Madison, Wisconsin.

[28] W. Bartel et al. (JADE Collaboration), *Phys. Lett.* **160B**, 337 (1985);
H.J. Behrend et al. (CELLO Collaboration), *Phys. Lett.* **144B**, 297 (1984);
B. Adeva et al. (MARK-J Collaboration), *Phys. Rev. Lett.* **53**, 134 (1984);
Phys. Lett. **152B**, 439 (1985).

[29] M. Althoff et al. (TASSO Collaboration), *Phys. Lett.* **138B**, 441 (1984).

[30] C. Albajar et al. (UA1 Collaboration), *Z. Phys.* **C37**, 505 (1988).

[31] C. Albajar et al. (UA1 Collaboration), *Phys. Lett.* **198B**, 271 (1987);
A. Datta and R.M. Gudlole, *Phys. Rev.* **D37**, 225 (1988);
F. Halzen et al., *Phys. Rev.* **D37**, 229 (1988);
A. Datta et al., *Phys. Rev.* **D37**, 1876 (1988);
A.D. Martin et al., *Phys. Lett.* **189B**, 220 (1987).

[32] H. Albrecht et al. (ARGUS Collaboration), *Phys. Lett.* **192B**, 245 (1987);
C. Albajar et al. (UA1 Collaboration), *Phys. Lett.* **186B**, 427 (1987);

H.R. Band et al. (MAC Collaboration), *Phys. Lett.* **200B**, 221 (1988).

[33] G. Altarelli and P.J.Franzini, *Z. Phys.* **C37**, 271 (1988); *Preprint*, CERN-TH 4745/87 (1987);
J. Ellis et al., *Phys. Lett.* **B192**, 201 (1987);
I.I. Bigi and A.I. Sanda, *Phys. Lett.* **B192**, 307 (1987);
V. Barger et al., *Phys. Lett.* **B194**, 312 (1987);
D. Du and Z. Zhao, *Phys. Rev. Lett.* **59**, 1072 (1987);
J. Maalampi and M. Roos, *Phys. Lett.* **B195**, 489 (1987);
H. Harari and Y. Nir, *Phys. Lett.* **B195**, 586 (1987);
L.-L. Chau and W.-Y. Keung, *Preprint*, UCD-87-02 (1987);
A. Datta, E.A. Paschos, and U. Türke, *Phys. Lett.* **B196**, 376 (1987).

[34] F. Halzen et al., *Phys. Lett.* **182B**, 388 (1986);
J.R. Cudell et al., *Preprint*, MAD/PH/376 (1987); *Phys. Lett.* **B197**, 227 (1987).

[35] F. Halzen, *Proc. VIIth Intern. Conf. on Phys. in Collision* (1987).

[36] S.L. Glashow and E.E. Jenkins, *Phys. Lett.* **B196**, 233 (1987); *Preprint*, HUTP-87/A047 (1987);
G. Altarelli and P.J.Franzini, *Preprint*, CERN-TH 4745/87 (1987).

[37] M. Tanimoto, *Z. Phys.* **C36**, 193 (1987);
J.D. Bjorken and I. Dunietz, *Phys. Rev.* **D36**, 2109 (1987);
A. Datta, E.A. Paschos, and U. Türke, *Phys. Lett.* **B196**, 376 (1987).

[38] V. Barger et al., *Phys. Rev.* **D24**, 1328 (1981);
H. Georgi and S. Glashow, *Nucl. Phys.* **B167**, 173 (1980);
G.L. Kane and M.E. Peskin, *Nucl. Phys.* **B195**, 29 (1982).

[39] W. Bartel et al. (JADE Collaboration), *Phys. Lett.* **132B**, 241 (1983);
B. Adeva et al. (Mark J Collaboration), *Phys. Rev. Lett.* **50**, 799 (1983);
A. Chen et al. (CLEO Collaboration), *Phys. Rev. Lett.* **52**, 1084 (1984);
P. Avery et al. (CLEO Collaboration), *Phys. Rev. Lett.* **53**, 1309 (1984).

[40] V. Barger, et al., *Preprint*, MAD/PH/150 (1984);
V. Barger, R.J.N. Phillips, and A. Soni, *Preprint*, MAD/PH/295 (1986).

[41] W.S. Hou and R.G. Stuart, *Preprint*, MPI-PAE/PTh 53/88 (1988).

[42] B. Adeva et al. (Mark J Collaboration), *Phys. Rev.* **D34**, 681 (1986).

[43] W. Bartel et al. (JADE Collaboration), *Z. Phys.* **C36**, 15 (1987);
B. Noraska, *Phys. Rep.* **148**, 204 (1987).

[44] F. Cornet, K. Hagiwara, et al., *Phys. Lett.* **B174**, 224 (1986);
V. Barger, R.J.N. Philips, and A. Soni, *Phys. Rev. Lett.* **57**, 1518 (1986).

[45] H.J. Behrend et al. (CELLO Collaboration), *Phys. Lett.* **B193**, 157 (1987).

[46] E. Farhi, *Phys. Rev. Lett.* **39**, 1587 (1977).

[47] A. DeRujula et al., *Nucl. Phys.* **B138**, 387 (1978).

[48] F. Kajino, A. Abashian, and K. Gotow, *Nucl. Instrum. Methods* **A245**, 507 (1986).

[49] S.S. Myung, *Doctoral thesis*, Korea University (1988).

[50] Y. Doi et al., *Preprint*, KEK 88-22 (1988), submitted to *Nucl. Instrum. Methods*.

[51] M. Gyr and C. Iselin, *"POISSON"*, CERN (1976).

[52] H. Asakura et al., *Reports of the Faculty of Science and Engineering, Saga Univ.* Vol.16, No.2 (1988).

[53] G. Altarelli and G. Parisi, *Nucl. Phys.* **B126**, 298 (1977).

[54] G.C. Fox et al., *Nucl. Phys.* **B168**, 285 (1980)

[55] K. Kato and T. Munehisa, *Phys. Rev.* **D36**, 61 (1987).

[56] W. Bartel et al. (JADE Collaboration), *Phys. Lett.* **101B**, 129 (1981); **134B**, 275 (1984); *Z. Phys.* **C21**, 37 (1983);
H. Aihara et al. (TPC/2γ Collaboration), *Z. Phys.* **C28**, 31 (1985);
M. Althoff et al. (TASSO Collaboration), *Z. Phys.* **C29**, 29 (1985).

[57] F.F. Field and R.P. Feynmann, *Nucl. Phys.* **B136**, 1 (1978);
P. Hoyer et al., *Nucl. Phys.* **B161**, 349 (1979);
A. Ali et al., *Phys. Lett.* **93B**, 155 (1980).

[58] B. Andersson et al., *Phys. Rep.* **97**, 33 (1983).

[59] R.D. Field et al., *Nucl. Phys.* **B213**, 65 (1983);
B.R. Webber et al., *Nucl. Phys.* **B238**, 492 (1984).

[60] T. Sjostrand et al., *Com. Phys. Comm.* **27**, 243 (1982); *Com. Phys. Comm.* **28**, 229 (1983); *Com. Phys. Comm.* **39**, 347 (1986); *Com. Phys. Comm.* **43**, 367 (1987).

[61] K. Kato and T. Munehisa, *KEK Report* 84-18 (1984).

[62] F.A. Berends, R. Kleiss, and S. Jadach, *Nucl. Phys.* **B202**, 63 (1982); *Com. Phys. Comm.* **29**, 185 (1983);
F.A. Berends and R. Kleiss, *Nucl. Phys.* **B178**, 141 (1981).

[63] J. Fujimoto and Y. Shimizu, *Mod. Phys. Lett.* **A3**, 581 (1988);
J. Fujimoto, K. Kato, and Y. Shimizu, *Preprint*, KEK 87-69 (1987), submitted to *Prog. Theo. Phys.*
This is not the first calculation of full electroweak corrections to quark-pair production; see the following references:
G. Passarino and M. Veltman, *Nucl. Phys.* **B160**, (1979) 151;
M. Bohm and W. Hollik, *Nucl. Phys.* **B204** (1982) 45; *Nucl. Phys.* **B249** (1985) 61;
M. Igarashi et al., *Nucl. Phys.* **B263** (1986) 347.

[64] Ch. Berger and W. Wagner, *Phys. Rep.* **146**, 1 (1987).

[65] J.J. Sakurai and D. Schildknecht, *Phys. Lett.* **41B**, 489 (1972);
I.F. Ginzburg and V.G. Serbo, *Phys. Lett.* **109B**, 231 (1982).

[66] Ch. Berger et al. (PLUTO Collaboration), *Z. Phys.* **C26**, 353 (1984).

[67] H. Terazawa et al., *Rev. Mod. Phys.* **45**, 615 (1973).

[68] S. Kawabata, *Com. Phys. Comm.* **41**, 127 (1986).

[69] Ch. Berger et al. (PLUTO Collaboration), *Z. Phys.* **C26**, 191 (1984).

[70] N. Arteaga-Romero et al., *Z. Phys.* **C32**, 105 (1986).

[71] J. Smith, *Preprint*, UCD-88-25 (1988).

[72] W.R. Nelson et al., *"The EGS4 code system"*, SLAC-Report-265 (1985).

[73] A. Grant, *Nucl. Instrum. Methods* **131**, 167 (1975).

[74] K. Tobimatsu and Y. Shimizu, *Progr. Theor. Phys.* **74**, 567 (1985); **75**, 905 (1986);
S. Kuroda et al., *Comp. Phys. Comm.* **48**, 355 (1988).

[75] S.K. Kim, *Doctoral thesis*, Korea University (1988).

[76] N. Cabibbo and R. Gatto, *Phys. Rev.* **124**, 1577 (1961).

[77] F. Jegerlehner, *Z. Phys.* **C32**, 195 (1986).

[78] J. Cole, G. Penso, and C. Verzegnassi, *Preprint*, Trieste 10/85/EP (1985).

[79] Y. Shimizu, (in Japanese) *KEK Report* 84-23 (1985).

[80] F.A. Berends and G.J. Komen, *Phys. Lett.* **63B**, 432 (1976).

[81] Y.S. Tsai, *Preprint*, SLAC-PUB-3129 (1983), unpublished.

[82] F.A. Berends, G.J.H. Burgers, and W.L. van Neerven, *Phys. Lett.* **185B** 395 (1987).

[83] R. Marshal, *Preprint*, RAL-88-049 (1988), submitted to *Z. Phys.*

[84] W.J. Marciano, *Phys. Rev.* **D29**, 580 (1984).

[85] O.V. Tarasov et al., *Phys. Lett.* **93B**, 429 (1980).

[86] S. Behrends, *Ph.D. thesis*, Univ. of Rochester, Appendix 1 (1987).

[87] A. Wagner, *Phys. Scripta* **23**, 446 (1981);
R.L. Gluckstern et al., *Nucl. Instrum. Methods* **24**, 381 (1963).

[88] D.G. Cassel and H. Kowalski, *Nucl. Instrum. Methods* **185**, 235 (1981).

[89] D.G. Cassel and M. Ogg, *"DUET - a Track-Finding Program for Cylindrical Geometries"*, CLEO Internal Report (1983).